The Pennsylvania State University

The Graduate School

College of Earth and Mineral Sciences

STRUCTURE AND PERFORMANCE RELATIONSHIP IN HIGH PERFORMANCE LITHIUM ION BATTERY CATHODES

A Dissertation in

Energy and Mineral Engineering

by

Pengyu Zhu

Submitted in Partial Fulfillment
of the Requirements
for the Degree of

Doctor of Philosophy

August 2013

The dissertation of Pengyu Zhu was reviewed and approved* by the following:

Yongsheng Chen
Assistant Professor of Energy and Mineral Engineering
Dissertation Co-Advisor
Co-Chair of Committee

Donghai Wang
Assistant Professor of Mechanical and Nuclear Engineering
Dissertation Co-Advisor
Co-Chair of Committee

Caroline Burgess Clifford
Senior Research Associate, EMS Energy Institute

Sharon Falcone Miller
Associate Professor of Energy and Mineral Engineering
Senior Research Associate, EMS Energy Institute

Sulin Zhang
Associate Professor of Engineering Science and Mechanics and Bioengineering

Luis F. Ayala H.
Associate Professor of Petroleum and Natural Gas Engineering
Chair of Graduate Program

*Signatures are on file in the Graduate School

ABSTRACT

The goal of this dissertation is to study the structure and performance relationship in cathodes material used in lithium-ion battery applications. In addition, functional materials used for other energy applications, such as oxygen reduction reaction in fuel cell and selective oxidation of ethane, are also discussed in the appendix.

Energy storage systems are the essential part for electric vehicles (EVs) and the urge for the development of affordable and reliable battery systems for EVs promotes the research on lithium ion battery. In this dissertation, two types of cathode materials, namely $Li_xMo_6S_8$ Chevrel phase (CP) and nitrogen doped mesoporous carbon, were investigated, in the aim of developing high performance energy storage material, as well as establishing the correlation between the structures and high electrochemical performances.

Different from the traditional synthetic route, which requires high energy input and long calcination time, the $Li_xMo_6S_8$ Chevrel phase (CP) was synthesized via an one step molten salt method. Extraordinary electrochemical performance was observed and the Li^+ transportation properties during discharge/charge process were also investigated. Electrochemical impedance spectroscopy (EIS) technique was used to characterize the transportation kinetics of Li ion insertion/extraction processes in the CP phase. X-ray diffraction (XRD) with energy dispersive X-ray (EDX) spectroscopy and scanning electron microscopy (SEM) were used to correlate the morphology change to the Li ion insertion process.

Nitrogen doped mesoporous carbon was developed as high performance cathode material

for lithium-sulfur battery. Fundamental understanding of the mechanism of nitrogen promotion effect in mesoporous carbon was revealed by utilizing X-ray absorption near edge structure (XANES) spectroscopy to probe the chemical environment. With the existence of nitrogen dopant, the oxygen functional groups on the carbon surface were activated and tended to bond with sulfur species to form O-S bonds. This enhanced chemical adsorption process promoted the performance of Li-S battery in terms of cycling stability.

TABLE OF CONTENTS

LIST OF FIGURES

LIST OF TABLES

ACKNOWLEDGEMENT

I would like to first thank my advisor Dr. Yongsheng Chen, who shows incredible passion, and energetic working attitude to support my research. He provided me opportunities to conduct experiments at synchrotron facilities located at Argonne National Laboratory and Brookhaven national Laboratory and trained me on the state of the art characterization technique, X-ray absorption fine structure spectroscopy (XAFS), which is a very important part of my PhD work.

I would also deeply express my gratitude to my co-advisor Dr. Donghai Wang for his patient guidance that helped me entering the new research field with ease. I really appreciate the necessary resources he kindly provided for me to complete this PhD work.

I sincerely thank my committee members Dr. Caroline Clifford, Dr. Sharon Miller and Dr. Sulin Zhang for their advices, suggestions, time and efforts they devoted to my dissertation.

Moreover, I would like to acknowledge all the past and current members in Dr. Donghai Wang's group. I've learned a lot from different people with different backgrounds and had a wonderful time working together with them. I particularly thank Dr. Dongping Lv for the trainings on all the experimental setups and his timely discussion on my research progress. I would like to thank Dr. Jiangxuan Song and Terrence Xu for the development and characterization of mesoporous carbon cathode materials and the collaborative work on the X-ray absorption experiments. I want to thank Mikhail Gordin for performing scanning electron microscopy measurement on Chevrel phase electrode materials. I am thankful for Hai Zhong, who kindly shared his expertise in electrochemistry research methodology with me.

I would also thank beamline scientists Trudy Bolin, Dr. Tianpin Wu at Argonne National Lab for and Dr. Cherno Jaye, and Dr. Daniel Fischer at Brookhaven National Lab for their help on X-ray absorption fine structure spectroscopy experiments.

Chapter 1

Introduction to Lithium Ion Battery – Challenges and Opportunities

Lithium is the lightest metallic element and has great electrochemical potential. The non-rechargeable lithium battery was released commercially in the 1970s and efforts have been devoted to developing a better rechargeable lithium battery ever since. However, the safety issue of metallic lithium during charge/discharge caused a big problem. The growing dendrite of lithium penetrates through the separator and reaches to the cathode area, causing a electrical short inside the battery. In addition, the unwanted heat generated during the process quickly melts down the metallic lithium and causes safety and stability problems.

Later, efforts have been devoted to using lithium ion source to replace lithium metal in the anode in order to prevent the dendrite growth. Since the commercialization in early 1990s by SONY, lithium-ion batteries (LIBs) have been widely used as portable energy sources due to their high operation voltage, high energy and power densities, and stable cycling performance. Particularly, LIBs are used to replace other secondary batteries, including nickel-metal hydride batteries, lead-acid batteries, and alkaline batteries, to power electronic devices, medical devices, portable power tools, and more recently, hybrid and pure electric vehicles. Compared to traditional NiCd battery, LIB shows a high nominal cell voltage of 3.60V as compared to 1.20V for nickel system battery.

LIB is believed to be the promising candidate for electric vehicles (EVs) due to its higher energy density compared to other battery systems. Particular interests of LIB researches have been focused on developing a low-cost, safe, rechargeable battery of high voltage, high capacity

and good rate capability.

A typical LIB consists of a cathode (positive electrode), an anode (negative electrode), and a porous separator immersed in ion conducting liquid electrolyte. The first commercial lithium ion battery developed by SONY used lithium cobalt oxide (layer-type compound) as cathode and graphite as anode. The electrolyte was a solution of Li salt, typically $LiPF_6$ dissolved in a mixture of ethylene carbonate (EC) and diethyl carbonate (DEC) and/or dimethyl carbonate (DMC). During discharge, the Li ions flow from the anode to the cathode through the electrolyte and separator, while in charge process the direction of ions flow reversed. Figure 1-1 illustrates the process [1].

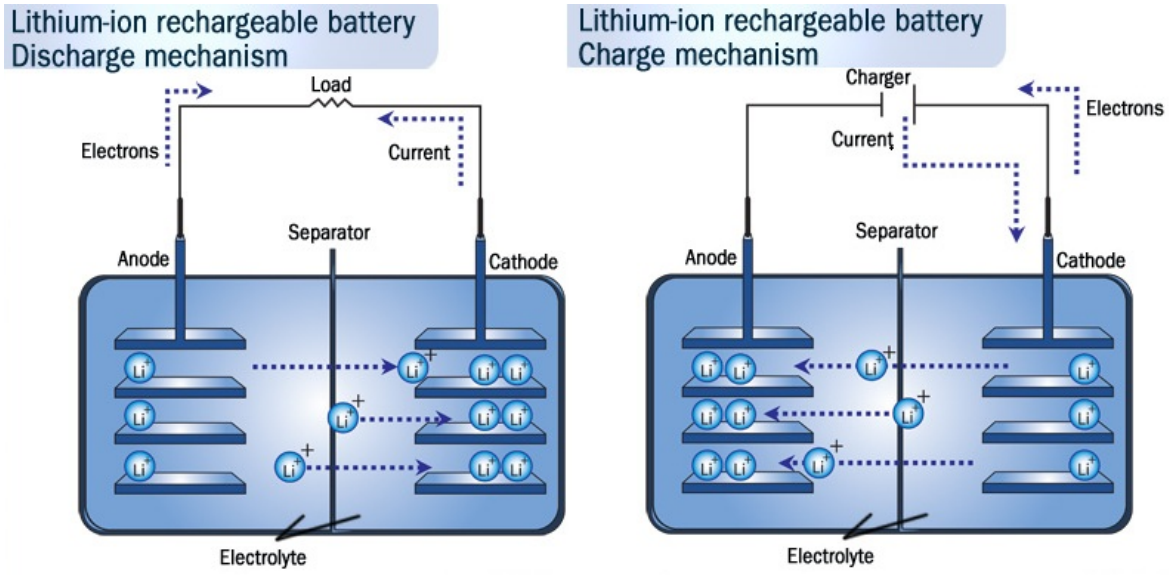

Figure 1-1. Li ion flow in lithium-ion battery during discharge/charge process. Reprint from Ref. [1].

In this chapter, a fundamental basis of lithium ion battery system will be explained along with the technical challenges, and the future development of electrolyte, cathode and anode will be discussed separately.

1.1 Requirements and constraints for LIB system

Prior to the electrode and electrolyte development, certain requirements and constraints should be met in the LIB system. Figure 1-2 shows an schematic open-circuit energy diagram of an aqueous electrolyte [2].

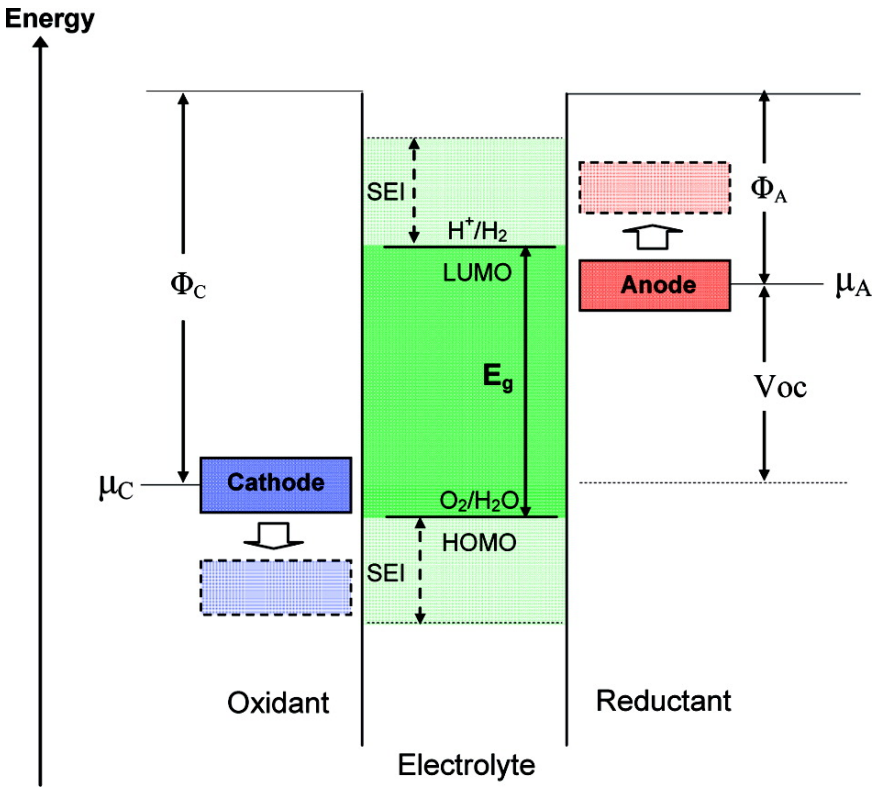

Figure 1-2. Schematic open-circuit energy diagram of an aqueous electrolyte. Reprint from Ref. [2].

In the battery system, the anode and the cathode serve as the reductant and the oxidant, respectively. The lowest unoccupied molecular orbital (LUMO) and the highest occupied molecular orbital (HOMO) determines the safe electro-window for the electrolyte in terms of thermodynamic stability. The energy difference between the HOMO and LUMO is called the HOMO–LUMO gap, here denoted as E_g in Figure 1-2. The anode and cathode have

electrochemical potentials μA and μC (their Fermi energies εF), respectively. An anode with a μA above the LUMO will reduce the electrolyte while a cathode with a μC below the HOMO will oxidize the electrolyte. A solid electrolyte interface (SEI) has to be formed between the electrode and electrolyte to prevent further reaction. Therefore, thermodynamic stability requires locating the electrode electrochemical potentials μA and μC within the window of the electrolyte. Thus, open-circuit voltage Voc of a battery can be expressed in Equation 1-1, where e is charge of electron.

$$e\,V_{OC} = \mu_A - \mu_C \leq E_g \qquad (1-1)$$

For the aqueous electrolyte, the high H^+ ion conductivity required for an aqueous electrolyte system is found only in liquid water with the limited V_{OC} at 1.3 V. It is necessary to turn to the non-aqueous system with a larger E_g for the Li ion battery. Li metal is not directly used as the anode because of its electrochemical potential (μ_A) lies above the HOMO for most practical non-aqueous electrolyte. Thus, strategies have been developed for an anode with a μ_A that matches well with the HOMO of electrolyte and a stable SEI layers during charge/discharge. In the following paragraphs, the issues of developing electrolyte, anode and cathode will be addressed individually.

1.2 Electrolyte for LIB system

Besides obtaining a large electrolyte window E_g, there are additional requirements that must be met, as follows: the conductivity of the Li^+ ion must be greater than 10^{-4} S/cm so that the electrolyte will not be the rate determining step for the Li ionic transpiration; the electronic conductivity of the electrolyte should be less than 10^{-10} S/cm so that it will not cause

short-circuited; the stability of the electrolyte should be maintained under ambient temperature and battery operation conditions; the compatibility between electrodes and electrolyte must be maintained, including the fast formation of the SEI layer in the case of electrode potential lies outside the electrolyte window; safety requirements (nonflammable and nonexplosive in case of short-circuit) and low toxicity needs to be met. Table 1-1 listed several different types of nonaqueous electrolyte that are usually used in current LIB systems [2].

Table 1-1. Nonaqueous Electrolytes for Li-Ion Batteries [2]

Electrolytes	**Example of classical electrolytes**	**Ionic conductivity ($\times 10^{-3}$ S/cm) at RT**	**Electrochemical window (V) vs Li^+/Li^0**		**Remark**
			Reduction	**Oxidation**	
Liquid organic	1M $LiPF_6$ in EC:DEC (1:1)	7	1.3	4.5	Flammable
	1M $LiPF_6$ in EC:DMC (1:1)	10	1.3	>5.0	
Ionic liquids	1M LiTFSI in EMI-TFSI	2.0	1.0	5.3	Non-flammable
	1M $LiBF_4$ in EMI-BF_4	8.0	0.9	5.3	
Polymer	LiTFSI-P(EO/MEEGE)	0.1	<0.0	4.7	Flammable
	$LiClO_4$-PEO_8+10 wt % TiO_2	0.02	<0.0	5.0	
Inorganic solid	$Li_{4-x}Ge_{1-x}P_xS_4$ (x=0.75)	2.2	<0.0	>5.0	Non-flammable
	$0.05Li_4SiO_4$ + $0.57Li_2S$ + $0.38SiS_2$	1.0	<0.0	>8.0	
Inorganic liquid	$LiAlCl_4$ + SO_2	20	-	4.4	Non-flammable
Liquid organic + Polymer	$0.04LiPF_6$ + 0.2EC + 0.62DMC + 0.14PAN	4.2	-	4.4	Flammable
	$LiClO_4$ + EC + PC + PVdF	3.0	-	5.0	
Ionic liquid + Polymer	1M LiTFSI + P_{13}TFSI + PVdF-HFP	0.18	<0.0	5.8	Less flammable
Ionic liquid + Polymer + Liquid organic	56 wt % LiTFSI–Py_{24}TFSI + 30 wt % PVdF-HFP + 14 wt % EC/PC	0.81	1.5	4.2	Less flammable
Polymer + Inorganic solid	2 vol% $LiClO_4$-TEC-19 + 98 vol% 95 ($0.6Li_2S$ + $0.4Li_2S$) + $5Li_4SiO_4$	0.03	<0.0	>4.5	Non-flammable

Organic Liquid Electrolyte. The most commonly used organic liquid electrolyte is carbonate based electrolyte which has an oxidation potential (HOMO) at 4.7V and a reduction potential at 1.0V [3, 4]. Propylene carbonate (PC), ethylene carbonate (EC), diethyl carbonate (DEC), dimethyl carbonate (DMC) and ethylmethyl carbonate (EMC) are usually used as additives in the carbonate electrolyte. Specifically, ethylene carbonate (EC) is used to assist the formation of the SEI layer when the lithium metal is used as an anode material. The drawback of the carbonate electrolyte is its high flammability with a flash point below 30 ℃. For safety issues, efforts have been devoted to replacing the carbonate electrolyte.

Room Temperature Ionic Liquids (RTILs). In the past decade, the RTILs have received lots of attention as an alternative electrolyte for LIBs owing to their non-flammability, non-volatility, high Li solubility, good thermal stability and low toxicity. Especially, the RTILs show a high anodic limit at about 5~5.5V vs. Li/Li^+. However, such material usually comes with a high viscosity that reduces the Li^+ ionic conductivity. Imidazolium-based RTILs, having high Li^+ ionic conductivity, e.g., ethyl-methyl-imidazolium bis-(trifluoromethanesulfonyl)-imide (EMI-TFSI), 1-methyl-3-methylimidazolium tetrafluoroborate ($EMIBF_4$) and 1-butyl-3-methylimidazolium tetrafluoroborate ($BMIBF_4$), were investigated as an electrolyte [5, 6]. Addition of the ethylene carbonate is required for the formation of the SEI layer to overcome the poor stability at a voltage below 1V. So far, no RTILs electrolyte has been successfully utilized for large power battery.

Inorganic Liquid Electrolyte. Stassen et al. reported using a non-flammable inorganic liquid electrolyte consisting of $LiAlCl_4$ and SO_2 in a traditional $LiCoO_2$ cathode LIB system [7]. An

exceptional Li^+ ionic conductivity of 2×10^{-2} S/cm was observed at room temperature, however, the small electrolyte window compromises its advantage.

Solid Polymer Electrolyte. Polymers, especially polyethylene oxide (PEO) type polymers with lithium salt $LiPF_6$ or $LiAsF_6$, were used as low-cost, nontoxic electrolyte [8, 9]. However, the biggest drawback is the PEO based electrolyte cannot provide a high Li^+ ionic conductivity ($<10^{-5}$ S/cm) at room temperature. Although the metal oxides, such as Al_2O_3, TiO_2 and ZrO_2, were added to the PEO electrolyte to enhance the conductivity, these materials are still lack of competence [10, 11].

Inorganic Solid Electrolytes. Inorganic solid electrolytes have recently drawn much attention due to their potential applications in the rechargeable lithium batteries. Different types of materials with high Li^+ ionic conductivities ($>10^{-4}$ S/cm) have been extensively studied and the emphasis has been placed on the correlation between the composition, structure and the electrical transport property [12-16]. Such materials usually possess high ionic conductivity and large electrochemical window. Recently, Kamaya et al. have reported a sulfur based $Li_{10}GeP_2S_{12}$ electrolyte with extraordinary ionic conductivity (10^{-2} S/cm) [17]. The quick development of novel solid state electrolyte materials will provide promising solutions for the safety issues in LIB system.

1.3 Electrodes for LIB system

In the LIB system, the electrolyte serves as the ionic pathway for Li^+ transportation while the electrodes, both the anode and the cathode, serve as lithium storage matrixs for reversible lithium insertion and extraction. As shown in Figure 1-1, upon discharging, the lithium stored in

the anode is oxidized and released to the electrolyte and the lithium ion is reduced and intercalates into the cathode; upon charging, the lithium in cathode is oxidized back to the lithium ion and moves toward to the anode and intercalates into the anode after reduction.

The choice of electrode materials is crucial since the performance of the cell is mainly determined by its properties. There are several criteria for good electrode materials, including a high gravimetric energy density, high volumetric energy density, high rate capability (power density), and high cycle life. For electrode to yield higher energy density, efforts have been devoted to searching for electrode materials that can operate at high voltage (≧ 4.0V vs Li) for cathode and low voltage (≦ 0.5V vs Li) for anode.

1.3.1 Anode materials

Extensive research has been devoted to understanding and improving the existing anode materials for LIBs applications. Ideally, the anode material should contain elements with low atomic or formula weights that can accommodate large amount of Li^+ per molecule, have a potential as close to Li metal so that the total cell work voltage is high, be chemically stable in electrolyte, and possess good electronic and Li^+ ionic conductivity. Graphite can intercalate Li ions up to the composition LiC_6 with a theoretical anode capacity at 372 $mAhg^{-1}$. Efforts were made to further increase the Li content in the carbon beyond the LiC_6 form limit, to increase the capacity of graphite but so far have not been successful. Thus, research has been conducted intensively to develop next generation anode to replace graphite. The research for the development of anode materials is mainly guided by two mechanisms, namely intercalation/deintercalation and alloying.

The intercalation/deintercalation process usually involves metal oxides or other compounds with 2D layer structures or 3D network structures that can reversibly intercalate Li ions into the lattice without destroying the crystal structure [18]. Titanium oxides are the representative of such materials and many studies (listed in Table 1-2) were conducted on evaluating TiO_2 with different morphology as anode materials. Researchers tried to control the particle sizes and surface areas of TiO_2 to create the best morphology to achieve higher reversible capacity and longer cycling capability.

The prerequisite conditions should be met for developing such materials. First, the host material should possess vacancy sites in their one dimensional channel, 2D layers and 3D channels that enable Li intercalation/deintercalation. Second, the host material should contain transition metals or rare earth metals that have multiple valance states. It is because the intercalation of one Li ion will lead to reduction of valance state of the host material by one unit. For example, α-Fe_2O_3 will form $Li_xFe_2O_3$ ($x \leq 0.5$) after the Li intercalation while α-Al_2O_3 will not undergo the Li intercalation [18].

Alloying mechanism is generally a reaction between elements or metals with the Li to form alloy or intermetallic compounds for lithium storage during charging and releases Li ions during discharging. Examples for such materials are Si [19-22], Sb [23, 24] and metals such as Sn [25, 26], Zn[23], In[23], Bi[23] and Cd[23]. These materials are able to store large amount of Li ions per unit, e.g., $Si + 4.4\ Li \leftrightarrow Li_{4.4}Si$. The Li alloying-dealloying usually occur at low potentials ($\leq$ 1.0 V vs Li).

Table 1-2 Physical properties and electrochemical Li cycling data of TiO_2 [18].

Morphology	Particle/crystallite size (nm)	Surface area (M^2g^{-1})	Current rate (1C= 335 mAg^{-1})	Reversible capacity (mA h g^{-1})	Voltage, range= 1~3 V vs. Li (cycling range, capacity retention after n cycles)
TiO_2 nanoparticles	6	223	0.05C	165	91% (n=1-50)
Commercial sample	89	10	0.05C	100	80% (n=1-20)
Mesporous TiO_2 sub-microspheres	14 (XRD)	116.49	0.1C	180	93% (n=5-80)
Mesporous TiO_2	9 (XRD)	92	4C	157	84% (n=1-50)
TiO_2-Cu				191	82% (n=1-50)
TiO_2-Sn				196	80% (n=1-50)
Nanoporous as prepared	5.1 (XRD)	524.5	0.2C	94	95% (n=100)
Spherical	9-11	80	0.2C	270	91% (n=2-30)
Nanoparticle	9	110	1C	160	83% (n=50)
TiO_2 prepared by molten salt method at 280℃	13 (XRD)	200	0.1C	227	76% (n=2-60)

1.3.2 Cathode materials.

For a material to be considered as a good candidate for cathode material for rechargeable LIB, it usually meets following the requirements: (1) it has to be readily reducible/oxidizable, (i.e., transitional metal); (2) the material can reversibly react with Li during intercalation-deintercalation processes without collapsing of the host structure; (3) the material should yield high energy density, namely, it gives out high voltage (preferably above 4V) and high capacity; (4) the material possesses high ionic and electronic conductivity; and (5) the material should be chemically stable, with low cost and environmentally friendly [27].

Nearly all the research conducted on cathode materials focuses on two types of materials. One type is layered compounds that consists of close-packed anion lattice (O or S) surrounding a redox-active transition metal (Ti, Mn and Co) in between [27]. The vacancies between layers are the pathways for the Li ion transportation. Examples for these types of materials (illustrated in Figure 1-3) are $LiTiS_2$, $LiCoO_2$ and novel $LiNi_yMn_yCo_{1-2y}O_2$ that provides higher working voltage.

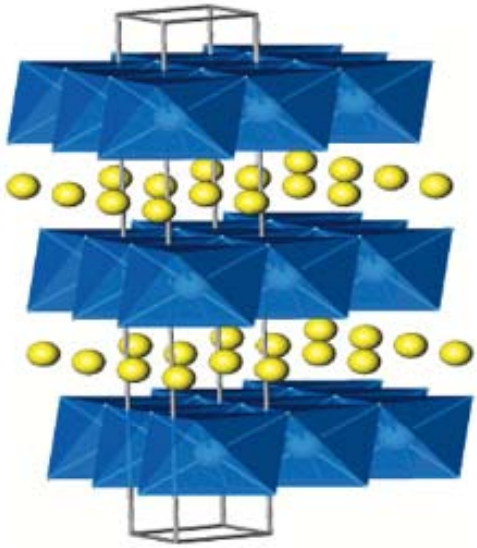

Figure 1-3. Layered structure of $LiCoO_2$ with lithium ions between the transition-metal oxide sheets. Reprint from Ref. [27].

The other type has more open structures and tunnel compounds such as vanadium oxides, manganese dioxide, transition metal phosphate $LiFePO_4$ and Chevrel phase material [27]. The lithium ions are inserted in the vacancies between the units and these vacancies serve as Li transportation pathways.

1.3.3 Beyond the conventional LIBs

Lithium-air Battery. As a possible solution for electric vehicle propulsion problem, lithium-air battery became a research hotspot since 2009. Currently, the insufficient capacity of battery severely limits the range of practical electric vehicles. Theoretically, the lithium-air battery potentially has a much higher gravimetric capacity compared to all other batteries.

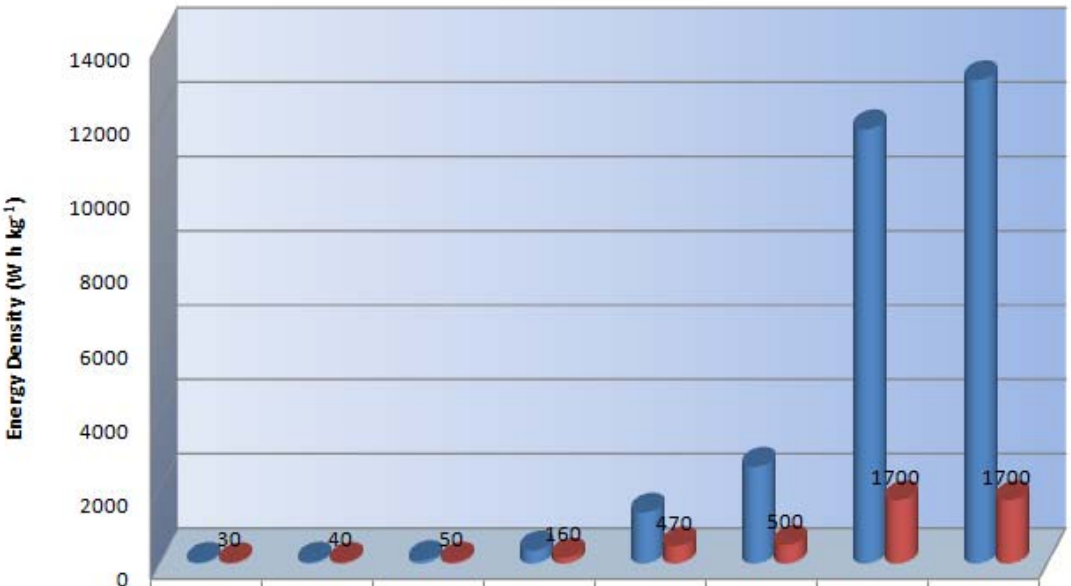

	Lead-Acid	Ni-Cd	Ni-Metal Hydride	Li-Ion	Zinc-Air	Li-S	Li-Air	Gasoline
Theoretical	40	50	90	350	1370	2600	11680	13000
Practical	30	40	50	160	470	500	1700	1700

Figure 1-4. The gravimetric energy densities ($Whkg^{-1}$) for various types of rechargeable batteries compared to gasoline. Reprint from Ref. [28].

Figure 1-4 shows the comparison of various battery systems vs. gasoline in terms of gravimetric energy density ($Whkg^{-1}$). The theoretical energy density of gasoline is 13,000 $Whkg^{-1}$ and tank-to-wheel efficiency of US fleet is 12.6% [28]. Thus, an approximation of 1,700 $Whkg^{-1}$ was made for practical gravimetric energy density of gasoline. Li-air battery shows a theoretical energy density of 11,680 $Whkg^{-1}$ that is compared to the gasoline. It is possible to

achieve a cell with energy density of 1,700 $Whkg^{-1}$ if long term research and development are devoted to overcoming several fundamental challenges.

The biggest challenge is that the electrochemical reaction between Li and air are not truly reversible. There are multiple reactions taking places on the cathode. Depending on different electrotypes, the reactions on the cathode are different. In nonaqueous Li/air batteries, the reactions on cathode are shown as follow:

$$2\,Li + \frac{1}{2}O_2 \leftrightarrow Li_2O \qquad (1-3) \qquad \text{and} \qquad 2\,Li + O_2 \leftrightarrow Li_2O_2 \qquad (1-4)$$

In aqueous media, the reactions on the cathode depend on the pH value. In acidic and alkaline aqueous solutions, the reactions on cathode undergo these paths, respectively:

$$2\,Li + \frac{1}{2}O_2 + H_2O \leftrightarrow 2LiOH \qquad (1-5) \qquad 2\,Li + \frac{1}{2}O_2 + 2H^+ + H_2O \qquad (1-6)$$

It has been reported that, in the nonaqueous system, the cycle of the reaction involves with interactions with the carbonate based electrolyte. Li_2O_2 doesn't serve as the discharge product and evolution of CO_2 instead of O_2 are observed upon the charge process [29-31]. At the cost of consumption of the electrolyte, the electrochemical reactions are not reversible and no other solvent has yet demonstrated highly reversible cycling [32]. Other challenges for Li-air battery include obtaining high capacity in the positive electrode, accommodating significant volume change during cycles, stabilizing Li metal negative electrodes, supplying contaminant-free O_2 to the system (CO_2, H_2O). There are many challenges that lie ahead of Li-air battery commercialization. However, it also comes with big opportunities.

***Lithium-Sulfur Battery*.** Current lithium-ion technologies are limited by the low theoretical gravimetric capacity (300 $mAhg^{-1}$) for long range electric vehicles applications. Besides, the high

cost of LIB system in electric vehicle (being about half the retail cost of the car) hinders the commercial viability of electric vehicle (EV).

Sulfur has been studied as cathode material since 1960s but only recent progress on the material development promotes the lithium-sulfur battery as the promising next generation battery system. Although the working voltage for a sulfur cathode is only 2.15V vs Li^+/Li, it gives a high theoretical specific capacity (1,672 $mAhg^{-1}$). Thus, the Li-S battery have a theoretical energy density of 2,600 $Whkg^{-1}$ or 2,800 WhL^{-1} based on weight or volume, respectively, which is about four times increase in terms of energy density compared to present LIBs [33, 34].

As a cathode material, sulfur behaves very differently from typical intercalation materials (i.e., $LiFePO_4$, $LiMn_2O_4$). Sulfur forms a ring structure comprised of stacked eight atoms (S_8) as in its most stable form. During discharge, the cleavage of sulfur-sulfur bond occurs to the stacked eight atom ring sulfur and the sulfur chain tends to bond with lithium ions to form highly soluble polysulfide species Li_2S_n ($3 \leq n \leq 8$) within the organic electrolyte environment. The sulfur chain is gradually shortened by S-S bond cleavage as the discharge process goes further and eventually the insoluble discharge products Li_2S_2 and Li_2S are formed (Figure 1-5).

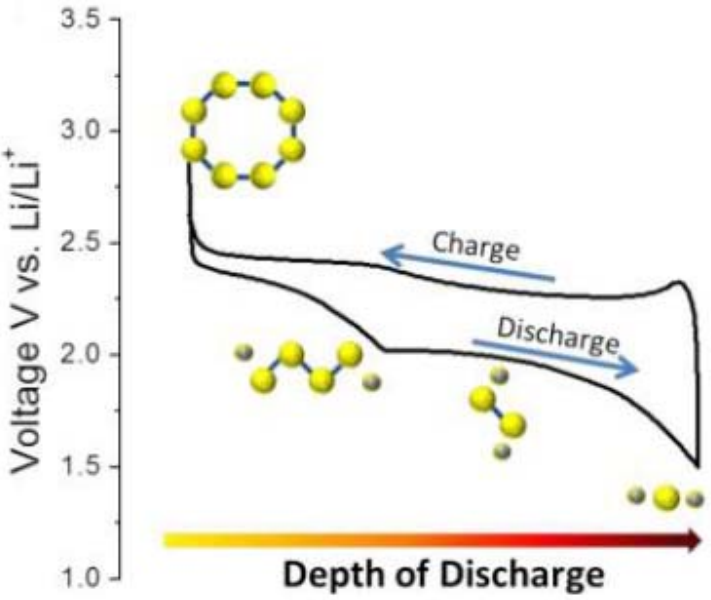

Figure 1-5. A typical voltage vs. capacity plot for Li-S battery. Reprint from Ref. [34].

The overall redox reaction can be described in the equation shown below in Reaction 1-7.

$$S_8 + 16Li \leftrightarrow 8Li_2S \qquad (1-7)$$

However, the Li-S battery is still far from commercialization. First, sulfur is a highly insulating material, both ionically and electrically (5×10^{-30} S/cm at RT), so it cannot be directly used as an electrode material. Owing to the insulating nature of sulfur, conductive sulfur facilitator is needed for the cathode, such as carbon and metal materials with high surface area and large pore volume. A polymer binder is used to glue the carbon additive and sulfur particle together in the cathode material (shown in Figure 1-6). In addition, reducing the sulfur particle size also increased the higher utilization of sulfur by reducing the electric and ionic diffusion paths.

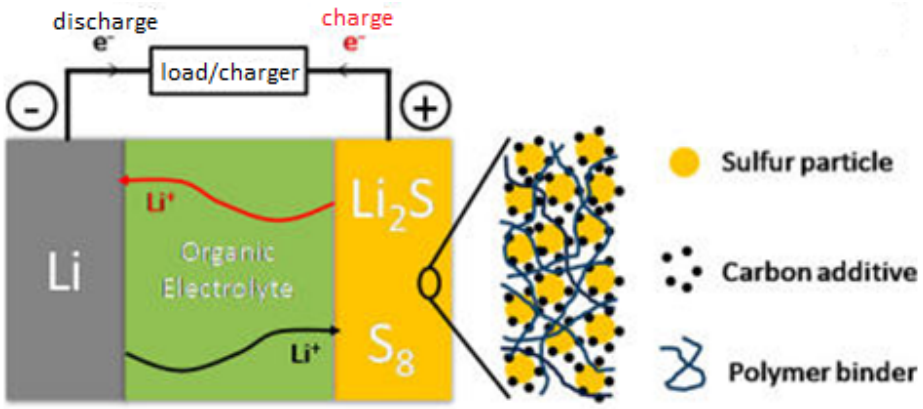

Figure 1-6. Illustration of the charge/discharge process involved in a rechargeable Li-S cell consisting of lithium metal anode, organic electrolyte, and sulfur composite cathode. Reprint from Ref. [35].

The second issue comes from the highly soluble intermediate discharge product polysulfide. In the organic electrolyte environment, the loss of sulfur contents during charge/discharge results from the dissolution of the polysulfide and leads to a low coulombic efficiency, short cycle life of the sulfur electrode and finally the rapid fading of capacity [36-38].

The shuttle effect is caused by the incomplete recharge of Li-S cell so that the polysulfides cannot completely transform back to elemental sulfur and stay in the form of high order polysulfides (such as Li_2S_8, Li_2S_6). In the subsequent discharge cycles, these polysulfides dissolve into the electrolyte and leave the cathode area and move towards the Li anode. At the anode, they directly react with Li metal to recreate the low order polysulfides. Thus, these polysulfides are shuttling between the electrodes back and forth, causing the low utilization of sulfur in the anode and a series of problems faced in Li-S battery system [37, 39].

Many efforts have been devoted to overcoming those obstacles including introduction of additives into organic electrolytes, e.g., $LiNO_3$, developing solid state electrolytes, protective

layers, and novel sulfur-carbon cathodes[38, 40-44]. Specifically, development of carbon-sulfur cathode materials gained extensive attention. Carbon became the most widely used conductive additive in the cathode owing to its high conductivity and the porous structural feasibility for facilitating the redox reaction.

In this work, my focus is on the development of better cathode materials for lithium-sulfur system and to correlate the enhanced performance with the fundamental understanding of the mechanism. Nitrogen doped mesoporous carbon is developed as a cathode material and better sulfur retention is achieved within the cathode, leading to a higher columbic efficiency. Detailed investigation of the carbon based Li-S cathode will be given in Chapter 4.

1.4 Scope of the dissertation

The dissertation mainly covers the high performance cathode development in the field of lithium ion battery. For the development of $Li_xMo_6S_8$ Chevrel phase material used as a cathode in lithium ion battery, a simple synthetic route is developed from the molten salt method. This greatly reduces the time and the harsh synthetic conditions, which originally hinders the wide application of the material for battery. The Li insertion/extraction mechanism and the morphology change associated with the process are monitored and investigated through electrochemical and structural characterization methods.

In the Li-S battery field, various carbon based materials are widely used as cathode material. A novel, mesoporous, nitrogen-doped carbon (MPNC)-sulfur nanocomposite material was developed as a cathode for Li-S batteries. Better cycling stability and coulombic efficiency are

observed. Mechanism of the nitrogen promotion effect is studied via X-ray absorption near edge structure (XANES) spectroscopy. The enhanced chemical adsorption promoted the sulfur immobilization capability of carbon and thus leads to better battery performance.

The dissertation is summarized in Chapter 5 with the correlation between activity and material structure in energy storage applications. Recommendations for expansion of research projects are made based on current results and discoveries.

In the appendix, the X-ray absorption spectroscopy is used for characterizing functional materials in other energy applications. Correlation between the structure and performance are established. The extended X-ray absorption fine structure (EXAFS) is utilized for characterizing PtVCo ternary catalysts for the oxygen reduction reaction (ORR) reaction in fuel cell application. Coordination numbers and bond distances between targeting and neighboring atoms are determined via the fitting of EXAFS spectra and they serve as indications for the degree of alloying in the ternary system. A correlation between the enhanced electrochemical activity and the nanostructure of the catalyst is established. The result is useful for optimizing the thermochemical treatment condition and sets guideline for future ternary catalysts design.

XANES is shown to be a powerful tool for probing the chemical environment of the materials. Mo based catalyst on SBA-15 support is studied for the selective oxidation of ethane to aldehydes. Potassium is used as an additive for promoting the selectivity of aldehyde. Mo L_3-edge XANES is used for determining the Mo coordinate symmetry and helps to correlate the enhanced catalytic activity to the coordination structure.

Chapter 2

Experimental Approaches

The evaluation of battery development involves many electrochemical techniques and each of them is quite unique and can provide useful information for battery performance evaluation. In this chapter, introductions will be given on the electrochemical as well as chemical methods that are used for testing and characterization of electrode materials.

2.1 Basics of energy storage evaluation

Batteries are energy storage devices. For battery application, people care about four physical properties: energy, power, mass and volume. Energy is a fundamental quantity and has a unit of Joule. Power is the rate at which energy is transferred, with a unit of Watt (1 Watt = Joule/ Second and 1 Wh = 3600 J). In energy storage systems, people also care about how effectively the energy may be stored in a system. There are two ways to evaluate this, one is based on the mass, and the other, the volume. Energy stored per unit mass is usually called specific energy and the energy stored per unit volume is referred to as energy density.

Voltage is also an important parameter in battery evaluation. It is the electric potential between the anode and the cathode and has a unit of Volt, which is equivalent to Joule/Coulomb. Through voltage, one can link the energy and capacity. Capacity measures the total amount of charge involved in the electrochemical reaction and has a unit of Coulomb (1C=1A x 1s). In the battery field, people usually use a different unit of Amp-hours (Ah) instead of Coulomb ($1\ Ah = 1\ A \times 3600\ s = 3600\ C$). Capacity is an important parameter when evaluating an electrode material. In battery literature, people usually use specific capacity (Ah/kg) or

volumetric capacity (Ah/l) to represent capacity per unit mass and capacity per unit volume, respectively.

Accordingly, one can calculate the energy of a battery as long as obtaining the working voltage and the capacity of the battery. For example, a battery has 3.6 V working voltage and 1 Ah capacity, the energy it stores equals $3.6\,V \times 1\,Ah = 3.6\,{}^{J}/_{C} \times 3600\,C = 12960\,J = 12.96\,KJ = 3.6\,Wh$

Thus, the aim of developing better battery system for energy storage always focus on increasing the work voltage of the battery and increasing the capacity of the electrode materials. The definitions of terms used in energy storage evaluation are given in Table 2-1.

Table 2-1 Definitions of terms used in energy storage system evaluation

Name	**Unit**	**Definition**
Coulomb	C	1 A x s
Capacity	C, Ah	Total amount of charge transferred between two electrodes in the electrochemical reaction
Specific capacity	Ah/kg, mAh/g	Capacity per unit mass
Volumetric capacity	Ah/L	Capacity per unit volume
Energy	J, Wh	Amount of electrical work done = U x I x t
Specific energy	Wh/kg	Energy per unit mass
Energy density	Wh/L	Energy per unit volume
Power	W	Rate at which the energy is available = U x I

Another important parameter used for battery performance evaluation is the C rate. Discharge current is often expressed as a C-rate in order to normalize against battery capacity, which is often very different between batteries. A C-rate is a measure of the rate at which a battery is discharged relative to its maximum capacity. For example, a 1C rate means that the discharge current will discharge the entire battery in 1 hour. For a battery with a capacity of 100 Ah, this equates to a discharge current of 100 A. A 5C rate for this battery would be 500 A, and a 0.5C rate would be 50 A [45]. Thus, when indicating the discharge rate in terms of C-rate, the capacity should always be specified.

2.2 Coin cell fabrication

The performance of electrode materials is usually tested in coin cell battery. For study of the cathode material, the material is usually mixed with the conductive additive (carbon), solvent (e.g., N-methyl-2-pyrrolidinone (NMP)), and binder (polyvinylidene fluoride (PVDF)) forming slurry and coated to the Al current collector. Li chip is used as the anode.

As shown in Figure 2-1, one stainless spacer is used on each side of the two electrodes to ensure good contact between the electrode and the cap. One commercial available ionic membrane is placed between the cathode and the anode to physically separate the two electrodes. Liquid electrolyte floods all the spaces between the cathode cap and the anode cap. A special press is used to seal the coin cell. The assembled coin cell is shown in Figure 2-1.

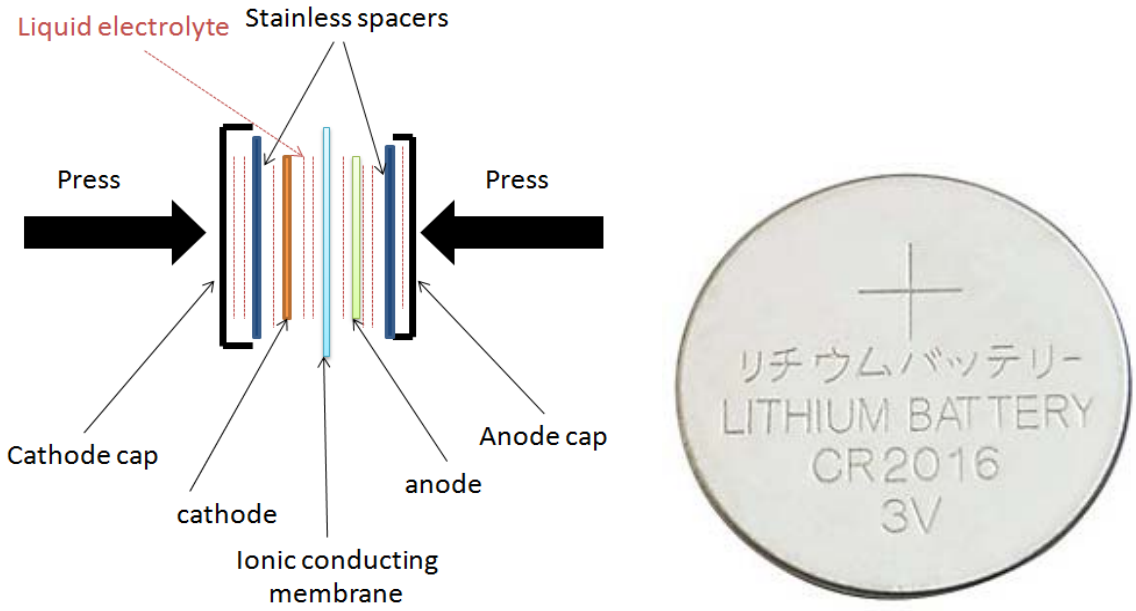

Figure 2-1. Diagrammatic sketch (shown on left) of components within a 2016 type coin cell (shown on right)

Note that the Li metal and most electrolytes used in LIBs are air sensitive. Thus, the whole assembling and pressing processes are conducted in an argon filled glove box (Figure 2-2).

Figure 2-2. Glove box for assembling 2016 type coin cell

2.3 Electrochemical characterization techniques

2.3.1 Charge/discharge cycling

The most straightforward electrochemical evaluation technique is galvanostatic charging and discharging of an electrode material. Usually, a constant current is applied, and the resulting voltage change is measured versus the lithium reference electrode. The change of electrochemical environment of material can be deduced from the change of voltage. The capacity of the electrode can be determined from the charge/discharge time. When applying various charge/discharge currents, the voltage at which the electrochemical reactions occur will change. From this voltage change, detailed information of the kinetics can be obtained. Figure 2-3 shows a LAND battery tester that is used for the charge/discharge cycling.

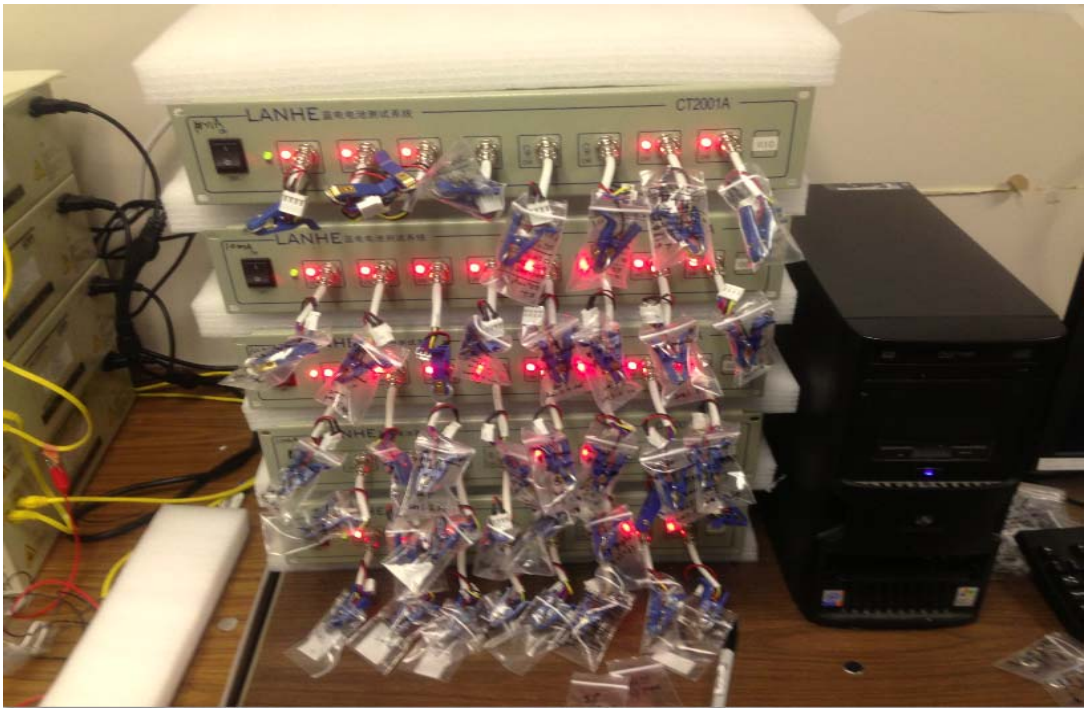

Figure 2-3. Land battery tester platform for charge/discharge cycling

2.3.2 Cyclic voltammetry test

The cyclic voltammetry (CV) test is a common electrochemical characterization technique used for investigating the reversibility of redox chemical reactions on the electrode surfaces. A voltage decrease linearly with time is applied to the working electrode. When the pre-determined value is reached, the applied voltage increase linearly up to another pre-determined value. During this process, the current response is plotted as a function of the applied potential. Figure 2-4 shows a CHI 660D electrochemical workstation for the CV test.

Figure 2-4. CHI electrochemical workstation used for cyclic voltammetry test.

The CV test utilizes a dynamic potential to monitor the change of current to probe the redox reaction taking places on the electrodes. It is convenient to locate a redox potential when a current peak appears. In addition, the CV test can be a quick tool to indentify the reversibility of redox reactions by observing the appearance of positive/negative current peaks.

2.3.3 Impedance analysis

To understand ionic conduction mechanism, the most straightforward technique is the direct measurement of electrical conductivity. The AC impedance techniques are generally simpler and more applicable to conduct conductivity studies than their DC counterparts. Figure 2-5 shows the Solartron FRA 1255B frequency response analyzer used for the AC impedance measurement.

Figure 2-5. Solarton AC impedance tester

During an AC impedance measurement a small potential perturbation is applied to the sample. The AC response to the applied perturbation, which is normally sinusoidal, can be different in phase and amplitude from the applied signal. Data from the measurement must be collected in short time, otherwise ion diffusion, rather than reaction kinetics, becomes the rate

determining process. Measurement of the phase difference and the amplitude allows analysis of the electrode process relating to contributions from diffusion, kinetics, double layer capacitance, coupled homogeneous reactions. It is widely applied in studies of ionic solids, solid electrolytes, conducting polymers, corrosion, membranes and liquid/liquid interfaces. The equivalent circuit is needed to interpret the electrochemical impedance spectrum (EIS). Simulation of the EIS provides information about resistance, capacitance, ionic transportation kinetics.

2.4. Structure characterization

During the electrochemical charge/discharge, Li ions transport in and out the electrode. The structural stability and morphology change during these processes determine the performance and the life of a battery. To determine the structural stability of the morphology, a series of electron analytical techniques were used.

2.4.1 X-ray diffraction analysis

X-rays interacts with electrons in atoms and the x-ray photons may be deflected away from its original direction. Diffracted waves from different scattering atoms will interfere with each other. The interference of waves can have constructive or destructive effects on the diffraction patterns. If atoms are arranged in order, as in crystals, the diffraction waves consist of a sharp peak with the same symmetry as the distribution of atoms. Thus, based on the Bragg's law, diffraction patterns can be used to deduce the distribution of atoms in the material.

Bragg's law is expressed in equation 2-1. $2d \sin\theta = n\lambda \qquad (2-1)$

Where d is the distance between equivalent atomic planes, θ is the angle between the

incident beam and these planes, n is an integer and λ is the wavelength. The scattered intensity can be measured as a function of scattering angle 2θ. The d spacing is calculated through the Bragg's law for determining the crystalline structure.

2.4.2 Scanning electron microscopy and energy dispersive X-ray spectroscopy

The scanning electron microscopy (SEM) is a powerful electron microscope to obtain high magnification images. It uses electron beam as a source to probe the material. The interaction between electrons and the materials can provide information about the sample's surface topography. A high resolution SEM can provide structural details down to 25 Angstroms.

SEM is commonly coupled with energy dispersive X-ray spectroscopy (EDS or EDX), to determine the spatial distribution of elements of the sample. When radiated by a electron beam, materials give off characteristic X-ray fluorescence from the elements in the beam. EDX analyze the energies of these X-ray photons by energy dispersion and subsequently identify and quantify the elements.

2.4.3 X-ray absorption fine structure spectroscopy

X-ray absorption spectroscopy (XAS) or X-ray absorption fine structure (XAFS) spectroscopy utilizes the X-ray photoelectric effect and the wave nature of the electron to determine local structures around elements of interest in materials. Unlike X-ray diffraction, XAFS doesn't require the sample material to have long range order to be detected and it has been widely used with great success in many research fields. XAFS utilizes synchrotron based X-ray sources, which can be million times brighter than conventional lab based X-ray machine, and provides atomic level coordination structure characterization and trace amount detection

sensitivity. In addition, XAFS is an element specific technique that accurately measures the absorption coefficient of selected element. XAFS can be divided into two regions: the near edge region or X-ray absorption near edge structure (XANES) and the extended region or extended x-ray absorption fine structure (EXAFS). The XANES region comprises of the absorption edge and the features before and after the edge within about 50 eV. XANES is sensitive to the oxidation states and coordination symmetry. The EXAFS covers the range beyond XANES and it may be over 1000 eV beyond the edge. EXAFS provides information about the coordination structure including coordination number, bond distance and chemical identification of neighboring atoms.

The absorption edge appears when the incident X-ray has an energy equal to or above the binding energy of a core-level electron. The core electron absorbs the photon energy and is excited to the continuum to escape the atom and a core hole is created at the core level (shown in Figure 2-6).

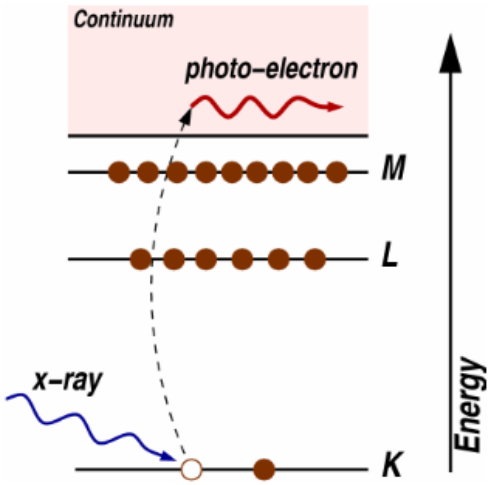

Figure 2-6. The photoelectric effect: x-ray is absorbed and a core-level electron is promoted out of the atom. Reprint from Ref. [46].

After a core hole is created by the photoelectric effect, the electron vacancy causes the atom to be in an unstable condition, leading to two competing relaxation processes to lower the overall energy of the atom as shown in Figure 2-7, namely X-ray fluorescence and Auger effect [47].

The two type of relaxation both yield secondary particles (fluorescence radiation and Auger electrons). The fluorescence photons are usually collected in the XAFS experiments as the rate absorption is proportional to the number of secondary particles. As for Auger electrons, the low count rate of Auger electrons limit its usage in XAFS spectroscopy. However, Auger electrons are usually used for elemental analysis in energy dispersive x-ray (EDX) spectroscopy.

For the XANES region, it is sensitive to geometrical structure of the absorbing atom and its electronic structure. The edge is used for determination of oxidation states of the absorbing atom. This can be simply explained considering that the atom with a higher oxidation state should have a higher charge, thus requiring more energy for the ejection of a core electron [47]. As for the pre-edge features, it is caused by the electron transitions within the molecule and may be useful for determining the coordination symmetry. For certain transition, the intensity increases following this criterion for geometry: octahedral < square-pyramidal < tetrahedral [47]. When the X-ray energy is higher than the edge energy, the outgoing photoelectron created by photoelectric effect and its scattering with the neighboring atoms are responsible for the EXAFS spectra. The outgoing photoelectron is not infinitely long lived and can only travel through several angstroms.

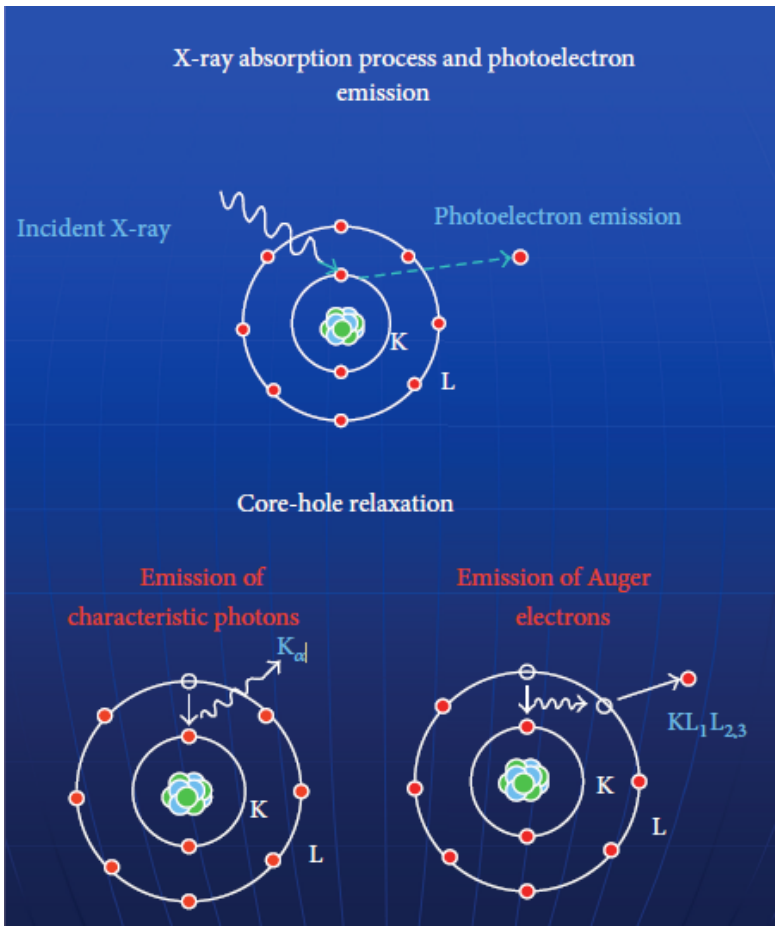

Figure 2-7. The photoelectric absorption process which creates core hole and its relaxation by fluorescent X-ray emission or Auger electron emission. Reprint from Ref. [47].

From the example shows in Figure 2-8, oscillation of the absorption coefficient, which carries the structural coordination information, can be interpreted into neighboring atom shells around the core atom after the Fourier Transformation [47]. Detailed EXAFS data processing will be discussed in Chapter 5 for the fitting of PtVCo ternary catalysts system.

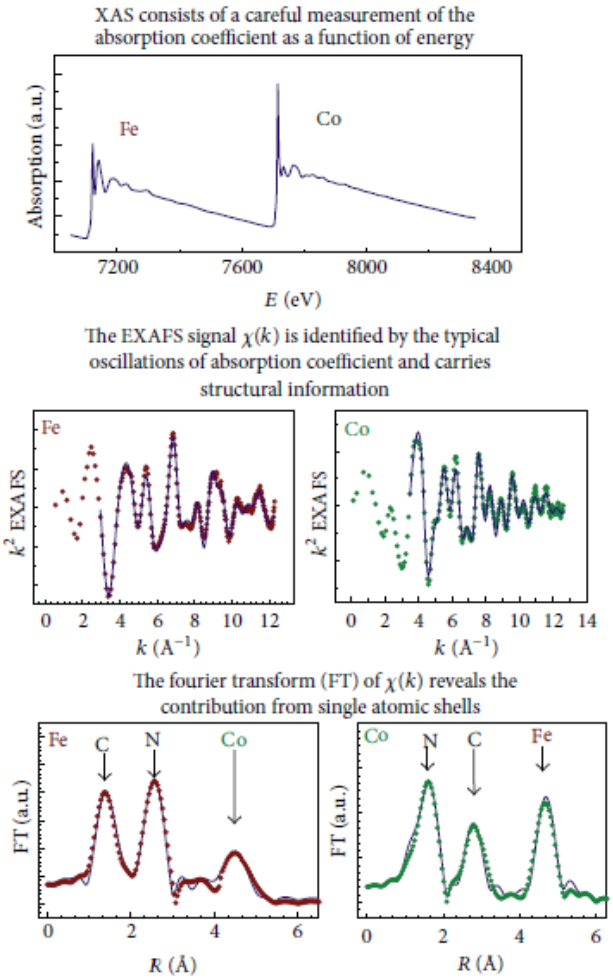

Figure 2-8. Example of the EXAFS data recording and primary data reduction of a cobalt hexacyanoferrate sample. The oscillations of absorption coefficient carry structural information, and the FT operator gives the contribution arising from single atomic shells around the photoabsorber. Reprint from Ref. [47].

Chapter 3

Investigation of $Li_xMo_6S_8$ material as cathode material in Lithium ion battery application[1]

3.1 Introduction

Chevrel phase (CP), ternary molybdenum chalcogenides with formula $M_xMo_6Y_8$ (M = 3rd row transition metals, rare-earth elements, Pb, Sn; Y = S, Se, Te) was firstly reported by R. Chevrel, M. Sergent and J. Prigent in the early 1970s. Afterwards, the CP materials were studied largely due to their outstanding superconducting abilities. The surprising finding was the discovery of sulfur based superconducting materials, since back then superconductivity had been exclusive to metals, alloys or intermediate compounds. Owing to its superior ionic conductivity, CP has been investigated as cathode material for Li-ion battery application since 1980s [48].

Nowadays, ternary Chevrel phase materials are widely used in Mg ion batteries, enabling fast ionic transport of divalent cations in the hosts. For lithium ion batteries the molybdenum cluster chalcogenides, such as binary Chevrel phase Mo_6S_8 structure, are of particular interest. They reversibly accommodate four lithium atoms per unit cell at an average potential of 2.1V vs. Li/Li^+, which yields a theoretical energy density of 280 $Whkg^{-1}$ [49].

The Mo_6-octahedra are surrounded by S_8 cubes. Lithium intercalations take place in a three dimensional network of channels within the lattice framework of Mo_6S_8. Mo_6S_8 units are separated by the inserting channels of the vacant lattice sites shown in Figure 3-1.

[1] **This chapter is a manuscript in preparation for submission as journal article** (***Zhu, P.***; Lv, D.; Wang, D.; Chen, Y., *Investigation of $Li_xMo_6S_8$ material as cathode material in Lithium ion battery application.*).

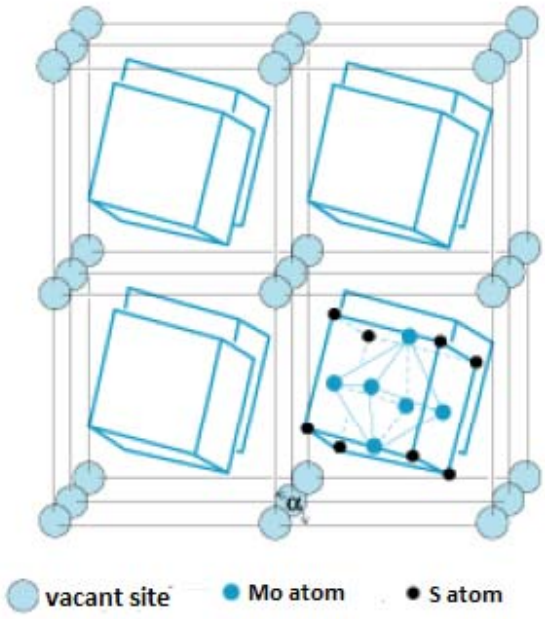

Figure 3-1. Framework structure of binary cluster Mo_6S_8. Reprint from Ref. [50].

For $0<x<1$, the $Li_xMo_6S_8$ exists as a single phase having a rhombohedral crystal structure. Drhombohedral distortion from the cubic structure increases with increasing x, with the lattice angle increasing from 91.3° at x=0 to 92.3° at x=1. For $1<x<3$, the $Li_xMo_6S_8$ exists as a two-phase mixture of $Li_1Mo_6S_8$ and $Li_3Mo_6S_8$. The $Li_3Mo_6S_8$ has a lattice constant of 6.64Å and lattice angle of 94.5° [51]. The phases of $Li_xMo_6S_8$ are metallic, thus providing a good electrical conductivity for $0<x<4$. Over the entire range of x, the relatively small change in unit cell volume and the good electrical conductivity make it a good candidate for high-rate, highly-reversible cathode [51].

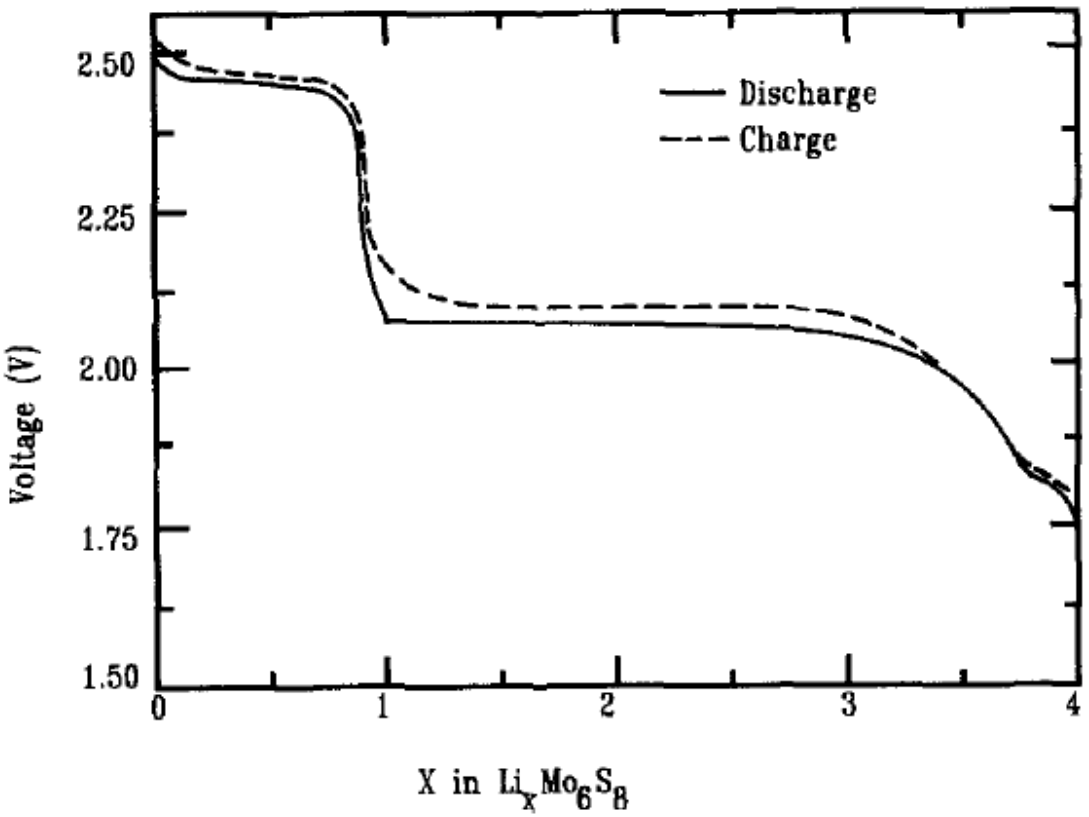

Figure 3-2 Voltage of a Li/$Li_xMo_6S_8$ cell as a function of x in $Li_xMo_6S_8$. Reprint from Ref. [51].

The long and tedious synthetic route for the Chevrel phase hinders its wide application as cathode material in the lithium ion battery. My synthetic route for $Li_xMo_6S_8$ usually starts with the synthesis of ternary Chevrel phase compounds such as $Cu_3Mo_6S_8$, followed by leaching out Cu to prepare Mo_6S_8 material [52]. The $Li_xMo_6S_8$ material is obtained after several cycles of discharge/charge process.

In present work, I utilize a molten salt method and synthesize $Li_xMo_6S_8$ material in one step under mild conditions. As a LIB cathode material, the material possesses excellent electrochemical property, especially the high rate capability and cycling stability.

3.2 Experimental section

3.2.1 Preparation of the cathode material

The Chevrel phase of $Li_xMo_6S_8$ material was synthesized via a molten salt synthesis approach. Briefly, the potassium chloride (KCl 99% Aldrich) was dried at 160 °C under vacuum for 3 hours and was used as a solvent for the following high temperature synthesis. The MoS_2 (99% Aldrich) and Li_2S (99% Aldrich) powders were used as received. The reactants were mixed in chemical stoichiometry to yield the $Li_xMo_6S_8$ formula. The solvent to reactant ratio is 2:1 by weight. The mixture was hand milled in a mortar and then transferred into a tube furnace for thermal treatment at 850°C under argon gas for 40 hours. After cooling to ambient temperature, the sample was dissolved in the DI water and washed four times through a centrifugal separation process to remove the KCl solvent, followed by drying under vacuum.

The $Li_xMo_6S_8$ cathode electrode was prepared by mixing 70 wt% CP composite powder, 20 wt% Super P (TIMCAL conductive carbon black), and 10 wt% polyvinylidene fluoride (PVDF) together in the N-methyl-2-pyrrolidinone (NMP) to form a slurry, which was then coated on an aluminum foil and dried at 80°C for 10h under vacuum.

3.2.2 Electrochemical measurements

Charge/discharge cycling. The electrochemical experiments were performed using a 2016-type coin cells that were assembled in an argon-filled dry glovebox (MBraun, Inc.). The cathode was the prepared $Li_xMo_6S_8$ material and the anode was a lithium chip. A 1M $LiPF_6$ in EC/EMC (gravimetric ratio of 3/7) was used as the electrolyte. The electrochemical performance was evaluated by galvanostatic charge/discharge cycling on a LAND battery tester at room

temperature with different charge/discharge rates in a voltage window between 1.4 and 3 V vs. Li/Li^+. The current density and specific capacity were calculated based on the mass of $Li_xMo_6S_8$ active material.

Cyclic voltammetry test. Cyclic voltammetry test were performed using a $Li_xMo_6S_8$/Li cell on a CHI 660D electrochemical workstation. Redox reaction couples occurred on the electrodes were recorded on the cyclic voltammetry spectroscopy. The CV test was started with an open circuit voltage of 2.45V. The scan rate is 0.0001 V/s with an interval of 0.001V in the electric window of 1.4V to 3V.

Impedance spectroscopy. Ex-situ EIS measurements were performed using Solartron FRA 1255B frequency response analyzer within the frequency range of 10^6 Hz to 5mHz at potentiostatic signal amplitudes of 5mV. The Nyquist plots of impedance spectra were processed via ZView software.

3.2.3. Structural characterization

X-ray diffraction analysis. The obtained $Li_xMo_6S_8$ cathode material was characterized on a Rigaku Dmax-2000 X-ray powder diffractometer (XRD) with Cu Kα radiation (λ = 1.5418 Å). The operation voltage and current were kept at 40 kV and 30 mA, respectively. The XRD diffraction patterns were analyzed via Materials Data JADE XRD pattern processing software.

Scanning electron microscopy (SEM). The cells were paused at different charge/discharge stages and were disassembled in the glove box. The $Li_xMo_6S_8$ cathodes were taken out from the cells and washed with anhydrous DME for ex-situ SEM measurement. The cathode electrodes were sealed into polyethylene pouches to prevent air exposure. The FEI Nova NanoSEM 630

scanning electron microscope coupled with energy-dispersive X-ray spectroscopy (EDX) was used to probe the changes in the surface morphology of cathode electrodes during charge/discharge cycles. In EDX analysis, at least three measurements were conducted for each sample to obtain accurate composition information and minimize the errors.

X-ray absorption near edge structure spectroscopy (XANES). The Mo L_3-edge XANES spectra were recorded at beamline of the Materials Research Collaborative Access Team (MRCAT) of Advanced Photon Source (APS) at Argonne National Laboratory. Cryogenic double-crystal Si (111) monochromator was used and the harmonics were rejected using a Rh-coated mirror. All spectra were collected in fluorescence mode with a Si DRIFT 4-element detector (Vortex) providing energy resolution of approximately 0.3 eV at 2.5 keV. Helium purging in the incident light path and the sample chamber was utilized to minimize signal loss through air absorption.

3.3 Results and Discussion

3.3.1 Morphology of the prepared $Li_xMo_6S_8$ Chevrel phase material

The X-ray diffraction was measured on three $Li_xMo_6S_8$ samples. Because lithium is a very light element with light electron clouds surrounding the core, it cannot be properly detected by the XRD technique. An alternative technique used to characterize the structure of lithium containing samples is the neutron diffraction spectroscopy. Thus, XRD is difficult to determine the Li contents in the sample.

The $Li_xMo_6S_8$ material as prepared was tested via XRD and the diffraction pattern was

shown in Figure 3-3. A significant existence of Mo_3S_4 structure was observed, which possesses a very strong characteristic peak at 13.8 2-theta degree. All the other small peaks match well with the Mo_3S_4 characteristic peaks, indicating a fairly pure Chevrel phase $Li_xMo_6S_8$. The XRD pattern indicates that the one step molten-salt synthesis successfully obtained the Chevrel phase.

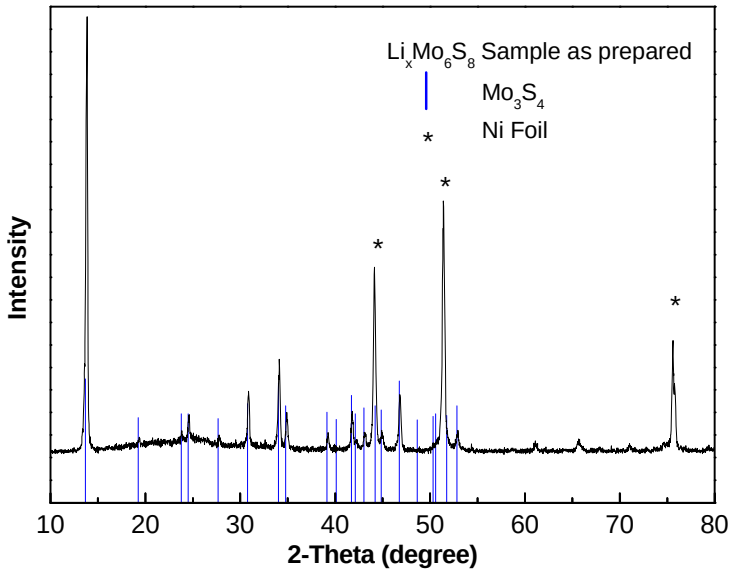

Figure 3-3. XRD pattern of $Li_xMo_6S_8$ material as prepared

The powder sample of Chevrel host $Li_xMo_6S_8$ was also measured with SEM and EDX mapping analysis. The SEM images are shown in Figure 3-4(a) and (b) with different magnifications. Cubic structures can be clearly observed from Figure 3-4(b). Figure 3-4(a) and (b) show that the particle size of CP is not uniformly distributed, ranging from several microns to several hundred nanometers.

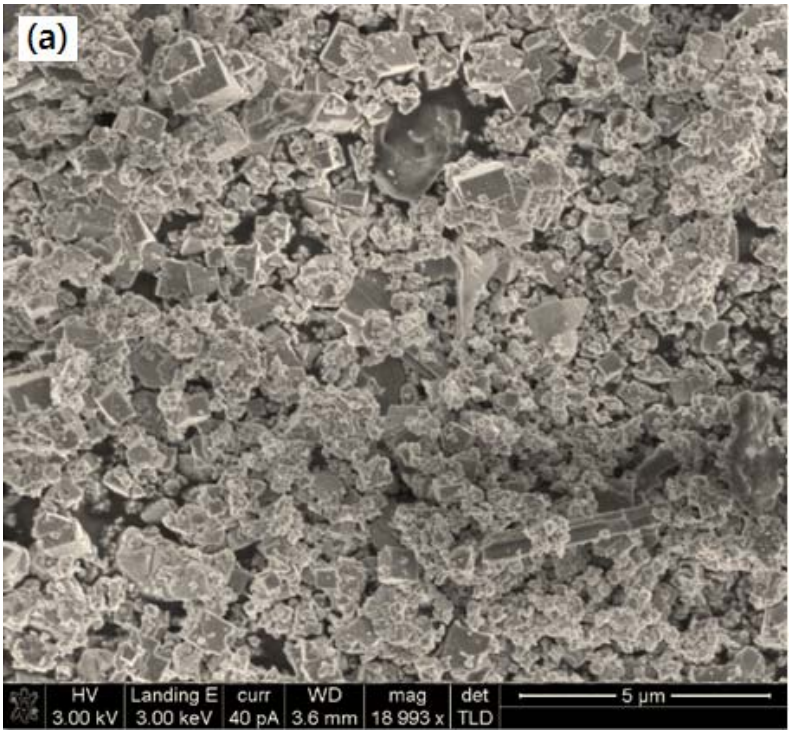
(a)
HV
3.00 kV
Landing E
3.00 keV
curr
40 pA
WD
3.6 mm
mag
18 993 x
det
TLD
5 µm

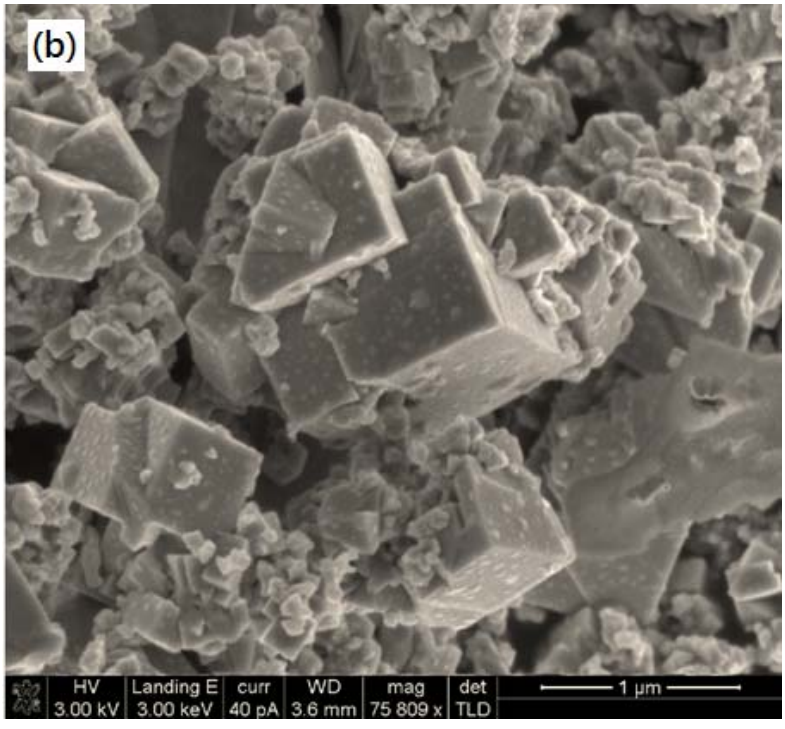
(b)
HV
3.00 kV
Landing E
3.00 keV
curr
40 pA
WD
3.6 mm
mag
75 809 x
det
TLD
1 µm

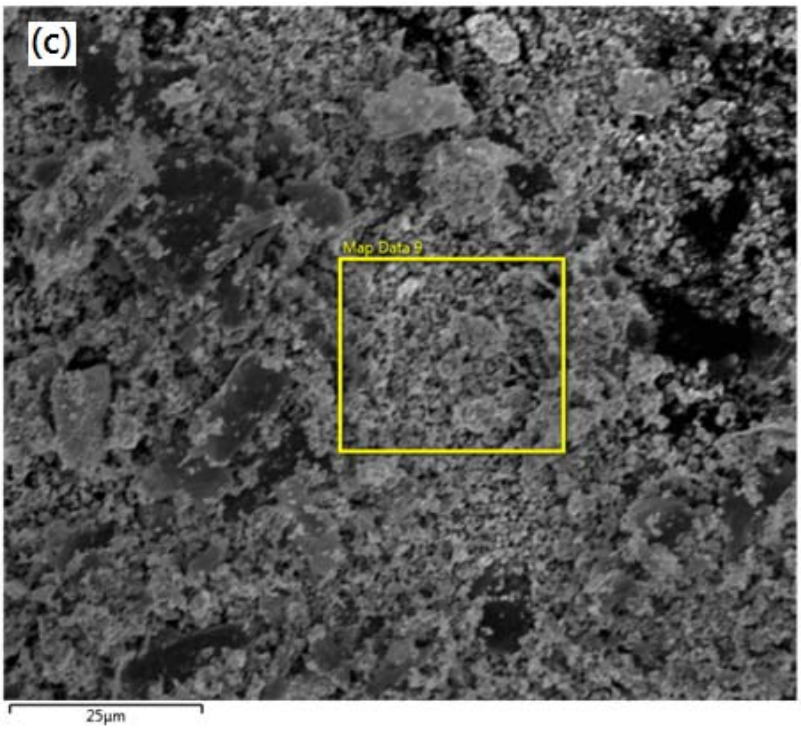
(c)
Map Data 9
25µm

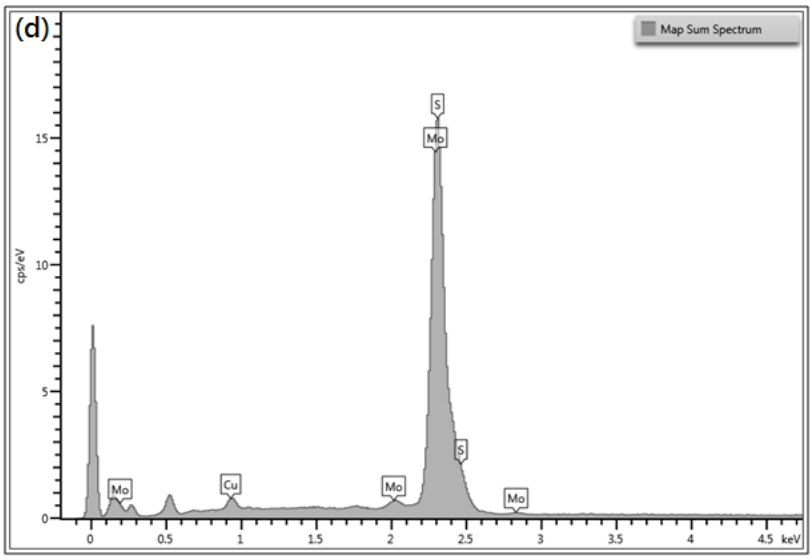
(d)
Map Sum Spectrum
cps/eV
S
Mo
Mo
Cu
Mo
S
Mo
keV

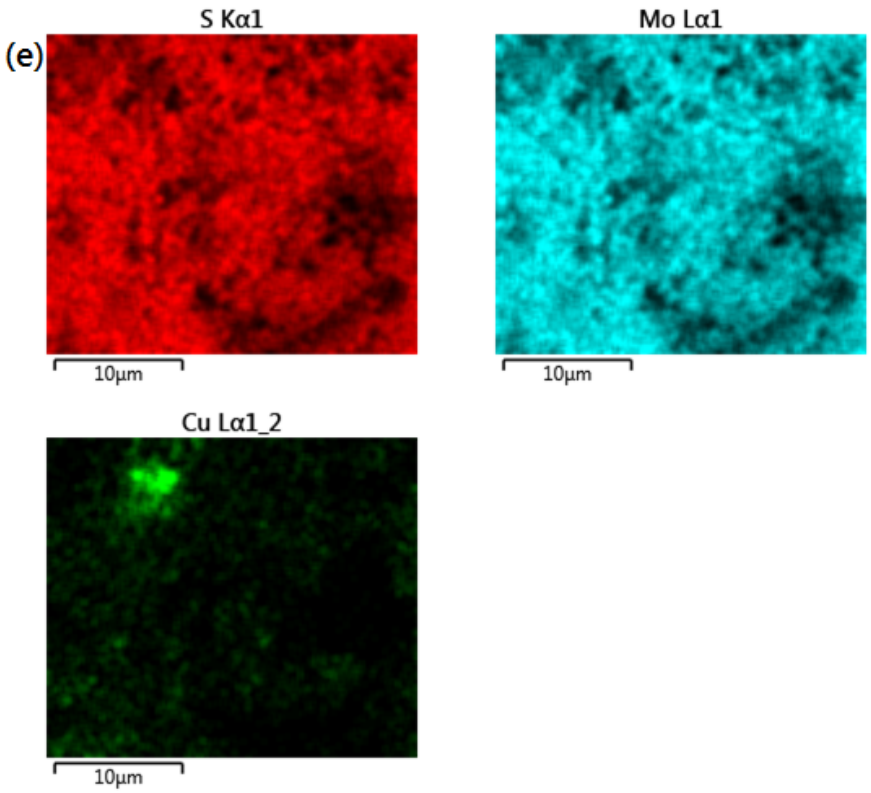

Figure 3-4. SEM images of powder sample of $Li_xMo_6S_8$ (a) with magnification of x18993 and (b) with magnification of x75809; (c) a zone of 25x25 microns for EDX elemental mapping; (d) EDX spectroscopy with illustrated elemental intensity; and (e) the elemental mapping images of S, Mo and Cu

The EDX analysis was performed on powder sample and the result is shown in Table 3-1. There is trace amount of Cu detected by EDX in the prepared sample. As shown in Figure 3-4 (e), the Cu sample is accumulated at one spot on the map instead of widely dispersed through all the samples. In addition, no species of Cu speciation are identified in the XRD patterns. This could be due to contamination during EDX sample measurement, rather than the sample preparation processes. Elements Mo and S are widely dispersed in all the area, indicating the existence of CP phase through all the area.

Table 3-1 EDX mapping result of $Li_xMo_6S_8$ powder sample

Element	Line Type	Wt%	Molar composition (per 100 gram)	Standard Label	Factory Standard
S	K series	28.80	0.9	FeS2	Yes
Mo	L series	68.69	0.72	Mo	Yes
Cu	L series	2.51	0.03	Cu	Yes
Total:		100.00	$Mo_{0.72}S_{0.9}Cu_{0.03}$		

The molar ratio of Mo/S is 0.8, slightly higher than stoichiometric ratio of 0.75, which can be attributed to the sulfur loss during the molten salt synthesis process. Although slight extra amount of Li_2S precursor was used to compensate the sulfur loss, it was difficult for accurate control.

3.3.2 Electrochemical performance and characterization

The typical voltage profile of a $Li/Li_xMo_6S_8$ coin cell employing a 1.0M $LiPF_6$ in the EC/EMC electrolyte during the discharge and charge at different rates was displayed in Figure 3-5 (a). The discharge curve shows three potential plateaus at 2.4V, 2.1V and 1.8V, respectively. The complete electrochemical reaction can be expressed in Reaction 3-1.

$$xLi + Mo_6S_8 = Li_xMo_6S_8 \quad 0 < x < 4 \qquad (3-1)$$

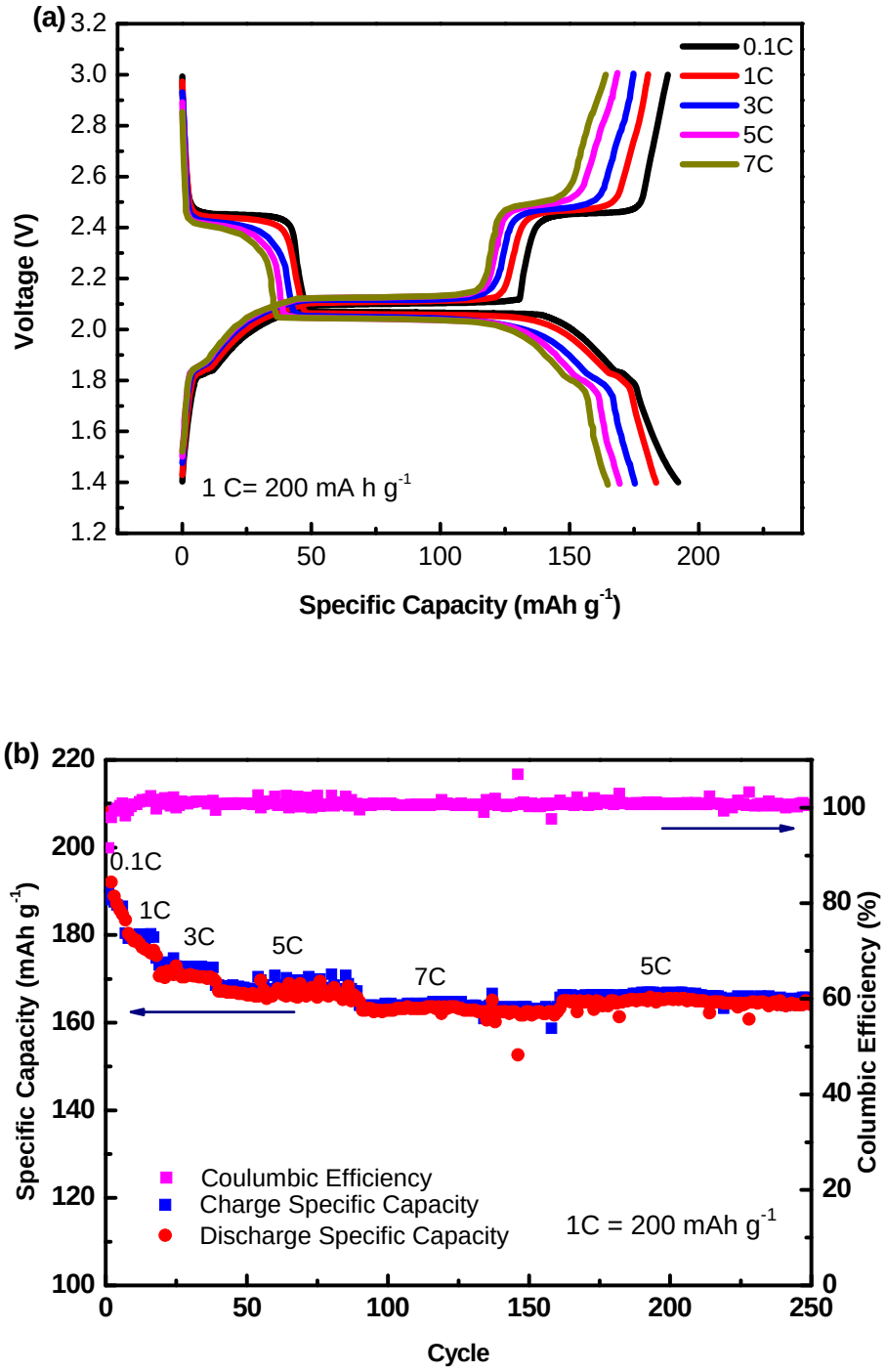

Figure 3-5. The discharge and charge curves of $Li/Li_xMo_6S_8$ cell: (a) rate performance plot, (b) capacity and columbic efficiency plots

Based on the voltage profile in Figure 3-5(a), the three plateaus in discharge curve at 2.46V, 2.1V and 1.8V represent different lithium intercalation processes during cycling. For the case of discharging/charging at a rate of 0.1C, the first plateau at 2.46V correspond to the lithium intercalation range $0<x<1$. The second plateau remains at 2.1V until 75% of discharge process is complete, representing the lithium intercalation range $1<x<3$. The last plateau at 1.8V corresponds to the last 25% discharge process where x ranges between 3 and 4. Figure 3-5(a) illustrates an unusual high specific capacity of 200 $mAhg^{-1}$ under 0.1C discharge rate. As the discharge/charge rate increases, the material shows an extraordinary rate capability. When cycles under 7C, which has a current 70 times of the initial cycle, the reversible specific capacity remains above 160 $mAhg^{-1}$, which is about 80% of the initial capacity under 0.1C. To look deeper in the voltage-specific capacity plot shown in Figure 3-5(a), the capacity loss when increasing the C rate occurs mainly at potential plateaus at 2.4V and 1.8V. The largest plateau at 2.1V retains the capacity well. This can be attributed to the different ionic conductivity of the $Li_xMo_6S_8$ CP material. The $Li_1Mo_6S_8$ material at 2.4V and $Li_4Mo_6S_8$ material at 1.8V have lower Li ionic conductivity that lead to higher electric polarization of the CP material under larger charging/discharging currents. The electric polarization creates an inner electric field that pushes the potential away from its equilibrium potential. With the increasing of the electric polarization, the potential is further pushed away from the equilibrium potential. When the charging/discharging process reaches the same cutoff potential, a more severe decrease of capacity can be observed compared to the process with less polarization.

Figure 3-5(b) illustrates the excellent cycling stability proved by repeated charge-discharge

rates and long term cycling. For example, after 250 cycles the capacity still remains very stable and the columbic efficiency still remains nearly 100%. After cycling under 7C rate for more than 50 cycles, then reducing the discharge/charge rate from 7C to 5C, the capacity can recover to the same level of the previous 5C cycling. It proves the excellent structural stability of $Li_xMo_6S_8$ CP material after long cycling and under higher C rates. This can be attributed to the open frame structures of CP with big vacancies that allow the expansion during Li ion insertion and extraction processes, without breaking down the frame structure.

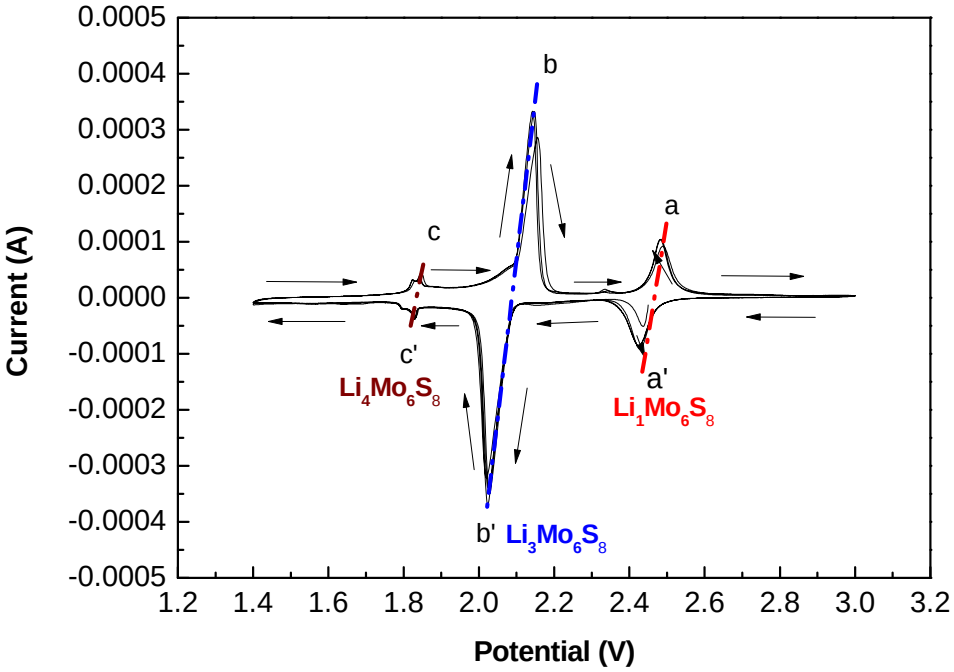

Figure 3-6. Cyclic voltammetry test of Li/Li$_x$Mo$_6$S$_8$ cell

The cyclic voltammetry test of Li/$Li_xMo_6S_8$ shown in Figure 3-6 illustrated three reversible redox peaks (*a/a'*, *b/b'* and *c/c'*), representing three phases of lithium intercalation into $Li_xMo_6S_8$

Chevrel phase host. For discharge process, the reactions take place at points *1*, *2* and *3* (shown below in Figure 3-7) can be expressed in Reactions 3-2 to 3-4, respectively [48, 53].

$$Li^+ + e^- + Mo_6S_8 = Li_1Mo_6S_8 \qquad (3-2)$$

$$2Li^+ + 2e^- + Li_1Mo_6S_8 = Li_3Mo_6S_8 \qquad (3-3)$$

$$Li^+ + e^- + Li_3Mo_6S_8 = Li_4Mo_6S_8 \qquad (3-4)$$

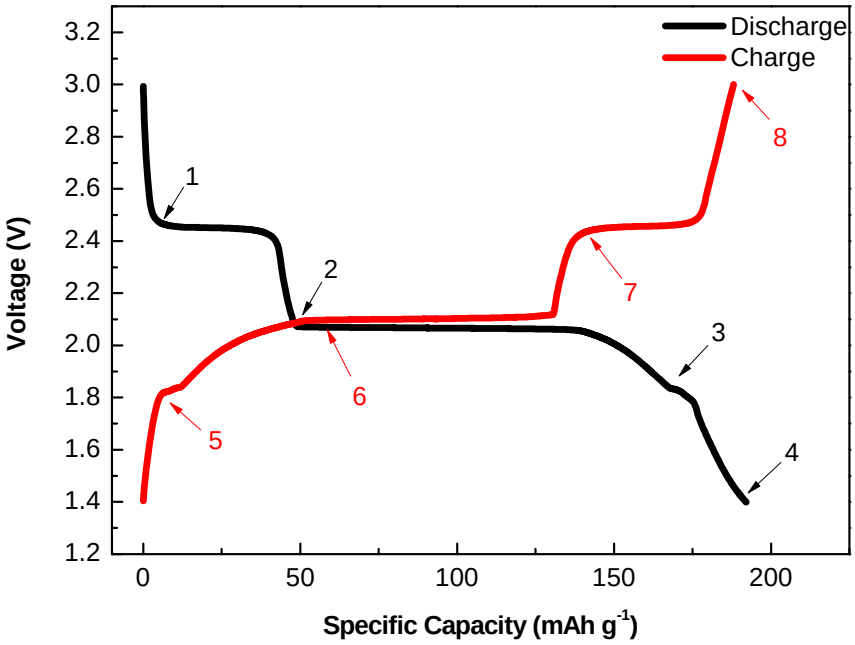

Figure 3-7. Voltage— specific capacity profile of Li/$Li_xMo_6S_8$ cell cycled under the rate of 0.1C.

Figure 3-7 shows a typical voltage— specific capacity profile of Li/$Li_xMo_6S_8$ cell cycled under the rate of 0.1C. Points of interests are selected for electrochemical impedance spectroscopy (EIS) measurement for the investigation of lithium transportation processes. At one of the points, the charge or discharge process was halted and the EIS of the cell was tested.

Points 1 and 2 represent the beginning of Reaction 3.2 and Reaction 3.3, respectively. Points 3 and 4 mark the start and end points of Reaction 3.4.

Figure 3-8 shows the impedance spectroscopy of $Li/Li_xMo_6S_8$ cell during discharge process (inserting of Li ions into Chevrel phase host). Usually in the Nyquist plots, there will be semicircles which reflect the total resistance between the two working electrodes and a steep tail represents differential intercalation capacitance (finite-space Warburg (FSW) element). From Figure 3-8(a), (b) and (c), only one semicircle is observed, which is assigned as high frequency semicircle (HFS). As the discharge proceeds, the radius of semicircle is increasing, indicating an increase of charge transfer resistance during the process, which may be attributed to the blocking of the tunnels when more and more Li ions insert into the host structure and the gradual forming of SEI layer. The formation of the SEI layer is consistent with the appearance of the second semi-circle in Figure 3-8(d) which indicates that Li ions in the Chevrel phase host have reached a certain level that creates another pair of resistance and capacitance.

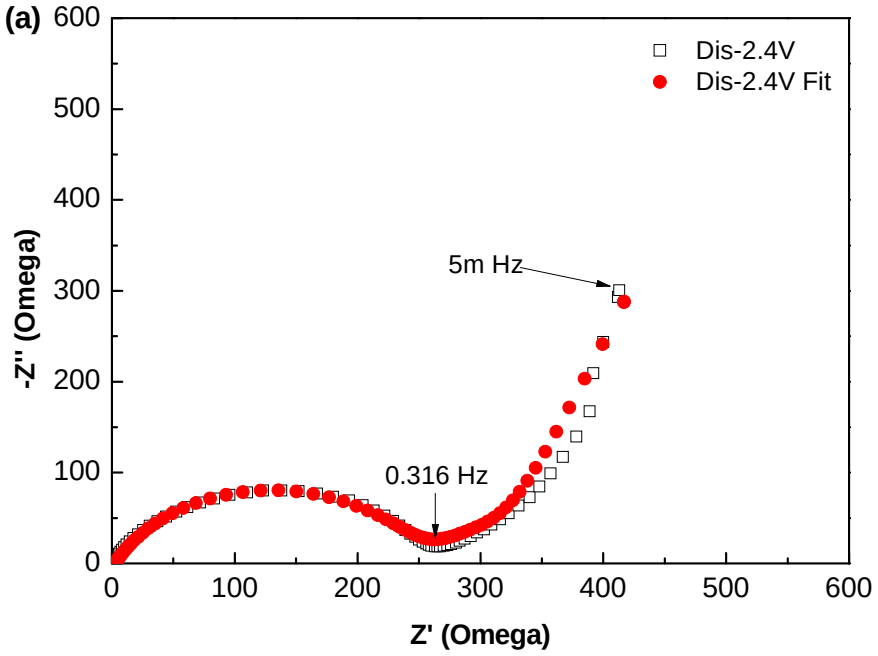
(a)
Dis-2.4V
Dis-2.4V Fit
5m Hz
0.316 Hz
-Z'' (Omega)
Z' (Omega)
0
100
200
300
400
500
600

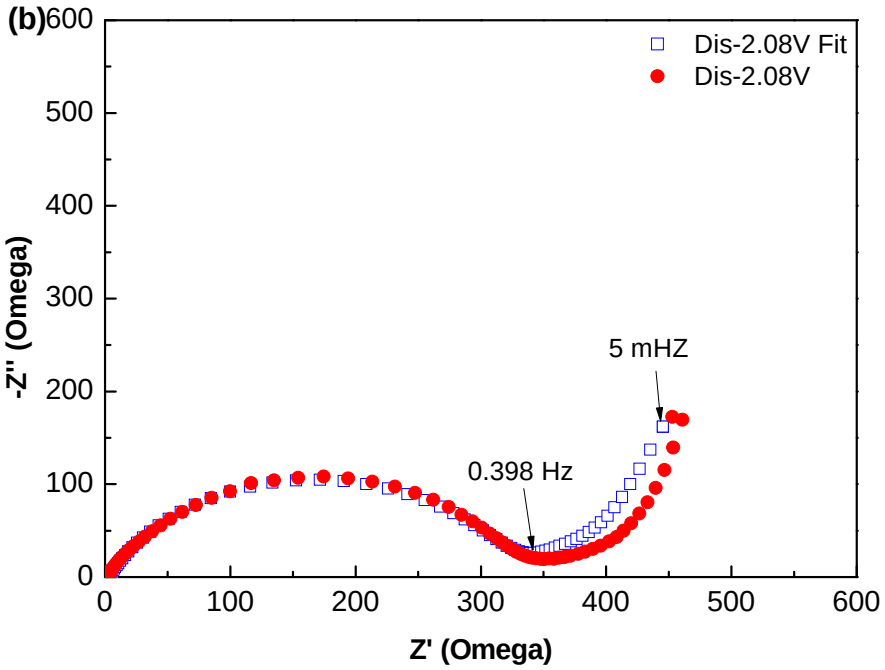
(b)
Dis-2.08V Fit
Dis-2.08V
5 mHZ
0.398 Hz
-Z'' (Omega)
Z' (Omega)
0
100
200
300
400
500
600

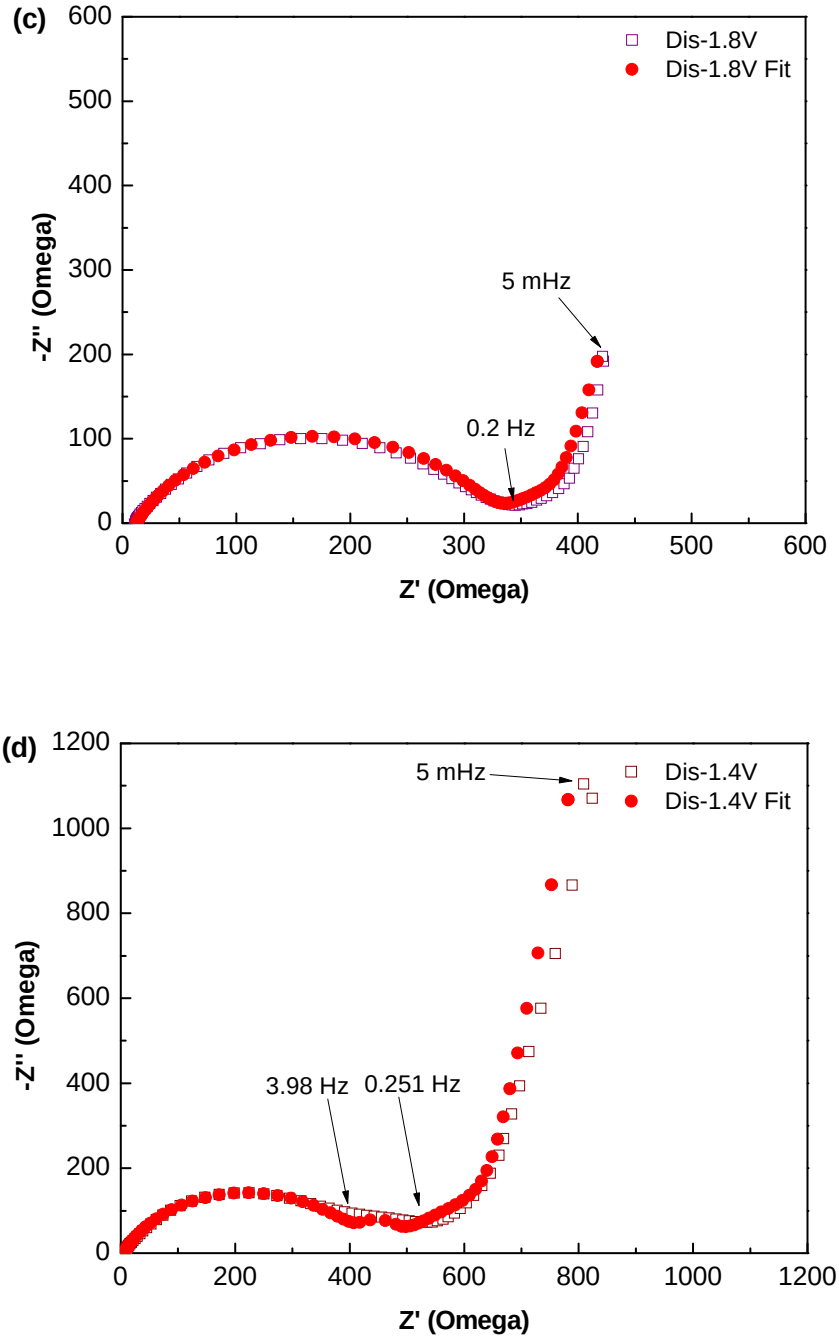

Figure 3-8. Detailed Nyquist plots of impedance spectroscopy and fitting results of Li/$Li_xMo_6S_8$ cell for Li-ion insertion into the Chevrel electrode (discharge process): (a) discharge to 2.4V; (b) discharge to 2.08V; (c) discharge to 1.8V; and (d) discharge to 1.4V.

The EIS spectra can be fitted with establishing equivalent electrical circuit diagrams. The equivalent electrical circuit diagram comprises a serial combination of the solution resistance *Rs*, the ion-charge transfers constant phase element (CPE) and resistance pair (CPE1 and R1) and a finite-space Warburg (FSW) element represents the ion diffusion. When there is a second semicircle, another CPE and resistance pair (CPE2 and R2) can be used [54]. For the impedance spectra in Figure 3-8(a), (b) and (c) are fitted with one-semicircle model (Figure 3-9(a)) while (d) is fitted with two semicircles model (Figure 3-9(b)). The fitting result is summarized in Figure 3-10.

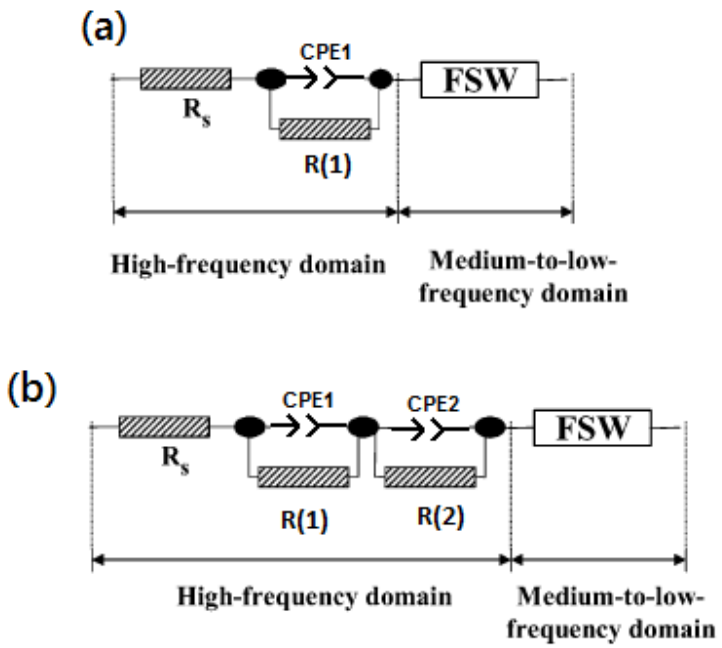

Figure 3-9. Equivalent electrical circuit diagram of impedance spectrum: (a) with one semi-circle; (b) with two semi-circles.

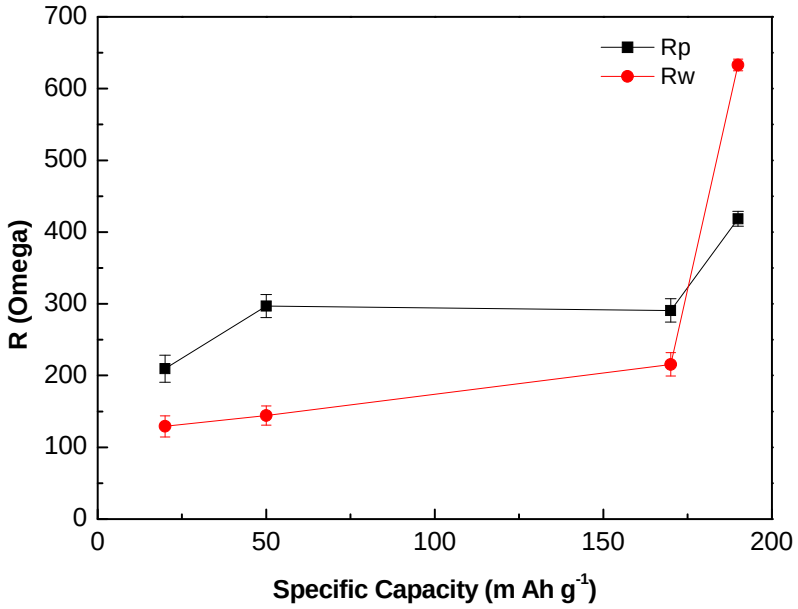

Figure 3-10 Fitting result of EIS spectra during discharge process. *Rp* is the resistance in CPE and resistance pair, *Rw* is resistance in a FSW element.

According to the fitting result, a trend of increasing of resistance in the whole system is observed as the discharge goes further, which agrees well with the prediction that with more Li ions inserted into the host structure, minor change of morphology and more resistance is caused by accumulation of Li ions in CP. The error bar associated with the data points are obtained from the Z-View software during the fitting process, representing the deviation of the fitting result to the original data.

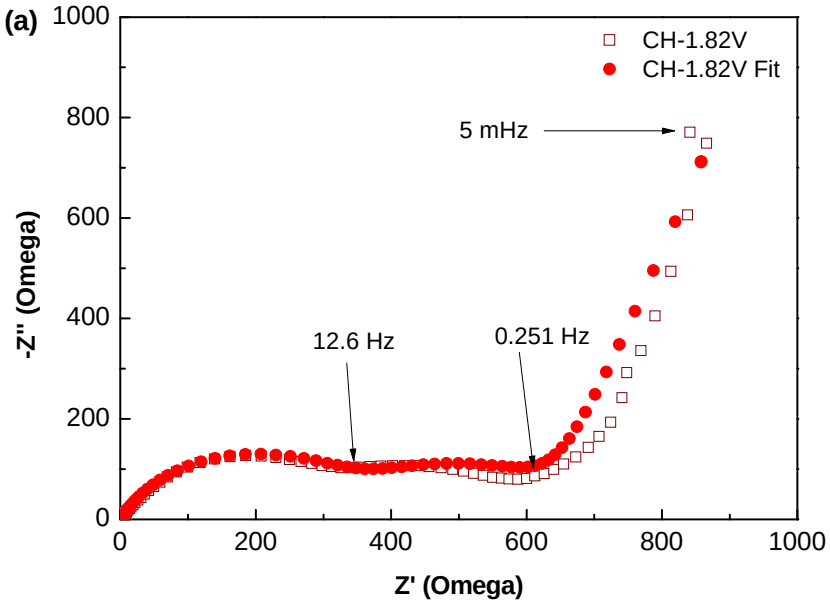
(a)
CH-1.82V
CH-1.82V Fit
5 mHz
12.6 Hz
0.251 Hz
-Z'' (Omega)
Z' (Omega)
0
200
400
600
800
1000

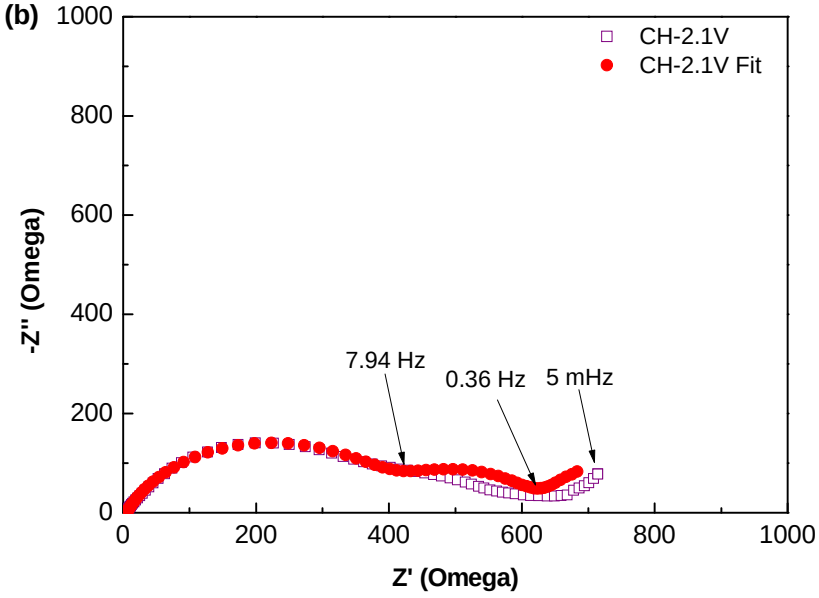
(b)
CH-2.1V
CH-2.1V Fit
7.94 Hz
0.36 Hz
5 mHz
-Z'' (Omega)
Z' (Omega)
0
200
400
600
800
1000

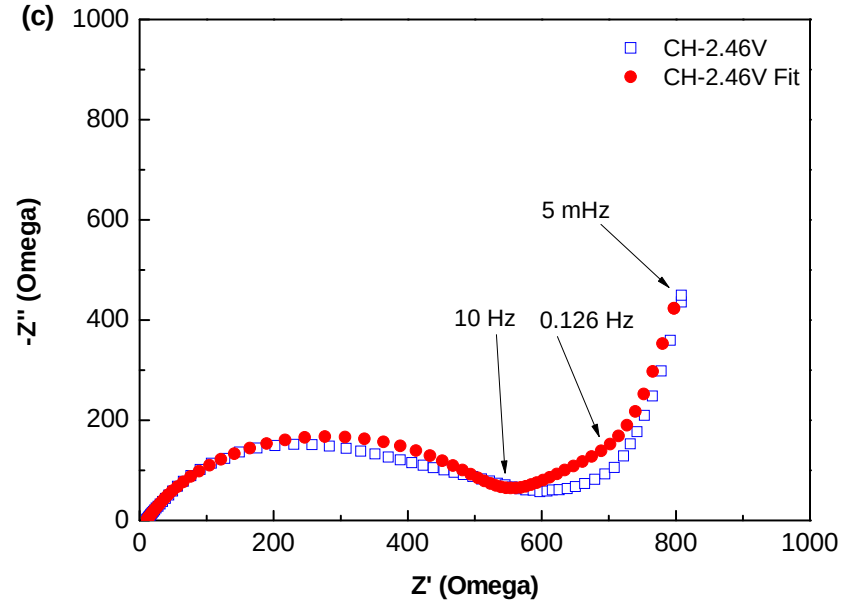

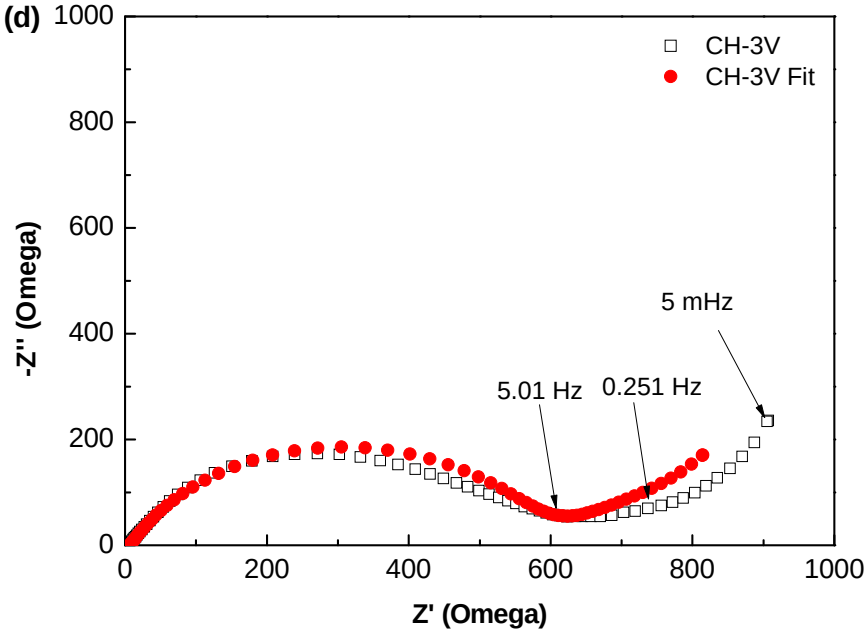

Figure 3-11. Detailed Nyquist plots of impedance spectroscopy and fitting result of Li/$Li_xMo_6S_8$ cell for Li-ion extraction from the Chevrel electrode (charge process): (a) charge to 1.82V; (b) charge to 2.1V; (c) charge to 2.46V; and (d) charge to 3V.

Figure 3-11 shows the EIS spectra and the fitting results of deintercalation of Li ions from $Li_xMo_6S_8$ Chevrel host during the charge process. In the initial process of charging, two semicircles can be observed. As charged to higher potential, the second semi-circle at lower frequency is shrinking and tends to disappear when reaches the second charge plateau around 2.1V where the $Li_3Mo_6S_8$ is formed. In Figure 3-11(c), only one semi-circle can be observed. Although the second semicircle shrinks to an almost straight in the lower frequency region after the first semicircle in (c), the fitting model is still adopted from Figure 3-9(b) so that the resistance of second semicircle can be better simulated. The fitting model for (d) is adopted from Figure 3-9(a) because in this case, the one semicircle model is good enough to provide accurate fitting result with reasonable errors. The fitting result of the charge process is summarized in Figure 3-12.

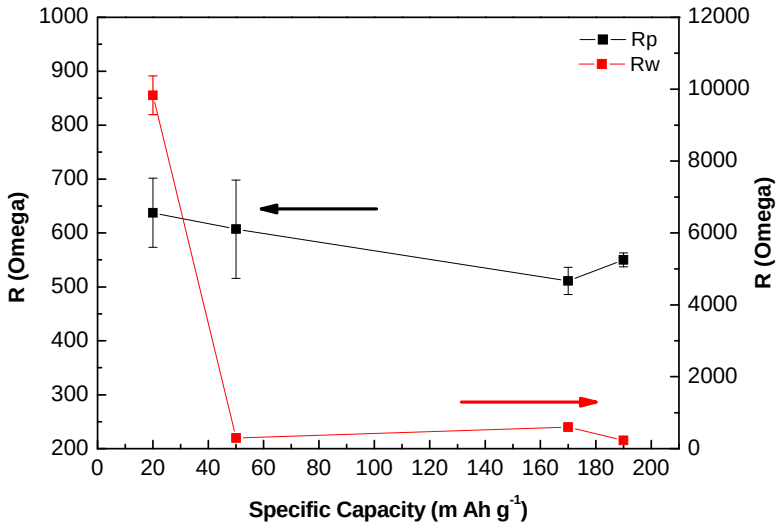

Figure 3-12. Fitting result of EIS spectra during charge process. Rp is the resistance in CPE and Rw is resistance in a FSW element.

As the charge process proceed, the extraction of Li ions from CP host became easier. It can be correlated with the decrease of the Rp and Rw. As noticed that the Rw at 1.82V has a value that is order of magnitude higher, than Rw values at 2.1V, 2.46V and 3V. It is attributed to the difficulty of the extraction of Li ions from the CP host in the early stage of charge process that the host is fully accommodated with Li ions and few vacancies are available as Li pathways. After certain breakthrough point, the Li pathways are successfully established and a sudden decrease of the resistance in FSW element is expected.

After a whole cycle of discharge/charge, the resistance of Chevrel phase for the whole system stabilized and some increase of the resistances between two electrodes can be observed (correlated to the increase of the diameter of semicircle in Nyquist plots). Compared to the initial resistance, the intercalation of Li ions into the host caused some of the structural change. However, due to the open framework structure of Chevrel phase host, the material still remains the structural stability and excellent electronic and ionic conductivity. More detail about the structure change caused by the Li intercalation/deintercalation was studied by XRD and SEM spectroscopy.

3.3.3 Observation of morphology change via SEM imaging

Figure 3-13 illustrated the discharge process in which Li insertion takes place on CP host materials. The cells were halted at the three plateaus (Figure 3-7) during discharge for investigation of phase transformation on each plateau.

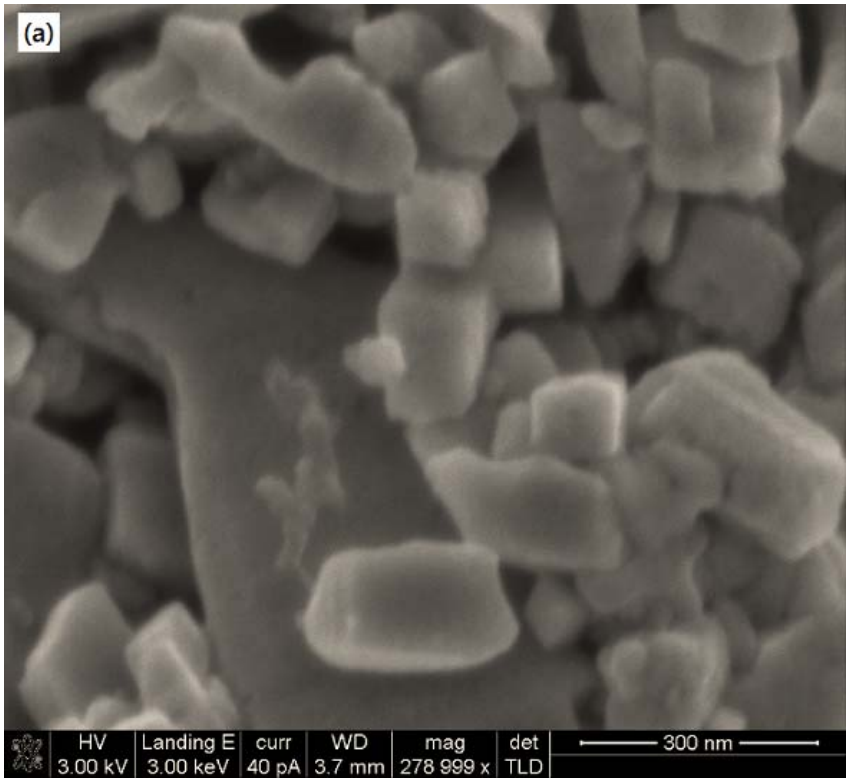
(a)
HV
3.00 kV
Landing E
3.00 keV
curr
40 pA
WD
3.7 mm
mag
278 999 x
det
TLD
300 nm

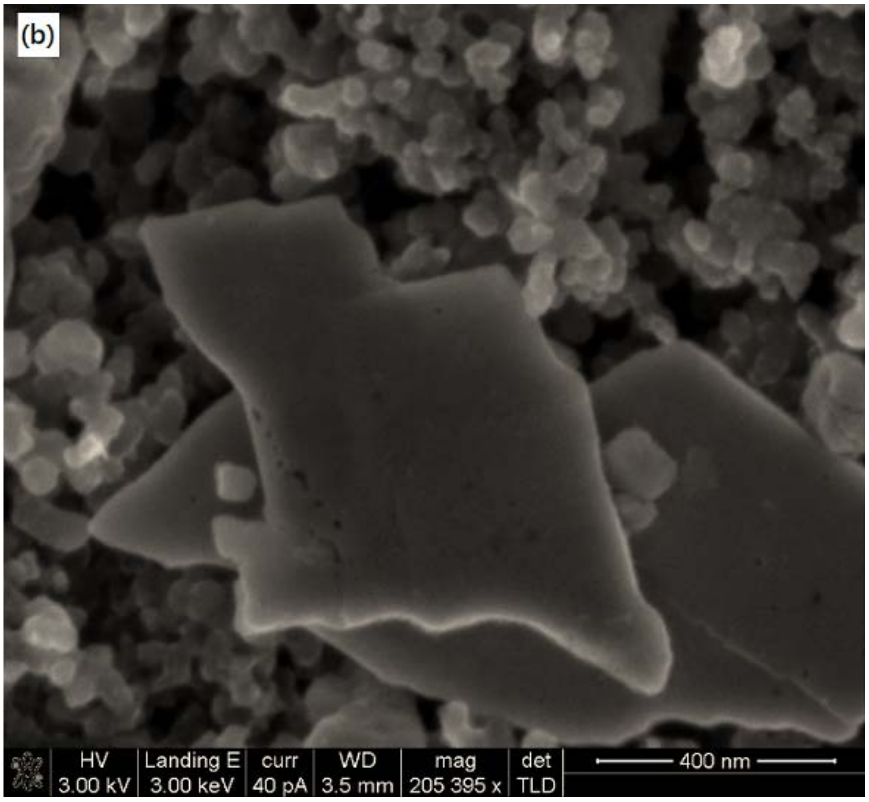
(b)
HV
3.00 kV
Landing E
3.00 keV
curr
40 pA
WD
3.5 mm
mag
205 395 x
det
TLD
400 nm

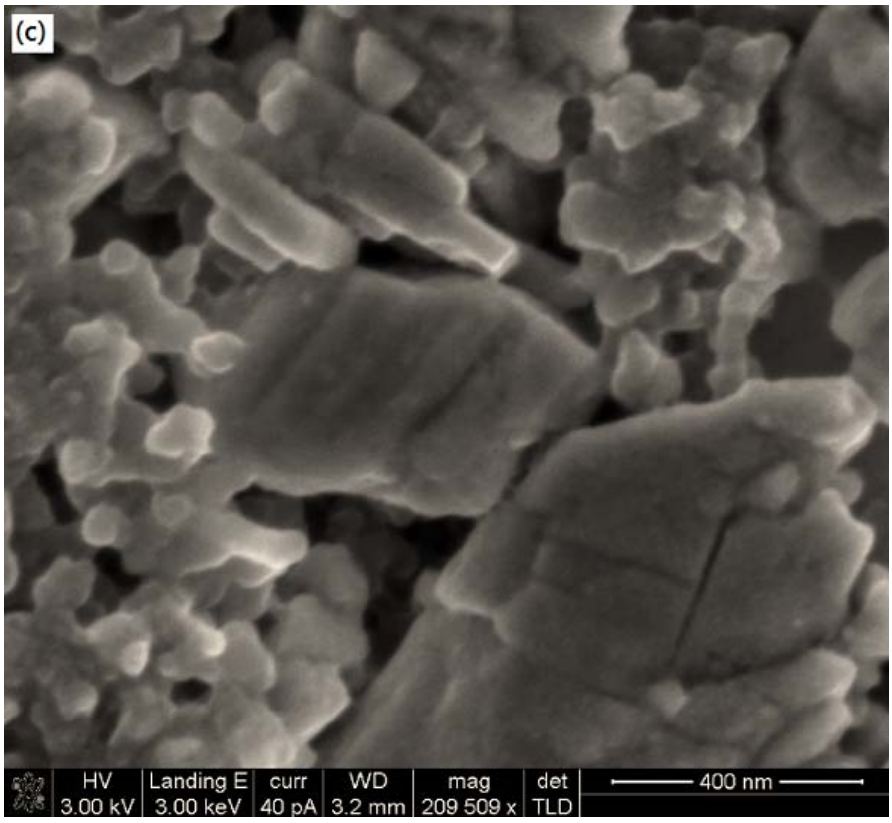

Figure 3-13. SEM images of $Li_xMo_6S_8$ cathode discharged from2.4V to 1.4V: (a) discharge to 2.4V; (b) discharge to 2.03V; and (c) discharge to 1.4V.

From comparison between (a) and (c), which represent the early stage of the Li ion insertion and final stage of the Li ion insertion, respectively, no obvious changes in terms of the particle sizes were observed. However, morphology changes can be observed. After cycling, the surface of the sample became smooth and changed from cubic to less angular. In addition, cracks are observed on the surface of the large particles, which may be caused by repeated Li ion insertion and extraction. The morphology change of the CP leads to the increase of resistance of the grain boundary, which is in good accordance with the impedance data. However, despite the cracks,

CP phase still remains its structural stability that enables its excellent performance in cyclability.

Figure 3-14. illustrated the SEM images of $Li_xMo_6S_8$ cathode during charging process after long cycling (500 cycles). From the large CP particles, hollow micropores were observed on the surface. The micropores could be due to the extraction of Li ions from CP host. However, despite some small morphology changes after cycling, the CP $Li_xMo_6S_8$ material still remains the structural stability that results in its excellent electrochemical performance.

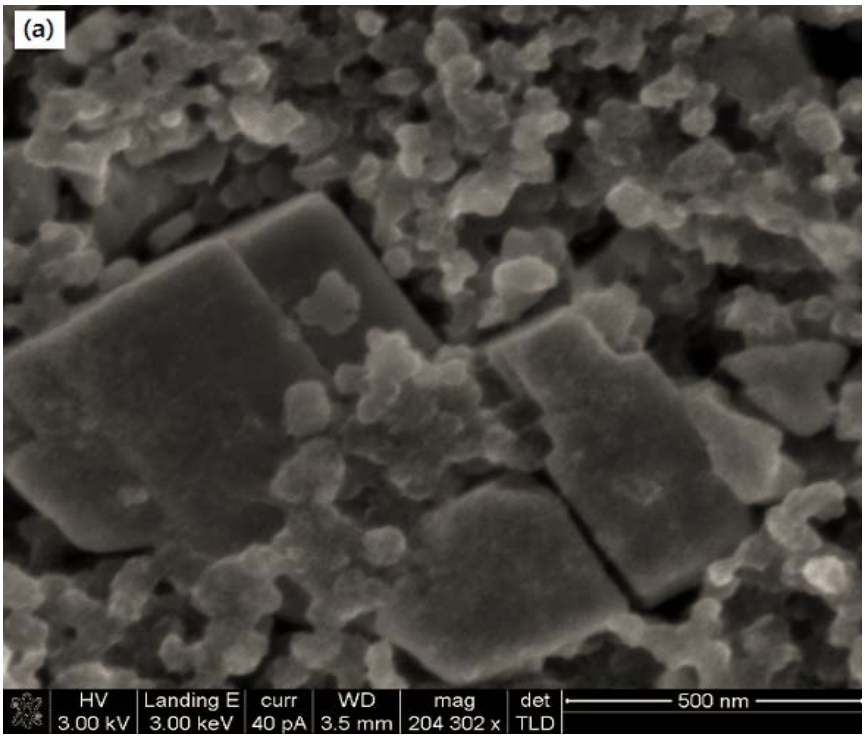

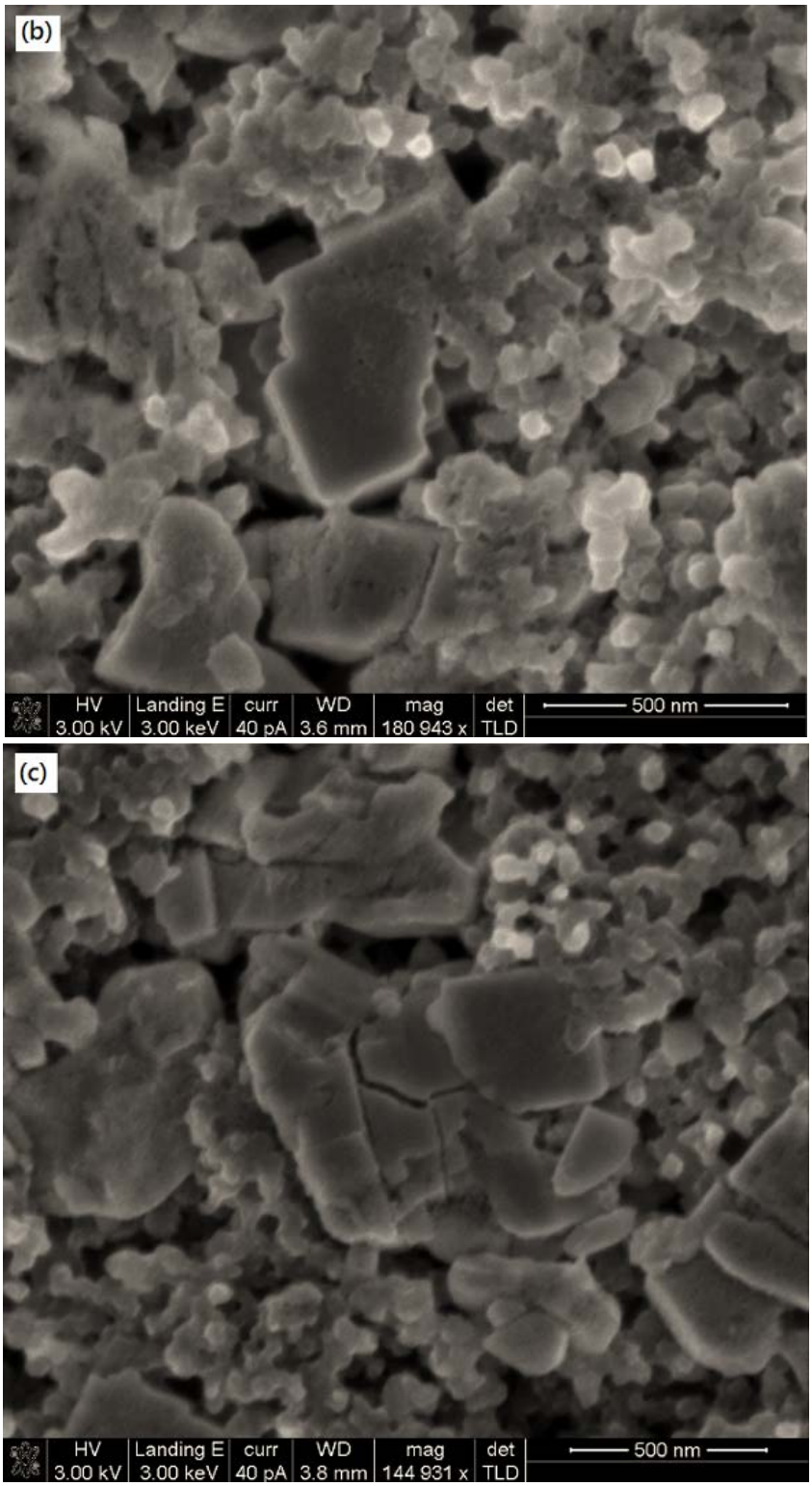

Figure 3-14. SEM images of $Li_xMo_6S_8$ cathode charged from2.1V to 3.0V after long cycling: (a) charge to 2.1V; (b) charge to 2.5V; and (c) charge to 3.0V.

3.3.4 Phase transformation observed from XRD

To test the stability of the material, three samples were tested by XRD. These three samples were basically from the same batch but with different preservation time. Sample 1 was measured right after the synthesis while sample 2 and 3 were measured after 1 month and 3 months later, respectively. The XRD spectra are shown in Figure 3-15.

Interesting findings in XRD results were obtained by comparing samples preserved for several months and the fresh sample. Phase transformations within the $Li_xMo_6S_8$ sample were observed among the three samples with different preservation time. The phase transformation may be the reason for the change of specific capacity of the host Chevrel phase.

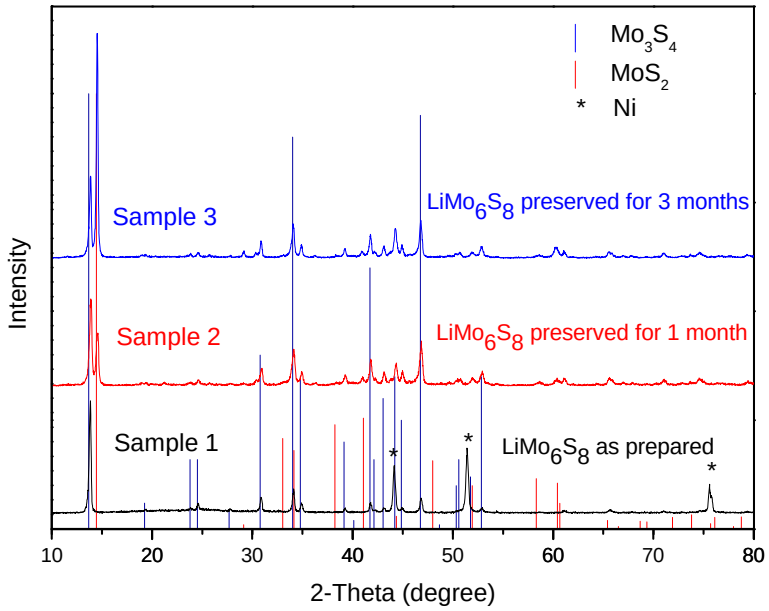

Figure 3-15. XRD analysis of $LixMo_6S_8$ at different preservation time.

After 1 month storage under ambient condition, the sample 2 shows a growth of the MoS_2

phase, which has a strong characteristic diffraction peak at 14.5° corresponding to 6.1 Å for d-spacing for (003) plane. In sample 3, there is an obvious increase of the MoS_2 phase and decrease of the Mo_3S_4 phase. Interestingly, the phase transformation correlates well with the electrochemical performance. Sample 1 has a reversible specific capacity of 200 $mAhg^{-1}$ while samples 2 and 3 have a specific capacity of 110 $mAhg^{-1}$ and 90 $mAhg^{-1}$, respectively. The discharge/charge profiles of these three samples are illustrated below in Figure 3-16.

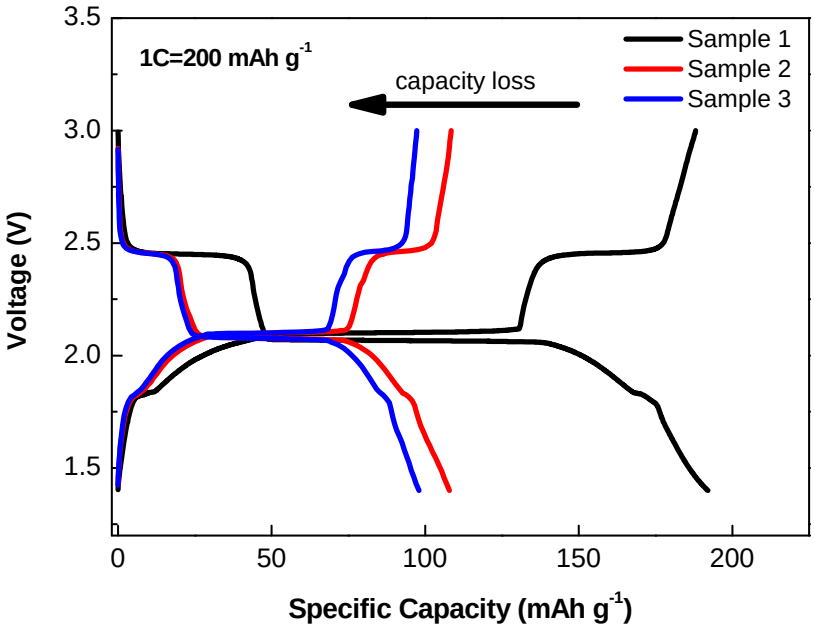

Figure 3-16. Discharge/charge profiles (0.1C) of samples with different storage time in ambient condition

Based on the observation, the $Li_xMo_6S_8$ material appears to be unstable in ambient condition and undergoes a phase transformation from the Chevrel phase to the MoS_2, which is one of the decomposition products. After the decomposition, the host material lost its ability for Li intercalation and thus leads to the reduced specific capacity.

3.3.5 Mo L_3-edge XANES analysis

The XANES spectra (Figure 3-17) were collected on the cathode electrodes that were halted at different discharge/charge plateaus to examine the Mo oxidation states. Electrodes were collected after they were disassemble in the glove box and rinsed several times to wash out the electrolyte. Because the XANES spectra were collected ex-situ, the electrode has to be exposed to the ambient air. When accepting a Li ion into the CP host, the Mo has to decrease the valance to maintain charge neutrality. Since XANES measures the whole sample and yields averaged spectra, we would expect a Mo spectrum with mixed valance.

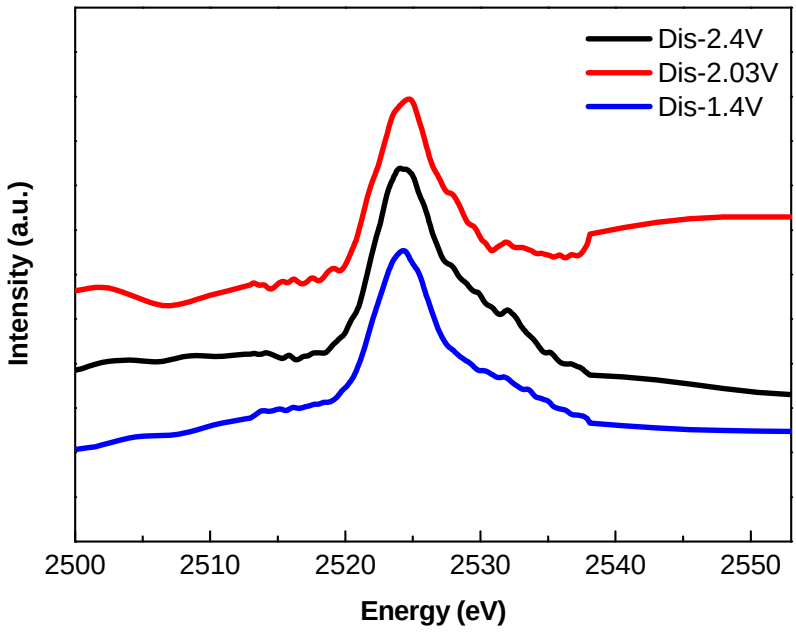

Figure 3-17. Mo L_3-edge XANES spectra on cells stopped at different discharge plateaus.

One explanation is that the Mo species are not stable when exposed to air and the chemical

identity information may be lost. Thus, from the Mo L_3-edge XANES spectra, it is difficult to identify the mixed oxidation states. Another possibility could come from the process of disassembling the cell that the electrode can easily get short-circuited and the voltage and valance is not accurate anymore.

Even with the second derivative of the spectra, the differences among spectra cannot be enlightened due to the significant background noise. Similar results are obtained for the Mo XANES spectra of the charging cells. In the future, an in-situ cell can be used at the X-ray beamline during charge/discharge and without air exposure.

3.4 Conclusion

The Chevrel phase $Li_xMo_6S_8$ has been successfully synthesized via a simple one step molten-salt method. Compared to the traditional ion-exchange method of ternary Chevrel phase material, this synthetic route reduced the high temperature, long calcination time and complex acid leaching process. Extraordinary electrochemical performance of high capacity, long term cycling stability, and rate capability were observed on the material. The EIS test indicates different Li-ion transportation kinetics during the multiple stages of Li ion insertion/extraction processes. The ex-situ SEM observation demonstrates that the synthesized CP phase was stable in morphology during the long term cycling process which is consistent well with its cycling stability. The study indicates that the $Li_xMo_6S_8$ synthesized by a one step molten salt method is a promising cathode material for lithium-ion battery application.

Chapter 4

X-ray Absorption Analysis of Nitrogen Contribution to the Enhanced Performance of Lithium-Sulfur Battery on Mesoporous Carbon Cathode[2]

4.1 Introduction

Lithium-sulfur battery is a very attractive candidate for the next generation lithium battery system due to its high theoretical specific capacity (1,672 $mAhg^{-1}$) [33]. However, it is still far from the commercialization mainly due to the low sulfur conductivity and the low sulfur utilization caused by the shuttle effect [35]. To achieve better conductivity and higher sulfur retention, the development of carbon-sulfur cathode materials gained extensive attention. Carbon became the most widely used conductive additive in the cathode, owing to its high conductivity and the porous structural feasibility for facilitating the redox reaction.

Among various carbon materials, the mesoporous carbon (pore size between 2-50 nm) has been mostly investigated. For the purpose of entrapping sulfur, tunable pore size and pore volume distributions are achieved via different preparation methods. Li et al. have synthesized mesoporous carbon–sulfur materials with various pore sizes (22 nm, 12 nm, 7 nm, and 3 nm) and pore volumes (from 1.3 to 4.8 cm^3g^{-1}) as framework for lithium–sulfur (Li–S) batteries [55]. Different weight ratios of sulfur loading were studied and the result indicated that with a larger

[2] **This Chapter is a manuscript in preparation for submission to Journal of Physical Chemistry C.** (***Zhu, P.***; Song, J.; Lv, D.; Wang, D.; Jaye, C.; Fischer, D.; Wu, T.; Chen, Y., *X-ray Absorption Analysis of Nitrogen Contribution to the Enhanced Performance of Lithium-sulfur Battery on Mesoporous Carbon Cathode.*)

pore volume the mesoporous carbon retained a higher maximum sulfur loading. A sulfur content of 83 wt% was achieved for the 22-nm mesoporous carbon. However, the overall battery performance was very similar for different mesoporous carbon materials at full sulfur-filling conditions. Later, hierarchically structured carbon was introduced by Dudney et al. where they added microporosity of less than 2 nm to the mesoporous carbon with uniformly distributed 7.3 nm pore size [39]. In such configuration, the smaller pores yielded high surface area and were preferentially filled with sulfur while the larger pores were able to confine the sulfur species and provided Li ionic pathway via good contact with electrolyte during the cycles.

Graphene has also become a research hotspot owing to its high conductivity and large surface area. Efforts have been taken into account for utilizing the graphene structure to facilitate the sulfur species as cathode material. In addition to the physical confinement and physical adsorption, chemical adsorption has been found to effectively entrap sulfur species. Oxygen functional groups on graphene oxide (GO) assisted the immobilization of sulfur and polysulfide species within graphene sheets through chemical adsorption [56]. Improved cycling stability and reversible capacity of 950 $mAhg^{-1}$ were reported [57].

Nitrogen doping has already been utilized to modify the property of various carbon materials for broader applications. Usually, doping of heteroatom i.e., nitrogen and boron, alters the charge distribution of neighboring carbon atom which generates an activation region for catalytic activities, i.e., oxygen reduction reaction (ORR) in fuel cells [58, 59]. It was also reported that nitrogen doping created extrinsic defects in the walls of carbon nanotubes (CNTs), serving as tunnels for the Li ion transportation [60]. In addition, the interaction between nitrite

and Li ions can be used to enhance the Li storage capability of the material that yielded high polysulfide retention [61].

Inspired from the advantage of hierarchically structured carbon, nitrogen doping was introduced into the mesoporous carbon material for modifying and enriching the oxygen functionalities on carbon, through which better chemical adsorption can be achieved for sulfur immobilization purpose. In my research group, we reported using hierarchical three-dimensional mesoporous nitrogen-doped carbon as sulfur immobilizer for lithium-sulfur cathodes and observed significant reduction of polysulfide loss during cycles via strong chemical bonding between nitrogen doped carbon and sulfur[3]. A high capacity retention (~800 $mAhg^{-1}$ after 100 cycle @0.1C, 1C=1672 $mAhg^{-1}$) and high coulombic efficiency (~93%) was thus achieved. The mechanism of nitrogen promotion effect is, however, still not clear.

The widely accepted theory of nitrogen promotion was explained mainly by theoretical simulations [59] and electrochemical performance tests. Characterization techniques such as BET, XRD, SEM and TEM were commonly used to provide structural analysis of nitrogen doping. Coupled with electrochemical tests, enhanced performance can be correlated to the increase of high–surface area, thermal stability and good electrical and mechanical properties of materials [60, 62]. X-ray photoelectron spectroscopy (XPS) was reported to identify the nitrogen species and mainly three types of nitrogen species were observed, namely pyridinic, pyrrolic and

[3] **Song, J.; Xu, T.; Gordin, L.M.; Lv, D.; *Zhu, P.*; Jiang, Y-B.; Chen, Y.; Wang D., *Nitrogen-Doped Mesoporous Carbon-Sulfur Nanocomposite Cathodes for Lithium-Sulfur Batteries: Enhanced Performance by Exploiting Chemical Adsorption.* Submitted to *Energy & Environmental Science.***

quaternary nitrogen [63-65]. Theoretical calculation was widely used to support the enhancement of performance with nitrogen doping. For example, Gong et. al used quantum mechanics calculations and hybrid density functional theory to indicate that carbon atoms adjacent to nitrogen dopants possess a substantially high positive charge due to the strong electronic affinity of the nitrogen atom [66]. Through density functional theory (DFT) calculation, Zhang et. al concluded the electron charge transfer between nitrogen and carbon provide active sites for ORR reaction [59]. Niwa et. al has utilized X-ray absorption spectroscopy (XAS) to investigate the nitrogen species at N K-edge in the cathode of polymer electrolyte fuel cell and he found that graphite-like nitrogen exhibit a higher oxygen reduction reaction (ORR) activity than pyridine-like nitrogen [67]. In the present work, X-ray absorption near edge spectroscopy (XANES) on carbon, nitrogen, oxygen and sulfur K-edge is utilized to probe the structural and chemical environmental change of cathode carbon materials. With nitrogen doping, a significant spectra change was found in O K-edge XANES spectra on the carbon materials before and after sulfur loading. S K-edge XANES also confirmed direct chemical bonding between sulfur and oxygen functional groups. Thus, a mechanism investigation of nitrogen doping promoted chemical adsorption of sulfur on carbon material was proposed. XAS is proved to be a powerful technique to provide inaccessible insights for the study of the carbon materials.

4.2 Experimental

The mesoporous carbon (MPC) and mesoporous nitrogen-doped carbon (MPNC) materials were prepared in the lab using poly(melamine-co-formaldehyde) resin (MF, average molecular

weight ~432, 84 wt% in 1-butanol) as polymer precursor, hydrophiphilic and colloidal silica as soft and hard templates. Detailed preparation procedures were published in our previous work[4]. The MPNC-sulfur material was prepared by impregnating sulfur in MPNC at 155 ^{o}C for 10 h with different sulfur loadings. A maximum 5 wt% of sulfur loading was applied to MPC and MPNC samples used in XANES experiments in order to optimize the XANES investigation of the interaction between sulfur and carbon. When naming a sulfur loaded sample, the sulfur content was denoted as a number following S symbol, for example, MPNC-S2 stands for 2% of sulfur loaded on MPNC material. A MPNC-S70 cathode was used for Li-S battery performance evaluation. The composite cathode was prepared by mixing 80 wt% composite powder, 12 wt% Super P, and 8 wt% polyvinylidene fluoride (PVDF) together in N-methyl-2-pyrrolidinone (NMP) to form slurry, which was then coated on an aluminum foil and dried at 80°C for 10 h under vacuum. The electrochemical performance was tested in a half-cell configuration with MPNC-S70 as cathode and lithium chip as anode in 2016 type coin cells. The electrolyte was 1M LiTFSI dissolved in a mixture of 1,3-dioxolane (DOL) and 1,2-dimethoxyethane (DME) (1:1 v/v) and the separator was a microporous polypropylene membrane (25 μm thick, Celgard 2400). Cells were assembled in an argon-filled glove box and the discharge/charge cycles were tested galvanostatically using a battery tester (Arbin BT-2000) at room temperature in a voltage window between 3 V and 1.7 V.

---

[4] **Song, J.; Xu, T.; Gordin, L.M.; Lv, D.; *Zhu, P.*; Jiang, Y-B.; Chen, Y.; Wang D., *Nitrogen-Doped Mesoporous Carbon-Sulfur Nanocomposite Cathodes for Lithium-Sulfur Batteries: Enhanced Performance by Exploiting Chemical Adsorption.* Submitted to *Energy & Environmental Science.***

The C K-edge (284.2 eV), N K-edge (409.9 eV) and O K-edge (543.1 eV) XANES spectra were collected at beamline U7A of National Synchrotron Light Source (NSLS) at Brookhaven National Laboratory. The storage ring was operated with an electron beam energy of 800 MeV and an average current of 600 mA. The XANES spectra were collected in partial electron yield mode with low energy electron compensation to minimize charging effect for poor conductors. The data were processed using Athena [68]. Quantification of oxygen functional groups was performed with O K-edge spectra by a linear combination fitting method that was reported elsewhere [69].

The S K-edge (2472 eV) XANES spectra were collected at beamline of the Materials Research Collaborative Access Team (MRCAT) of Advanced Photon Source (APS) at Argonne National Laboratory. A cryogenic double-crystal Si (111) monochromator was used along with a Rh-coated mirror to reduce harmonics. All spectra were collected in transmission mode with a Si DRIFT 4-element detector (Vortex) providing energy resolution of approximately 0.3 eV at 2.5 keV. Helium purging in the incident light path and the sample chamber was utilized to minimize signal loss through air absorption.

4.3 Results and discussion

The first cycle discharge-charge voltage-capacity profile of MPNS-S70 cathode in a half cell configuration is shown in Figure 4-1(a). The initial discharge specific capacity is 1,200 $mAhg^{-1}$. Note that the specific capacity value was calculated based on the mass of sulfur. Two discharge plateaus at 2.3V and 2.1V are observed, which can be attributed to the transformation

from sulfur (S_8) to Li_2S_n ($6 \leq n \leq 8$) and from Li_2S_n ($6 \leq n \leq 8$) to Li_2S_n ($2 \leq n \leq 6$), respectively [40]. Figure 4-1(b) illustrates excellent cycling stability of MPNC-S70. After about 5 cycles the capacity is stabilized at 800 $mAhg^{-1}$ and the value maintains after 30 cycles. Comparison of cycle performance and columbic efficiency between MPC-S70 and MPNC-S70 were shown in Figure 4-1(b). For MPC-S70 cathode, the initial discharge specific capacity is 1000 $mAhg^{-1}$ and retained at 800 $mAhg^{-1}$ after 5 cycles. The columbic efficiency is retained at 98% for MPNC-S70 whereas, due to the server shuttle effect in MPC-S70, only maximum 90% columbic efficiency can be achieved and sudden dropped to around 80% after first cycle. Evidently, the MPNC nanocomposite can serve as an excellent immobilizer for sulfur and polysulfide species and minimize the shuttle effect for retaining high columbic efficiency during discharge-charge process.

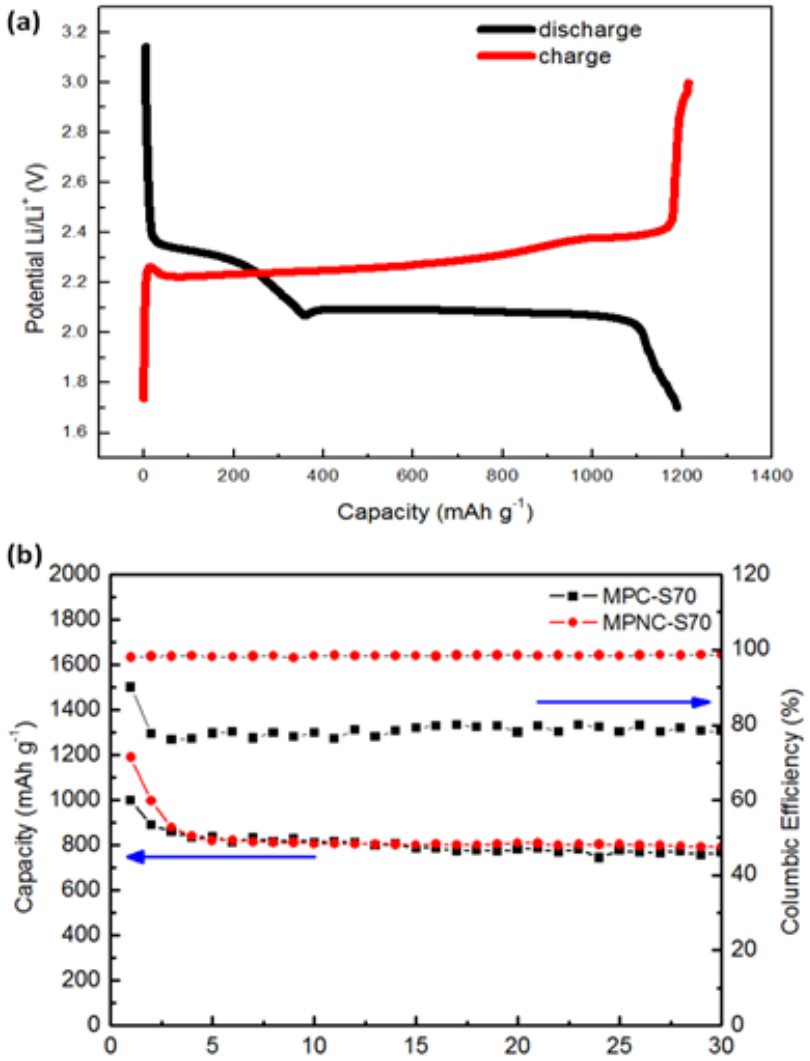

Figure 4-1. (a) First cycle discharge-charge voltage-capacity profile of MPNC-S70 cathode at 0.05C rate; (b) Comparison of cycle performance and columbic efficiency of MPC-S70 and MPNC-S70 (cycled at 0.05C for the first two cycles and 0.1C for subsequent cycles).

The uniform distribution of carbon, nitrogen and sulfur species on MPNC was confirmed by electron energy loss spectroscopy (EELS) elements mapping in TEM from our previous study[5].

[5] **Song, J.; Xu, T.; Gordin, L.M.; Lv, D.; *Zhu, P.*; Jiang, Y-B.; Chen, Y.; Wang D., *Nitrogen-Doped Mesoporous Carbon-Sulfur Nanocomposite Cathodes for Lithium-Sulfur Batteries: Enhanced Performance by Exploiting Chemical Adsorption.* Submitted to *Energy & Environmental Science.***

The highly porous MPNC materials were found to effectively inhibit the diffusion of polysulfide in electrolyte via physical and chemical adsorption. One interesting question is how N doping modifies the performance of carbon electrode. Does it provide additional adsorption sites for polysulfide or it affects the performance indirectly by causing changes in carbon surface functional groups? This question can be addressed by XANES since when there is a strong interaction through chemical adsorption and changes in coordination structure of the adsorption site would occur, which can be readily captured by XANES.

The C K-edge XANES spectra of MPC and MPNC materials are shown in Figure 4-2(a) and a small change of carbon coordination is observed after nitrogen doping on MPC. Compared to MPC spectra, an increase of peak shoulder at 284.8 eV before the whiteline (285.8 eV) in the MPNC spectra indicated that nitrogen doping caused a mild change of chemical coordination in carbon. However, no carbon coordination changes were found after adsorption of sulfur on neither MPC nor MPNC series samples. The N K-edge XANES were also collected on MPNC samples with different sulfur loading to probe the nitrogen coordination structure. According to the result shown in Figure 4-2(b), no noticeable change in nitrogen coordination structure is observed. The results strongly suggested that sulfur does not directly interact with carbon through nitrogen bonding.

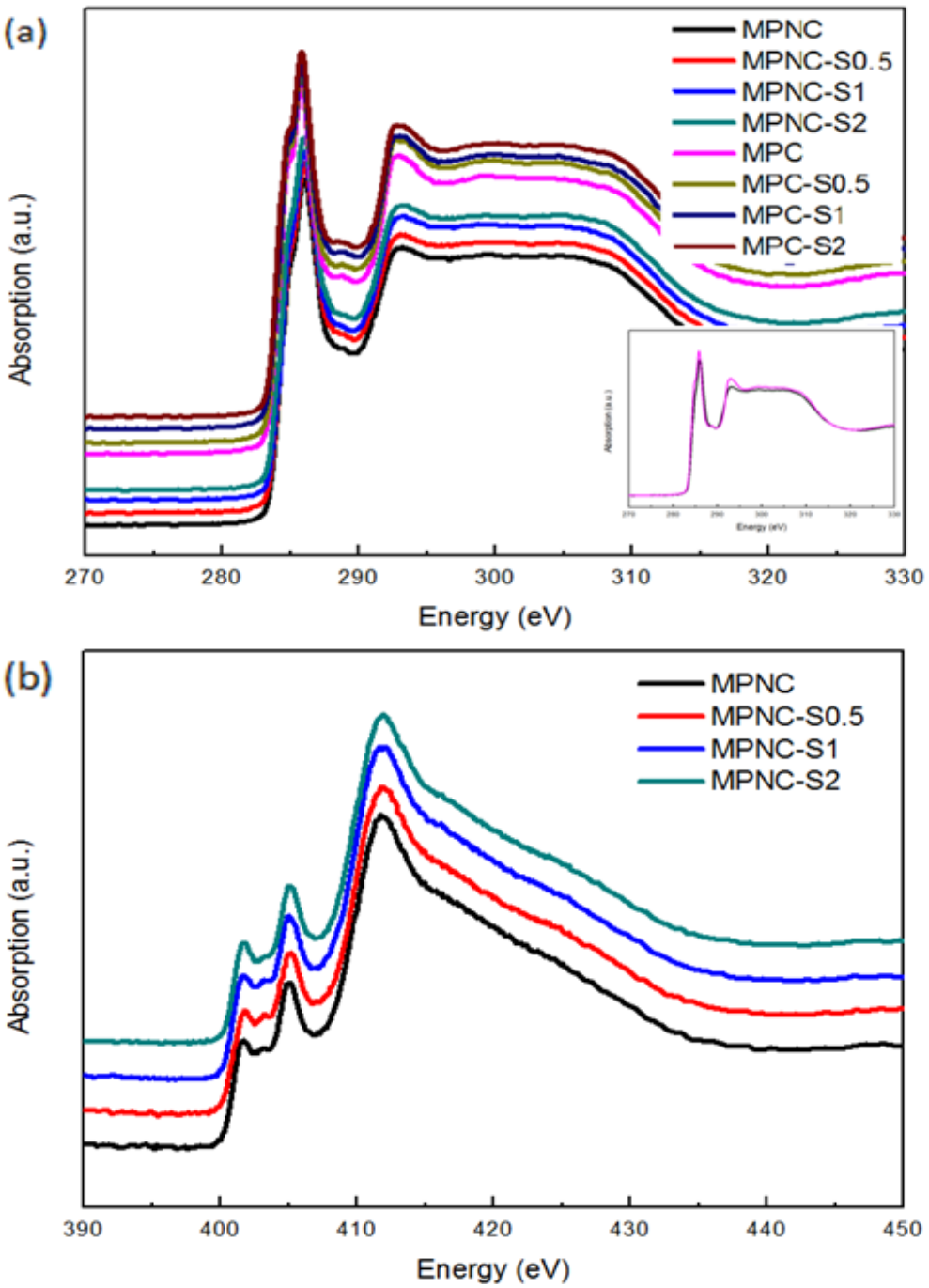

Figure 4-2. (a) C K-edge XANES spectra of MPC-S and MPNC-S composites with different sulfur loadings. Differences of MPC and MPNC spectra are high lightened in small box; (b) N K-edge XANES spectra of MPNC-S composites with different sulfur loadings. Enlightened differences are shown in small box between most contrast samples.

As shown in Figure 4-3, O K-edge XANES spectra reveal a shift of white line with increasing sulfur loadings on MPNC materials, whereas no similar trend is observed on MPC materials. For MPNC-S2 and MPNC samples, the pre-edge peaks remained at 531.1 eV while the whiteline showed up at 538.8 eV and 540.9 eV, respectively. The obvious white line shift of 2 eV strongly suggested a change of oxygen coordination structure when MPNC materials interact with sulfur, implying directly chemical bonding between oxygen and sulfur. In contrast, without nitrogen doping, there is basically no change in oxygen functional groups on MPC materials with different sulfur loading (Figure 4-3(a)). The results suggest that nitrogen doping affects the performance indirectly by making carbon surface functional groups more reactive towards sulfur.

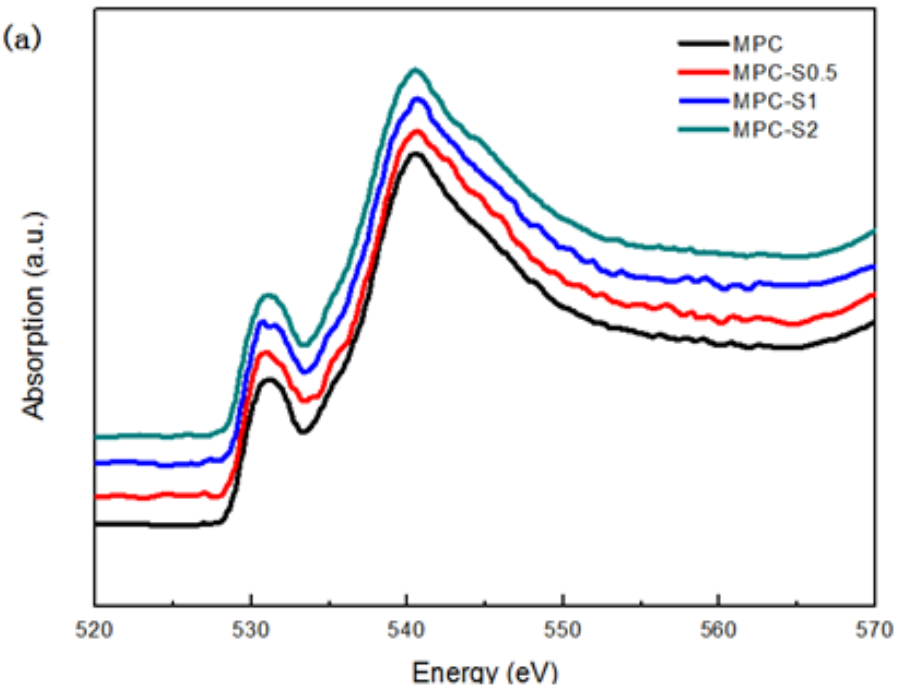

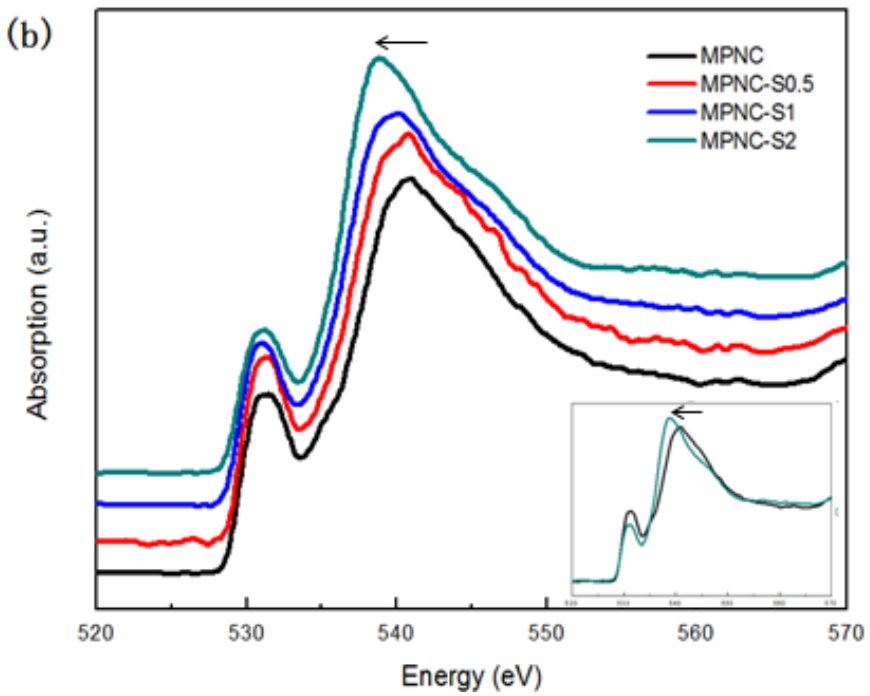

Figure 4-3. (a) O K-edge XANES spectra of MPC composites with different sulfur loadings; (b) O K-edge XANES spectra of MPNC composites with different sulfur loadings. The spectra are offset for better view. The inset shows aligned spectra of MPNC and MPNC-S2 for better comparison.

In the previous work, a method using O K-edge XANES spectroscopy to identify and quantify the oxygen containing surface functional groups on active carbon materials was developed [69]. Oxygen functional groups are grouped into three types, namely carboxyl-type, carbonyl-type, and hydroxyl-type (ether-type), and their abundance is quantified by linear combination fitting. Here I apply the method to the O K-edge spectra, and quantify the oxygen functional groups on MPNC before and after sulfur loading.

As shown in Figure 4-4, the LCF was performed on O K-edge spectra on samples with most contrast, namely MPNC and MPNC-S2, with a fitting range from 10 eV before the edge to 25 eV beyond the edge, covering all pre-edge peaks and the characteristic white line region.

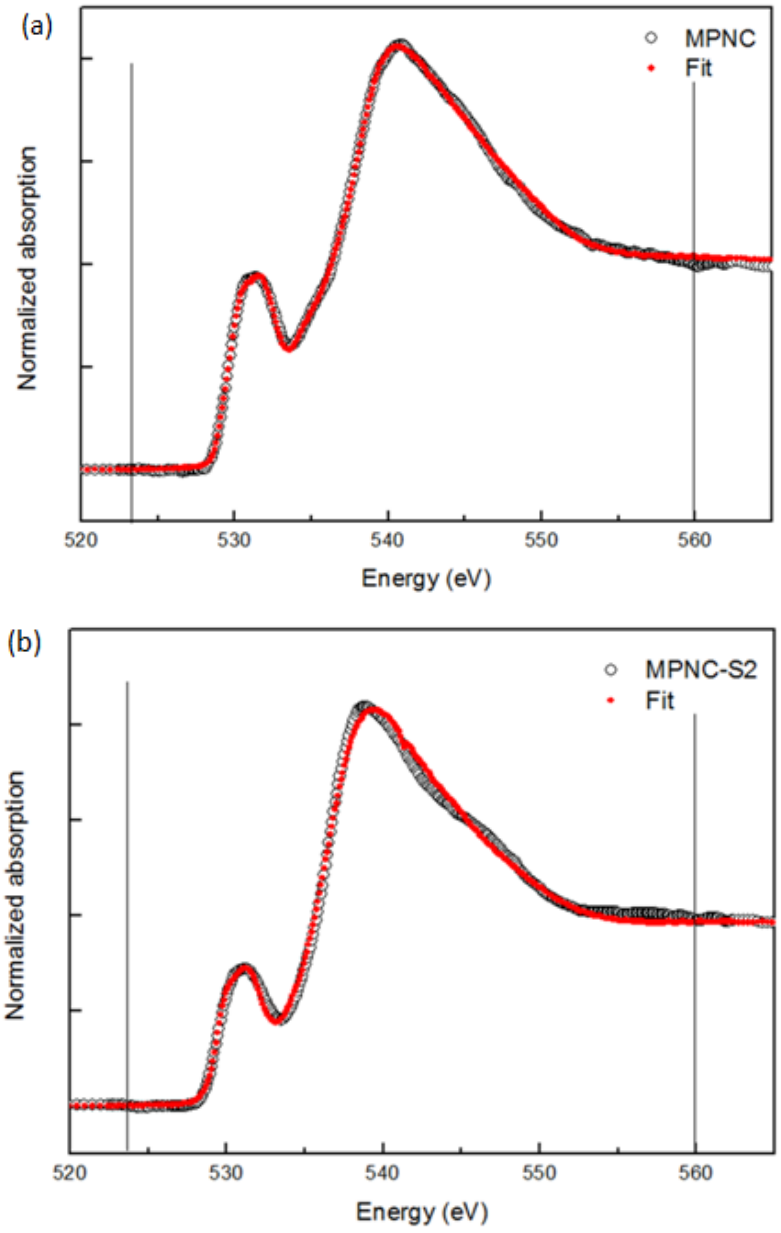

Figure 4-4. (a) LCF of O K-edge XANES spectra of MPNC with fitting range shown; (b) LCF of O K-edge XANES spectra of MPNC-S2 composites with fitting range shown.

All spectra, including the references spectra used in the fitting, were normalized to a unity edge step prior to the fitting, ensuring a constant oxygen content level for all the spectra. The fitting result is shown in Table 4-1.

Table 4-1. Abundance of different types of oxygen functional groups in MPNC and MPNC-S2

	MPNC	*MPNC-S2*
Carbonyl-type group[1]	16.0	8.6
Carboxyl-type group[2]	54.9	38.7
Hydroxyl-type group[3]	31.4	48.6
Sum of abundance	102.3	95.9
R-factor	0.00013	0.00085

[1]includes carbonyl, aldehyde, and ketone
[2] includes carboxylic acid, anhydride, and ester (PVCVA).
[3] includes phenolic hydroxyl, aliphatic hydroxyl, and ether

Evidently, a decrease in the abundance of carboxyl-type and carbonyl-type groups (from 54.9% to 38.7% and from 16.0% to 8.6%, respectively) is observed whereas an increase of hydroxyl-type groups from 31.4% to 48.6% is observed after sulfur loading. It appears that the C=O bond in both carboxyl-type and carbonyl-type groups are prone to fracture to C–O– (ether type) and tended to bond with sulfur species. The cleavage of C=O bond in carboxyl group resulted in the transformation to hydroxyl-type groups (most likely C-O-S). This agrees with the

observation of an increase of hydroxyl (ether) groups and decrease of carboxyl group on MPNC-S2 sample. Nitrogen may play an important role in the process. Because of the higher electro-negativity of nitrogen, with its presence in the chemical environment, the electron density on the C=O bond is altered and the bond strength weakened that makes it more vulnerable. As a result, MPNC material can better immobilize sulfur species through C–O– bridges. For MPC samples, without the contribution from nitrogen, no obvious change in oxygen chemical environment is found, suggesting weaker chemical bonding between MPC composites and sulfur species. The proposed process of nitrogen promotion of sulfur chemical adsorption is illustrated in Figure 4-5.

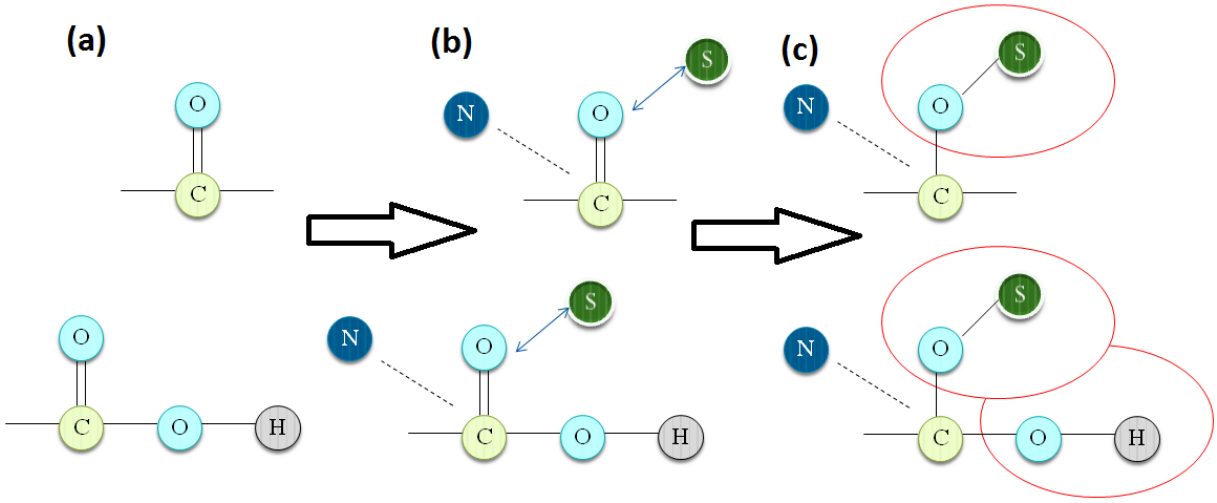

Figure 4-5. Proposed process of nitrogen promotion of sulfur chemical adsorption: (a) Oxygen functional groups on MPC material without nitrogen doping; (b) oxygen functional groups on MPNC material after nitrogen doping; and (c) chemical bonding between oxygen functional groups and sulfur.

Direct evidence of chemical bonding between oxygen and sulfur can be obtained via S K-edge XANES spectra. By comparing with published result of S K-edge XANES spectra, two

peaks (I at 2472.8 eV and II at 2482.8 eV) from Figure 4-6(a) were attributed to elemental sulfur and thiosulfate functional groups, respectively [70]. After normalization, the peak intensity ratio I/II revealed that the majority of sulfur species in MPC were elemental sulfur with small amount of thiosulfate existence. In contrary, in Figure 4-6(b) the presence of big abundant of thiosulfate in MPNC materials indicated a strong chemical adsorption between sulfur and oxygen functional groups. In this case, one sulfur atom anchors the sulfur chain to the carbon surface in the form of SO_3^- via oxygen functional group and the rest sulfur remains in elemental species.

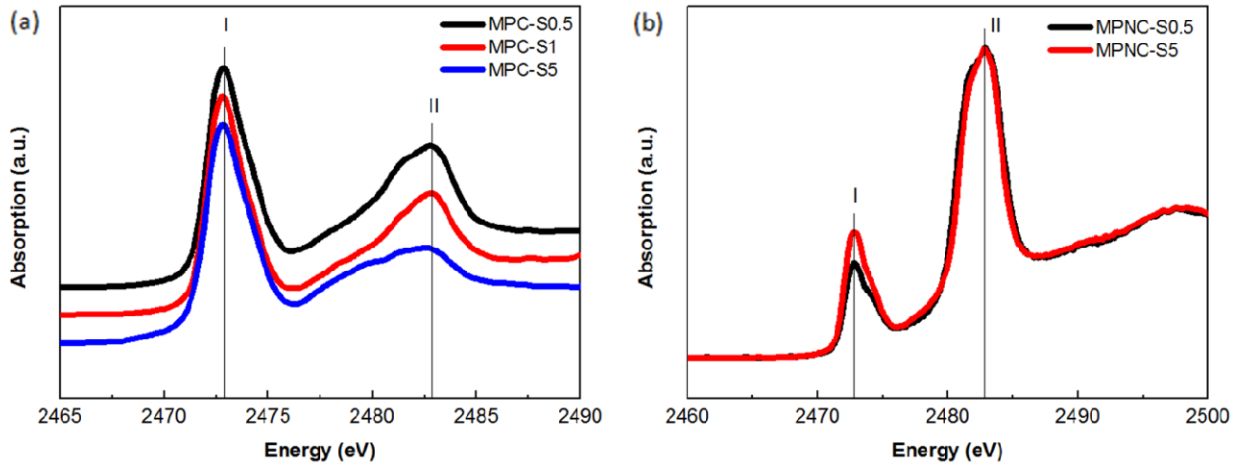

Figure 4-6. (a) Normalized S K-edge XANES spectra of MPC with increasing sulfur loading; (b) Normalized S K-edge XANES spectra of MPNC-S0.5 and MPNC-S2.

By comparing the S K-edge XANES spectra of MPC and MPNC materials, nitrogen promoted chemical adsorption of sulfur on the carbon surface can be directly observed by the phenomenon of significant increase of sulfate abundance, which can be precisely correlated to the observation of white line shift in O K-edge XANES spectra.

The Figure 4-7 shows three main nitrogen species in the nitrogen doped graphene material, among which the pyridinic N and pyrrolic N are the dominant species [71]. Apart from the most common three types, a fourth N species containing oxygen atom (pyridinic^{+}–O^{-}) was also reported in N-graphene and N-CNT studies [72, 73].

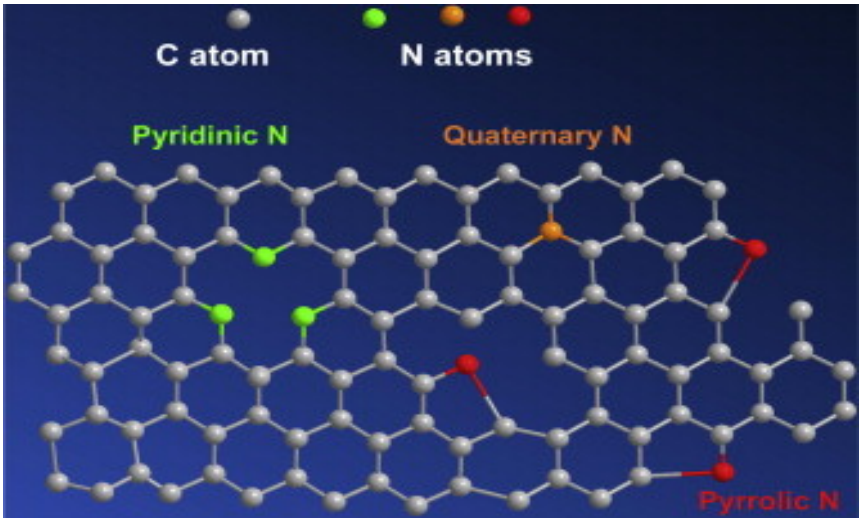

Figure 4-7. Nitrogen species in the nitrogen doped graphene materials. Reprint from Ref. [71].

Although the fourth N species is reported as the minority in terms of N contents, there is possibility that the oxygen atom in the fourth species assisted enhancing the chemical adsorption of sulfur via the formation of the O-S bond.

4.4 Summary

XANES was successfully utilized to probe the chemical environment of MPNC cathode materials for lithium-sulfur battery. A transformation of oxygen functional groups were observed in O K-edge XANES spectra when MPNC materials absorbed sulfur species while MPC materials without nitrogen doping showed no such trend. Chemical bonding between sulfur and

oxygen functional groups were directly monitored via S K-edge XANES. Nitrogen contribution effect was proposed to assist the C=O cleavage and oxygen-sulfur bonding process, which makes MPNC a better sulfur immobilizer material than MPC. The oxygen atom in pyridinic^{+}–O^{-} type nitrogen species may also help to enhance the chemical adsorption of sulfur. XANES was proved to be a powerful technique for quantitative study of oxygen functional groups on carbon materials.

Chapter 5

Conclusions and Recommendations for Future Work

5.1 High performance $Li_xMo_6S_8$ Chevrel phase cathode

One step molten-salt method has been developed for synthesis of the Chevrel phase $Li_xMo_6S_8$ material as cathode material for lithium ion battery application. Extraordinary electrochemical performance of high capacity, long term cycling stability, and rate capability were observed on the material. Transportation kinetics of Li ion insertion/extraction processes in the CP was investigated by EIS spectroscopy. XRD and SEM with EDX spectroscopy were used to correlate the morphology change to the Li ion insertion process. Despite minor morphology change during the cycling, the material shows excellent structural stability during cycling. The phase transformation observed from XRD spectra among the samples with different preservation time may be the reason for the loss of high capacity of $Li_xMo_6S_8$ cathode. $Li_xMo_6S_8$ synthesized through one step molten salt method is not stable in the ambient environment. Storage in inert gas environment is suggested. The study indicates that $Li_xMo_6S_8$ synthesized by a one step molten salt method is a promising cathode material for lithium-ion battery application.

5.2 In-situ XAFS measurement of Li-S battery

For nitrogen doped mesoporous carbon cathode material for lithium-sulfur battery, XANES is successfully utilized to probe the chemical environment for revealing the enhanced chemical adsorption process on the surface. A transformation of oxygen functional groups was observed in

O K-edge XANES spectra when MPNC materials adsorbed sulfur species while MPC materials without nitrogen doping showed no similar change. Chemical bonding between sulfur and oxygen functional groups were directly monitored via S K-edge XANES. Nitrogen promotion effect was proposed to assist the C=O cleavage and oxygen-sulfur bonding process, which makes MPNC a better sulfur immobilizer material than MPC. XANES was proved to be a powerful technique for quantitative study of oxygen functional groups on carbon materials.

5.3 Recommendation for future work

5.3.1 In-situ measurement of $Li_xMo_6S_8$ CP material

Further investigation of the unusual high capacity of $Li_xMo_6S_8$ CP material is recommended. The oxidation states of Mo species in $Li_xMo_6S_8$ CP material at different charge/discharge plateau can be studied by the in-situ XANES measurement. Accurate measurement of the valance of Mo species will help determine the actual amount of Li ions that Mo_6S_8 framework accommodates.

As mentioned in Chapter 3, the Mo species are air sensitive. Air exposure in the ex-situ measurements may chemically change the Mo species thus what is observed in the experiments may not necessarily represent the true Mo species under working conditions. Thus, from the ex-situ Mo L_3-edge XANES spectra, it is difficult to identify the mixed oxidation states. In-situ measurement during charge/discharge process on the X-ray beamline may solve the problem.

A schematic of a sample holder for in-situ XAFS measurement is shown in Figure 5-1. The sample holder is designed for beamline 9-BM at Advanced Photon Source at Argonne National Lab. A hole must be drilled on the cathode cap and should be sealed with Kapton Tape for source

X-ray to enter and for the generated characteristic fluorescence to exit the sample without losing too much intensity. The sample holder will be placed into a chamber continuously purged by helium for XAFS measurement while the coin cell clipped on the holder is tested by the battery tester.

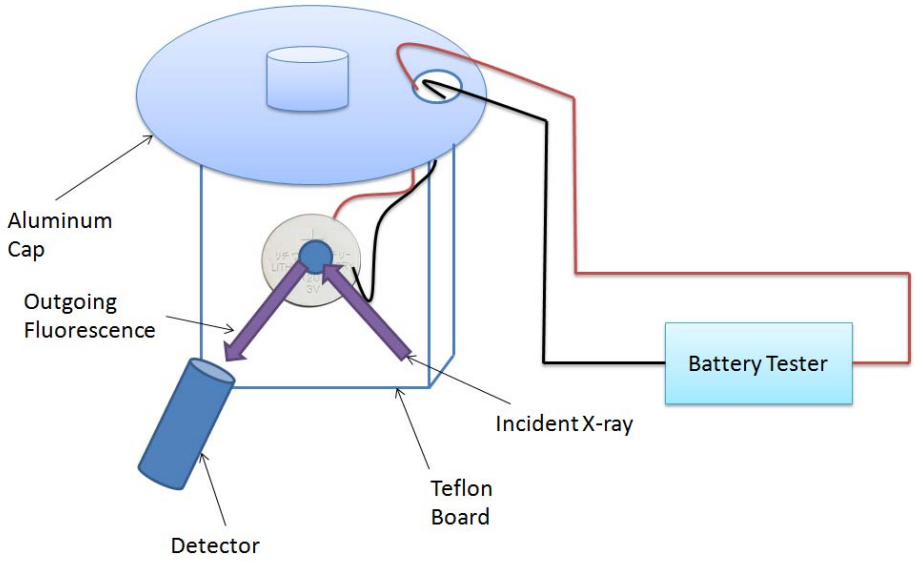

Figure 5-1. Schematic design of sample holder for in-situ XAFS measurement (Argonne Advanced Photon Source Beamline 9-BM).

From the Mo L_3-edge XANES spectra, the Mo coordination symmetry and its oxidation state can be well determined. The pre-edge features resulting from the electron transition and the edge energy may change consequently as electrons move in and out of Mo sites accompanying the Li insertion/extraction process. Thus, the Li insertion/extraction process can be indirectly monitored. In addition, density functional theory (DFT) simulation can be used for establishing the dynamic material structural model of the Li insertion/extraction process to explain the high specific capacity.

5.3.2 Sulfur chemistry in Li-S battery

The nitrogen promotion effect in MPNC cathode for Li-S battery was measured ex-situ on the powder sample. No in-situ XAFS results have been published so far regarding sulfur chemistry in real working condition within a cell, which is essential for revealing the true mechanism for sulfur cathode.

In-situ XAFS measurement on sulfur cathode for Li-S battery can be conducted. The design of sample holder can be the same as the Mo L_3-edge sample holder (shown in Figure 5-1). Special attention should be paid to the constructions inside the coin-cell. At the sulfur K edge energy, the Al current collector should be as thin as possible for X-ray penetration. The spacer used between the cathode cap and the cathode material should be removed to reduce the travel length for the outgoing fluorescence X-ray.

Figure 5-2 shows the plan of the experiments that several points of interest will be examined by the in-situ XAFS. Different point represents different stage of charge/discharge process and different sulfur species are expected (e.g., Li_2S_n $3 \leq n \leq 8$, Li_2S_2, Li_2S and elemental sulfur).

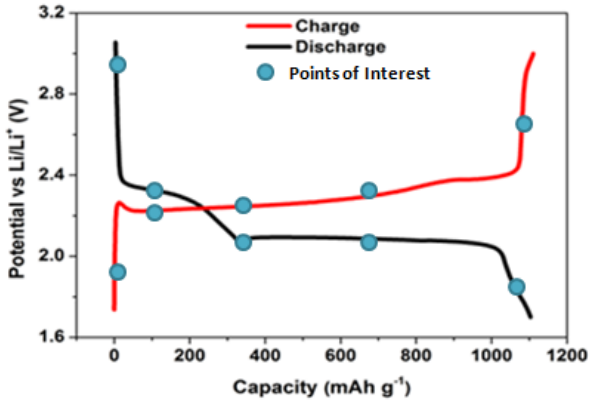

Figure 5-2. A typical first cycle discharge-charge voltage profile of an MPNC-S70 nanocomposite cathode at 0.05C

Figure 5-3 illustrates the comparison of the S K-edge XANES spectra of MPNC-S20 and MPNC-S5 in an in-situ cell and in a powder form, respectively. Although they have different sulfur loading, different sulfur species are observed. The MPNCS-20 sample is assembled into a 2016 coin cell for the XAFS measurement under its open circuit voltage. Although it is not in a charge/discharge working condition when collecting the XANES spectra, it has an environment that is very close to the real working condition, in which the interactions between cathode and electrolyte are present. In the MPNC-S20 sample, less elemental sulfur peak at 2,472 eV was observed and a different peak shown at 2,480 eV, instead of 2,482 eV (sulfate or thiosulfate species) in MPNC-S5 sample. This peak can be interpreted as a sulphonate species (RSO_2O^-) [70, 74].

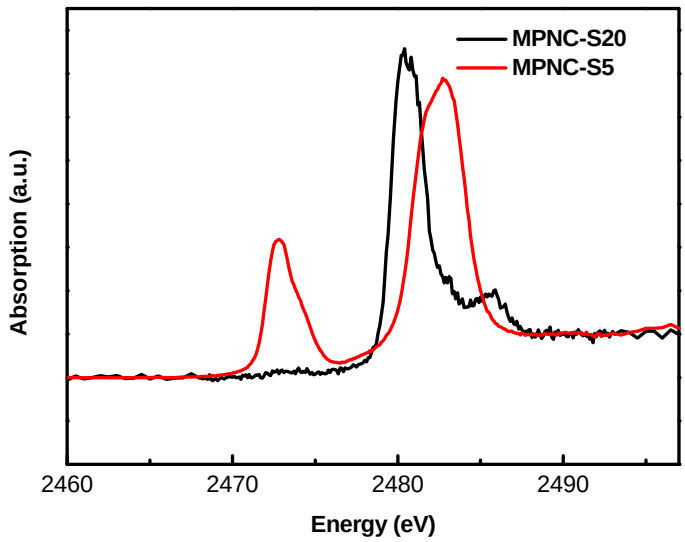

Figure 5-3. Comparison of S K-edge XANES spectra of MPNC-S20 (in-situ cell) and MPNC-S5 (ex-situ powder)

More details of the sulfur species transformation during the charge/discharge process will be

revealed if a complete series of in-situ XAFS spectra can be obtained for a whole cycle of Li-S battery. The interaction between the cathode and intermediate charge/discharge products will be identified. In addition, XANES is recommended for investigating systems that are similar to the nitrogen doped carbon, such as boron and phosphor doping to carbon materials in lithium-sulfur battery system.

Appendix A. EXAFS analysis of ternary nanoalloy catalysts for fuel cell application[6]

A.1 Oxygen reduction reaction reactivity test[7]

Proton exchange membrane fuel cell (PEMFC) is a potential power source for automobile industry due to many advantages, such as high conversion efficiency, low pollution, and high power density. However, the high cost of electrode catalyst, particularly platinum metal used for both anode and cathode materials, hinders its commercialization. The cost of catalysts constitutes about 30% of overall manufacturing cost and efforts have been made to reduce the cost. Due to the structural change during alloying, some platinum alloys with transition metals were found to have better activity than pure Pt in the oxygen reduction reaction (ORR). In the ORR, oxygen gets reduced on the surface of the Pt catalyst to form water molecules (in H^+ environment) or OH^- anions (in base environment). Recently, ternary alloys, such as PtVFe, PtNiFe, PtNiCo, and PtIrCo, have been shown to exhibit much higher electrocatalytic activity than pure Pt [75].

In this work, PtVCo has been chosen as a ternary system mainly based on some of the known facts about the PtV and PtCo bimetallic system, which have enhanced electrocatalytic activities. This work focuses on unraveling the effect of thermochemical treatment temperature on the atomic-scale structure and the catalytic activity [76].

---

[6] This work was published in Chemistry of Materials in 2012 (DOI: 10.1021/cm301613j).

[7] Oxygen reduction reaction reactivity test was performed by collaborator Wanjala et al. at SUNY Binghamton.

Detailed material synthesis procedures can be found in Wanjala, et al. [76]. The cyclic voltammetry (CV) electrochemical measurements were performed on a CHI-620A electrochemical station (CHI 620A, CH Instruments) at room temperature. The potentials are given with respect to the reversible hydrogen electrode (RHE). The CV results were shown in Figure A-1(a) and the rotating disk electrode (RDE) voltammetry were shown in Figure A-1(c).

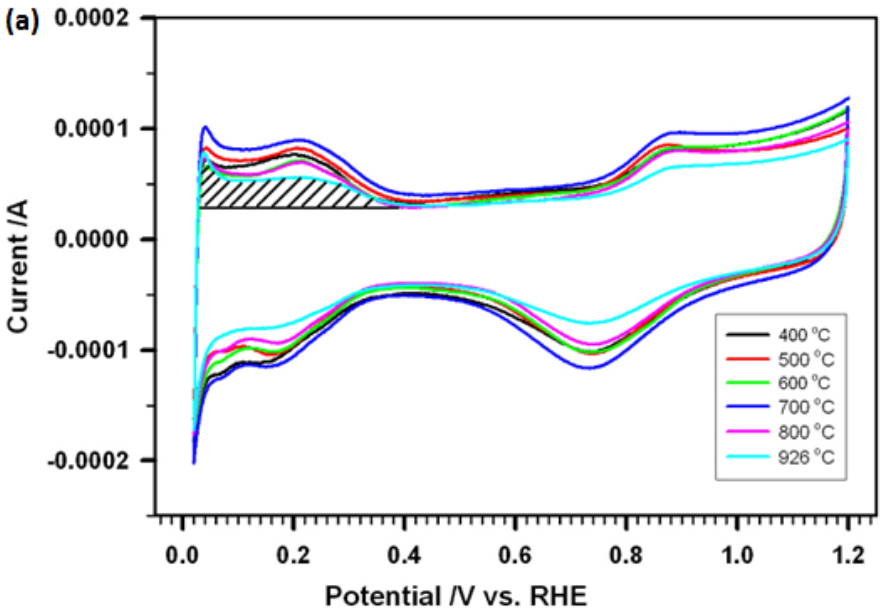

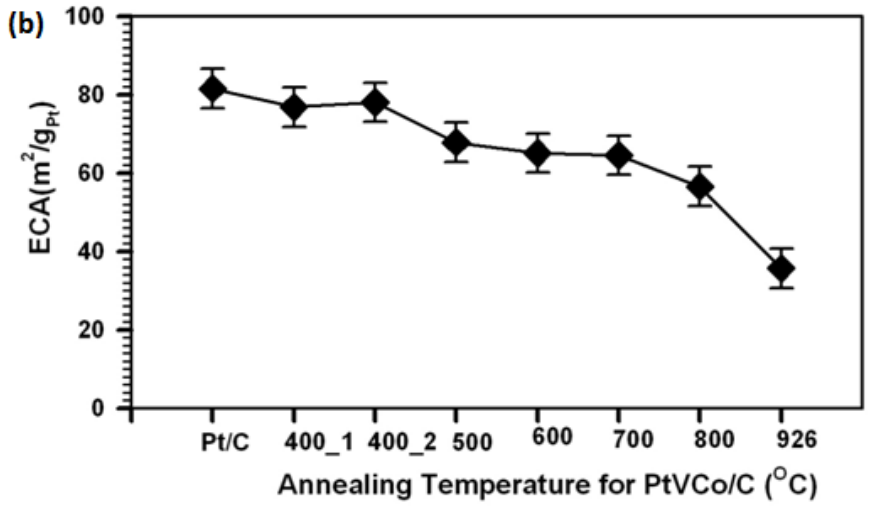

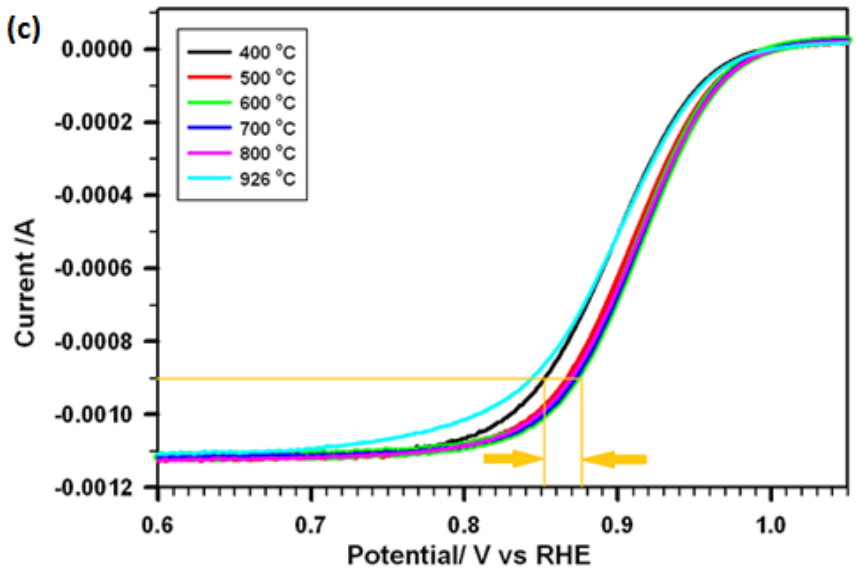

Figure A-1. (a) CV curve for the Pt45V18Co37/C catalysts subjected to "O + H" treatments at different temperatures (400, 500, 600, 700, 800, and 926 °C); (b) Plot of ECA values vs. the annealing temperature; (c) RDE curves for the same catalysts annealed at different temperatures. The potentials are given with respect to the reversible hydrogen electrode (RHE). Reprint from Ref. [76].

In Figure A-1 (a), the CV curves are used to measure the electrochemical active surface area for Pt based catalysts. The peaks at ~0.2 V are attributed to the hydrogen adsorption/desorption peak on the Pt electrode and the area (shown in the shadow) can be used for the estimation of electrochemical active area (ECA). A characteristic value of charge density associated with a monolayer of hydrogen adsorbed on polycrystalline platinum (210 μC/cm^2) is widely used to determine the true surface area of Pt electrodes [77]. The area in the unit of coulomb divided the value of 210 and the mass of the Pt loading yields the ECA value shown in Figure A-1(b). The ECA is one of the parameters for the evaluation of the Pt electrode. Figure A-1(c) shows the rotating disk electrode (RDE) measurement of ORR reactions on Pt electrode with different annealing temperatures. Oxygen reduction starts from ~1.05 V and the ORR proceeds with the

decrease of potential. From Figure A-1(c), at a certain current, e.g., -0.0009, which indicates a same degree of oxygen reduction, Pt electrode treated at 600°C can reduce the oxygen more easily with higher potential (~0.88V) than the electrode treated at 400°C (~0.85V). The potential difference simply means the Pt electrode treated at 600°C has higher ORR activity the electrode treated at 400°C.

This study is to investigate how the thermochemical treatment affects nano-morphology of the catalyst and to correlate the phase transformation to the enhanced electrochemical activity. Thus, the atomic-scale structural and chemical ordering in the nanoalloy catalyst can be manipulated for achieving the ultimate goal of high activity and stability. This work was published in Chemistry of Materials in 2012 [76]. EXAFS is utilized for measuring the coordination structure on Pt, Co and V, respectively. In this part, emphasis is given on the EXAFS measurement and data interpretation.

A.2 Experiment setup and data processing of EXAFS

Pt L_3-edge (11 564 eV) and Co K-edge (7709 eV) XAFS spectra were collected on the insertion device beamline of the Materials Research Collaborative Access Team (MRCAT) at the Advanced Photon Source, Argonne National Laboratory. A cryogenic double-crystal Si (111) monochromator was used along with a Rh-coated mirror to reduce harmonics. All spectra were collected in transmission mode. Powder samples were pressed into pellets with a proper thickness to ensure a good quality of the data. A metal cell with open parallel channels 4 mm in diameter was used. A proper amount of sample was pressed into a self-supporting pellet inside

the channel using a pair of dies. X-ray intensity before and after the pellet samples was measured by ionization chambers filled with N_2. In addition, reference spectra of Pt or Co foils for energy calibration were collected simultaneously, with each scan using an additional ionization chamber. XANES spectra were processed using Athena [68]. EXAFS spectra were extracted using Athena, and fitting of EXAFS data was performed using Artemis [68]. Background removal and edge-step normalization were performed using the AUTOBK program. FEFFIT was then used to fit the EXAFS function using paths for Pt species (Pt−O) as generated by the FEFF code (version 6.0) [78, 79].

The normalized XANES spectra at Pt L_3-edge (a) and chi(k) (b) spectra of Pt45V18Co37/C catalyst under different temperatures were shown in Figure A-2. From the XANES spectra, the two samples show identical chemical oxidation information. Fitting of EXAFS spectra was performed to interpret the different coordination environment of different targeting elements.

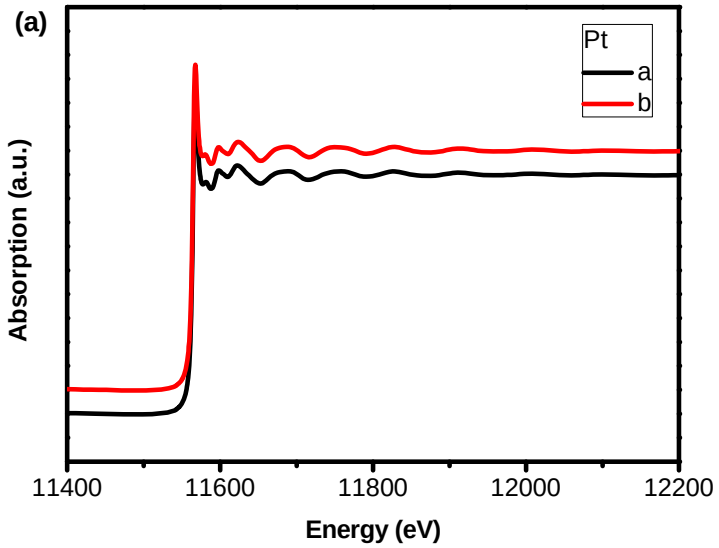

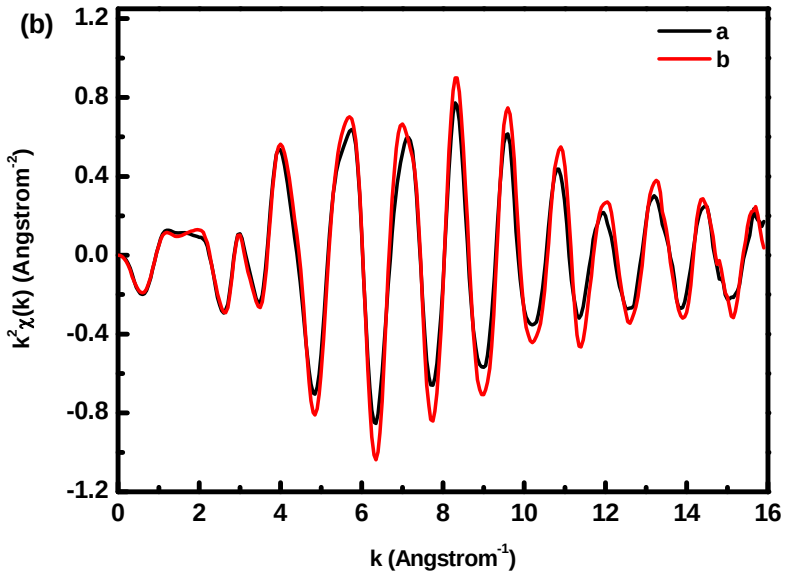

Figure A-2. Normalized XANES spectra at Pt L_3-edge (a) and chi(k) (b) spectra of Pt45V18Co37/C catalysts annealed at two different temperatures: 400 °C (a, black) and 800 °C (b, red).

The mathematical way of describing EXAFS is using the plane wave approximation. The EXAFS expression is shown in Equation A-1 [80]. The symbols and definitions are listed in Table A-1.

$$\chi(k) = \sum_i \frac{F_i(k) S_0^2 N_i}{k R_i^2} e^{-2k^2\sigma_i^2} e^{-\frac{2R_i}{\lambda(k)}} \sin\left(2kR_i + \delta_i(k) - \frac{4}{3}k^3 C_{3,i}\right) \quad \text{(A-1)}$$

Table A-1. Expression of EXAFS oscillations

Symbol	Definition	Obtained from
k	Wavenumber of ejected photoelectron	Theory
R	Bond distance	Fitting
N	Coordination number	Fitting
σ^2	Debye-Waller factor or mean square variation in R	Fitting
S_0	Core-hole or amplitude-reduction factor	Standards
C_3	Anharmonicity of the pair-distribution	Fitting
F(k)	Amplitude	Theory
δ(k)	Phase	Theory
λ(k)	Mean-free-path	Theory

Parameters obtained from theory and fitting result are colored in red and blue, respectively. Value of S_0^2 is obtained from measuring standard sample in advance. The fitting of *k* range was limited to 2.0−16.0 $Å^{-1}$ for the Pt L_3-edge spectra and 2.0−14.0 $Å^{-1}$ (shown in Figure 5-2(b)) for Co K-edge spectra, using a Hanning window of $\Delta k = 1.0$ $Å^{-1}$. The fits were performed to both the real and imaginary parts of $\chi(R)$ in the region of $1.0 < R < 3.2$ Å. Similar analysis was performed on the reference samples of Pt and Co foils to obtain the so-called amplitude reduction factor, S_0^2, used in the subsequent determination of the Me−Me atom first coordination numbers.

Because of the similar atomic radius of Co and V (0.07 Å difference) and the similar atomic

number of Co (27) and V (23), Pt edge EXAFS data were fitted with either O, Co, Pt (PtCo model) or O, V, Pt (PtV model) in the first coordination shell with the understanding that Pt−Co path in PtCo model or Pt−V path in PtV model is used to represent both Pt−Co and Pt−V scattering paths.

The nearest neighbors around Co may include O, Co, V, and Pt. Fittings of Co K-edge EXAFS data were attempted using O, Co, and Pt (CoCo model) or O, V, and Pt (CoV model) in the first coordination shell with the understanding that the Co−Co path in the CoCo model or Co −V path in the CoV model is used to represent both Co−Co and Co−V scattering paths in the samples. Similar to the fitting of Pt EXAFS data, the CoV model resulted in underestimated DWF (~4×10^{-3} Å^2). Thus, to fit Co K-edge EXAFS data in this work, the CoCo model was used. Details of fitting Co K-edge EXAFS data using CoCo model can be found in Wanjala et al. [76].

A.3 EXAFS fitting results

Structural information about the atomic coordination between metals in Pt45V18Co37/C catalysts was also obtained by EXAFS studies on selected samples annealed at 400 and 800 °C. The understanding of the structural changes between these two temperatures provides additional information for assessing how the activity change with annealing temperature is related to the structural change of the catalysts.

Individual fittings of the Pt EXAFS data using the PtCo and PtV models were performed. The PtV model resulted in an underestimated DWF (~3×10^{-3} Å^2) for the Pt−Co/V path (even

smaller than that of Pt−Pt, 6×10^{-3} Å^2), which is a result of fitting the Pt−Co path using Pt−V, as can be shown by a model experiment that was designed to evaluate the impact of using Pt−V to fit the Pt−Co scattering path. In this work, the PtCo model is thus used for the fitting of Pt L_3-edge EXAFS data.

Figure A-3 shows a set of EXAFS spectra data for the Pt L_3-edge. The fitted bond distance and bond disorder for a specific neighbor (e.g., O, Co, and Pt) are basically the same (or not significantly different), leaving the main difference in the coordination numbers. A fit with an apparently smaller DWF of Pt−Co/V than that of Pt−Pt is considered "unreasonable". The fitting results not only show that there are more Pt−Co bonds than Pt−V bonds but also suggest that there are few Pt−V bonds in the system. Note that this type of fitting has been shown to be an effective way to reduce uncertainties associated with the fitted parameters.

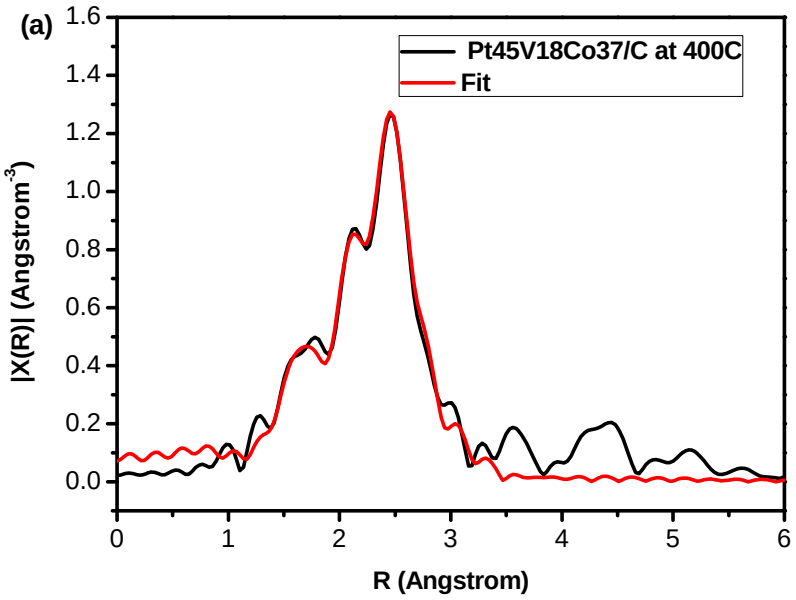

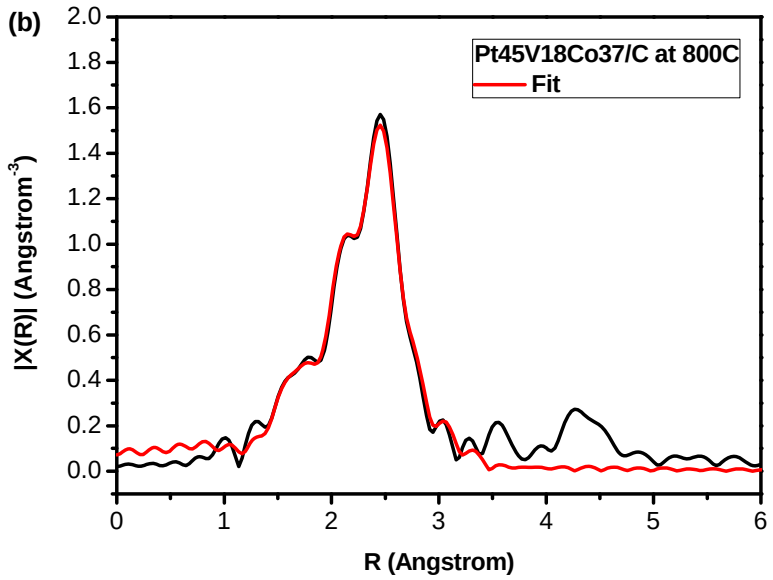

Figure A-3. Original (a, black curve) and fitted (b, red curves) magnitudes of Fourier-transformed k^2-weighted Pt L_3-edge EXAFS spectra of Pt45V18Co37/C annealed at (a) 400 and (b) 800 °C using the PtCo model. Reprint from Ref. [76].

The structural parameters used for fitting Pt L_3-edge EXAFS data in the PtCo model and the Co K-edge data in the CoCo model for the Pt45V18Co37/C catalyst are summarized in Table A-2. The results clearly show a significant presence of Co/V neighbors around Pt and Pt neighbors around Co, which is direct evidence of the formation of PtVCo alloy in the samples studied here. In addition, the EXAFS data indicate a higher probability of Pt bonding with transition metal atoms for the catalyst treated at 800°C, as compared with the catalyst treated at 400°C. For example, the coordination number (CN) of Pt−Co/V atomic pairs changes from 2.3 for the 400 °C-treated sample to 3.1 for the 80 °C sample, whereas the corresponding change in CN of Pt−Pt is insignificant (from 5.7 to 5.4). Although an increase in the particle size may lead to an increase in the total CN, the more significant increase in CN of Pt−Co/V than that of Pt−Pt

suggests better alloying between Pt and Co/V. The EXAFS results in Table A-2 also indicate a clear reduction in the oxide content (e.g., reduction in the metal−oxygen CNs) for the 800 °C-treated sample. The conclusions drawn from the EAXFS analysis are based on both the mean values and the associated uncertainties.

Table A-2. Structural Parameters from Fitting Pt L_3-edge EXAFS Data Using the Pt − Co Model and Co K-edge Data Using the Co − Co Model for Pt45V18Co37/C Catalysts*. Reprint from Ref. [76].

Sample	Scat Path	N	R	DWF(10^{-3} Å^2)
		Pt L_3-edge		
400 °C	Pt-O	0.5 ± 0.1	1.99 ± 0.03	1.5 ± 2.8
	Pt-Co/V	2.3 ± 0.7	2.64 ± 0.01	8.9 ± 2.6
	Pt-Pt	5.7 ± 0.7	2.70 ± 0.01	6.7 ± 0.6
800 °C	Pt-O	0.4 ± 0.1	1.99 ± 0.03	1.5 ± 2.8
	Pt-Co/V	3.1 ± 0.5	2.64 ± 0.01	7.9 ± 1.3
	Pt-Pt	5.4 ± 0.6	2.69 ± 0.00	5.9 ± 0.5
		Co K-edge		
400 °C	Co-O	2.3 ± 0.3	1.99 ± 0.01	10.7 ± 2.4
	Co-Co/V	1.2 ± 0.5	2.62 ± 0.01	12.0 ± 5.1
	Co-Pt	4.1 ± 0.5	2.64 ± 0.01	9.1 ± 1.2
800 °C	Co-O	1.8 ± 0.2	1.99 ± 0.01	10.7 ± 2.4
	Co-Co/V	1.8 ± 0.8	2.62 ± 0.01	12.0 ± 5.1
	Co-Pt	4.9 ± 0.6	2.64 ± 0.01	9.1 ± 1.2

*Note: R factor is 0.0088 for Pt L_3-edges, 0.0127 for Co K-edges. Scat path: scattering path. N: coordination number. R: bond length. DWF: Debye−Waller factor.

A.4 Summary

The EXAFS provides a powerful tool to investigate the ternary catalysts system that can provide information exclusive to other techniques. The change of coordination number and bond distances between different species can be directly utilized as indication of degree of alloying between the components. The controlled oxidative-reductive thermochemical treatment turns the ternary catalyst from disordered state into a more chemically ordered state with higher degree of alloying. The relationship of alloying can be correlated to the activity of ORR reaction. Thus, an optimized thermochemical treatment condition can be applied for better catalyst design.

Appendix B. Mo L_3-edge XANES analysis on Mo based catalyst[8]

B.1 Reactivity of Mo based catalysts for selective oxidation of ethane to aldehydes[9]

One of the major challenges for the petrochemical industry is to manufacture valuable products by oxidizing lower alkanes instead of olefins or aromatics. The direct transformation of methane and ethane to useful olefins and oxygenates has attracted much attention from chemists and chemical engineers for effective utilization of the abundant natural gas resources [81]. Usually, it requires a temperature above 500°C for conversion of ethane due to the low reactivity of its C-H bond. However, the product of conversion of ethane is not stable at such high temperature and is easily to convert to CO and CO_2. Thus, a viable process and effective catalyst for selective oxidation of ethane is needed. Molybdenum and vanadium have been reported for selective oxidation of ethane to formaldehyde and acetaldehyde. It is believed that the selectivity and activity of the catalyst depend on the dispersion, active sites, nature of the support (surface area and pore volume). It is reported that the catalysts, which have dispersed active species and in which the active metals exist in a tetrahedral coordination structure, yield high selectivity to aldehyde [82, 83]. In addition, the catalyst with addition of potassium was found to effectively improve the activity of catalysts and the selectivity to the total aldehydes [84]. The state of active species and the physicochemical properties of the molybdenum-based catalysts are remarkably

[8] **Part of this work was published in Journal of Catalysis in 2012 (DOI:10.1016/j.jcat.2011.09.029) [77].**

[9] **Reactivity test of selective oxidation was performed by collaborator Liu et al. at China University of Petroleum.**

modified by the addition of alkali ions.

In this work, Mo based catalyst supported on SBA-15 were studied for its ability of selective oxidation of ethane to aldehydes. A series of catalyst with different addition of potassium contents on $Mo_{0.75}$/SBA-15 was tested in fixed-bed flow reactor at the reaction temperature from 475°C to 600°C. The detail of catalyst preparation can be found at Liu et. al. [81].

The conversion of ethane, selectivity of aldehyde and the total yields of aldehydes under different temperature were illustrated in Figure B-1. The selective oxidation of ethane to acetaldehyde is shown below in Reaction B-1.

$$CH_3CH_3 + O_2 \rightarrow CH_3CHO + H_2O \qquad \text{(B-1)}$$

For each catalyst, the catalytic activity is measured at six different temperatures from 475°C to 600°C at an interval of 25°C. From Figure 5-4(a), the potassium-free catalyst $Mo_{0.75}$/SBA-15 has higher conversion of ethane at relatively low temperature from 475 °C to 525 °C (the first 3 points). The addition of potassium promotes the ethane conversion at higher temperature (from 550 °C to 600 °C). According to Figure B-1(b), catalysts with potassium addition at K/Si = 0.05% and 0.25% yield high selectivity than potassium free catalyst. From Figure B-1(c), catalysts with potassium addition at K/Si = 0.05% and 0.25% give high yields of aldehydes with stable catalytic activities with the increase of temperature.

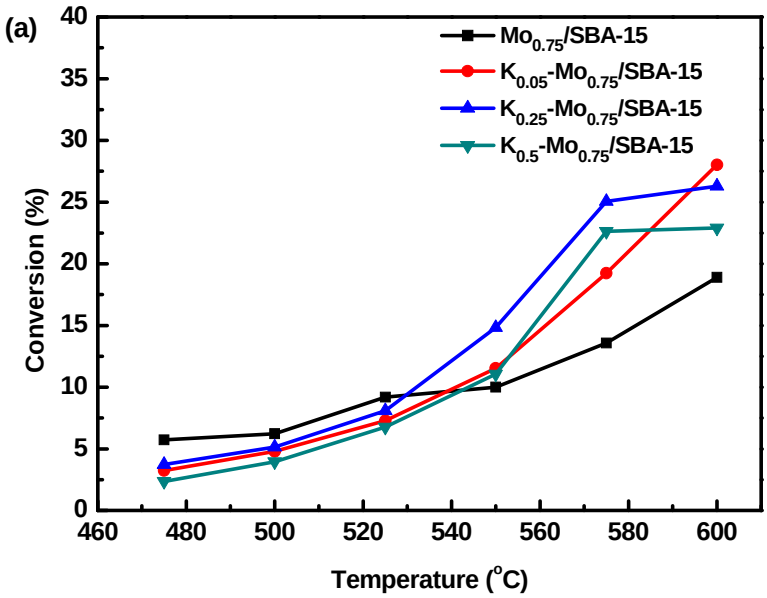
(a)
Conversion (%)
Temperature (°C)
Mo0.75/SBA-15
K0.05-Mo0.75/SBA-15
K0.25-Mo0.75/SBA-15
K0.5-Mo0.75/SBA-15

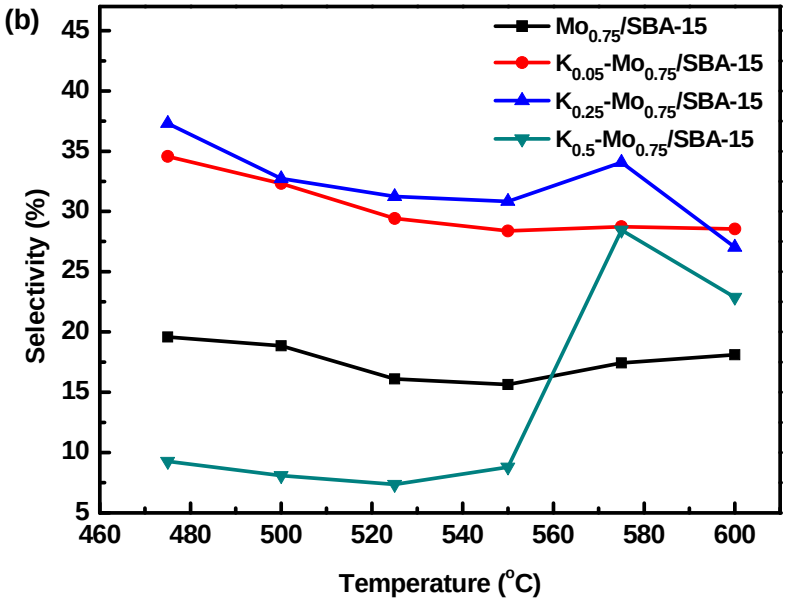
(b)
Selectivity (%)
Temperature (°C)
Mo0.75/SBA-15
K0.05-Mo0.75/SBA-15
K0.25-Mo0.75/SBA-15
K0.5-Mo0.75/SBA-15

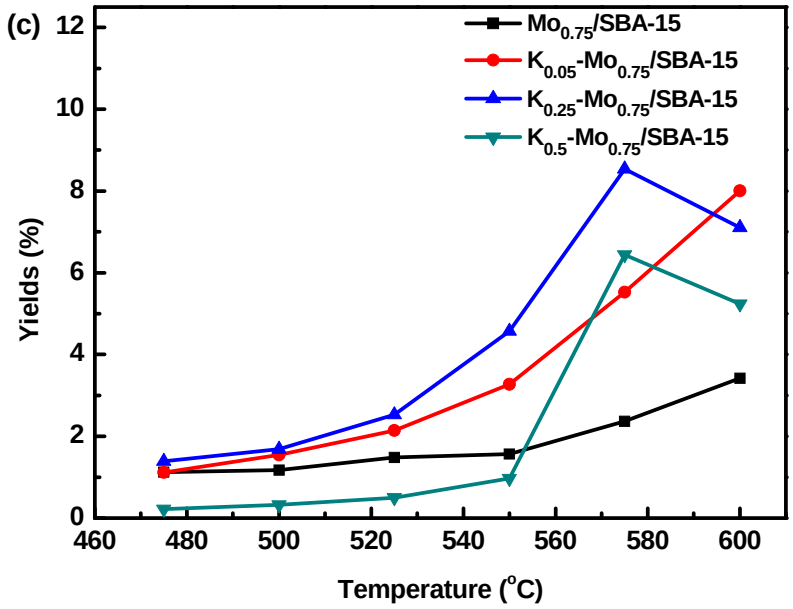

Figure B-1. (a) The conversion of C_2H_6 vs. temperature plot, (b) the selectivity to total aldehydes vs. temperature plot, and (c) and the total yields of total aldehydes vs. temperature plot over K_x-$Mo_{0.75}$/SBA-15 catalysts.

According to the above reaction data, the addition of suitable loading K markedly increased the rate of ethane oxidation, which is most probably related to the enhanced formation and reactivity of Mo^{6+}-O^- sites which play an important role in the oxidation. The increased activity of $K_{0.05}$-$Mo_{0.75}$/SBA-15 and $K_{0.25}$-$Mo_{0.75}$/SBA-15 catalysts may be due to the more dispersed Mo species and the formation of two-dimensional ploymolybdates. The higher selectivity of aldehydes over the latter should be ascribed to the formation of $K_2Mo_2O_7$ or K_2MoO_4 structures (tetrahedral and octahedral mixtures) [81].

Besides other characterization techniques, such as XRD, TEM, FT-IR, and UV-Raman, the Mo L_3-edge XANES spectra was used to identify the Mo oxidation states and to provide

complementary information about its coordination symmetry.

B.2 Experimental setup and results of Mo L_3-edge XANES

Mo L_3-edge (2,520 eV) X-ray absorption near edge structure (XANES) spectra were collected at Beamline 9-BM of Advanced Photon Source (APS), Argonne National Laboratory. The monochromator was double-crystal Si (111), and the XANES spectra were collected in fluorescence mode with a Si DRIFT 4-element detector (Vortex). Harmonics were rejected by use of a Rh-coated flat mirror in the experimental station. A small amount of well-ground sample was evenly spread over a tape. Energy calibration was accomplished by setting the edge energy of Mo L_3-edge to 2,520 eV. XANES data were processed using Athena [68, 85].

Catalysts $Mo_{0.75}$/SBA-15 and $K_{0.25}$-$Mo_{0.75}$/SBA-15, the two samples having the most contrast in term of catalytic activity (Figure 5-4(c)), are chosen for the study of potassium promotion effect. For Mo_{10}/SBA-15 sample, due to the excess amount of Mo loading, formation of molybdenum oxide can be clearly detected by XRD. Mo_{10}/SBA-15 catalyst has almost no yields for aldehydes, mainly due to the low dispersion of Mo species and lack of active sites. Detailed result is presented in published work in Liu et. al. [81]. The Mo_{10}/SBA-15 catalyst is purely used as a control sample for geometry determination purpose. The Mo L_3-edge XANES spectra are shown in Figure B-2.

XANES spectroscopy can measure coordination structure about a specific element. A method has been established to study Mo coordination structure with Mo L_3-edge XANES from d-orbital splitting [86]. In the XANES spectra, a d-orbital splitting was observed in the range of

1.8 to 2.4 eV for tetrahedral structures, and 3.1 to 4.5 eV for octahedral structures [87-89].

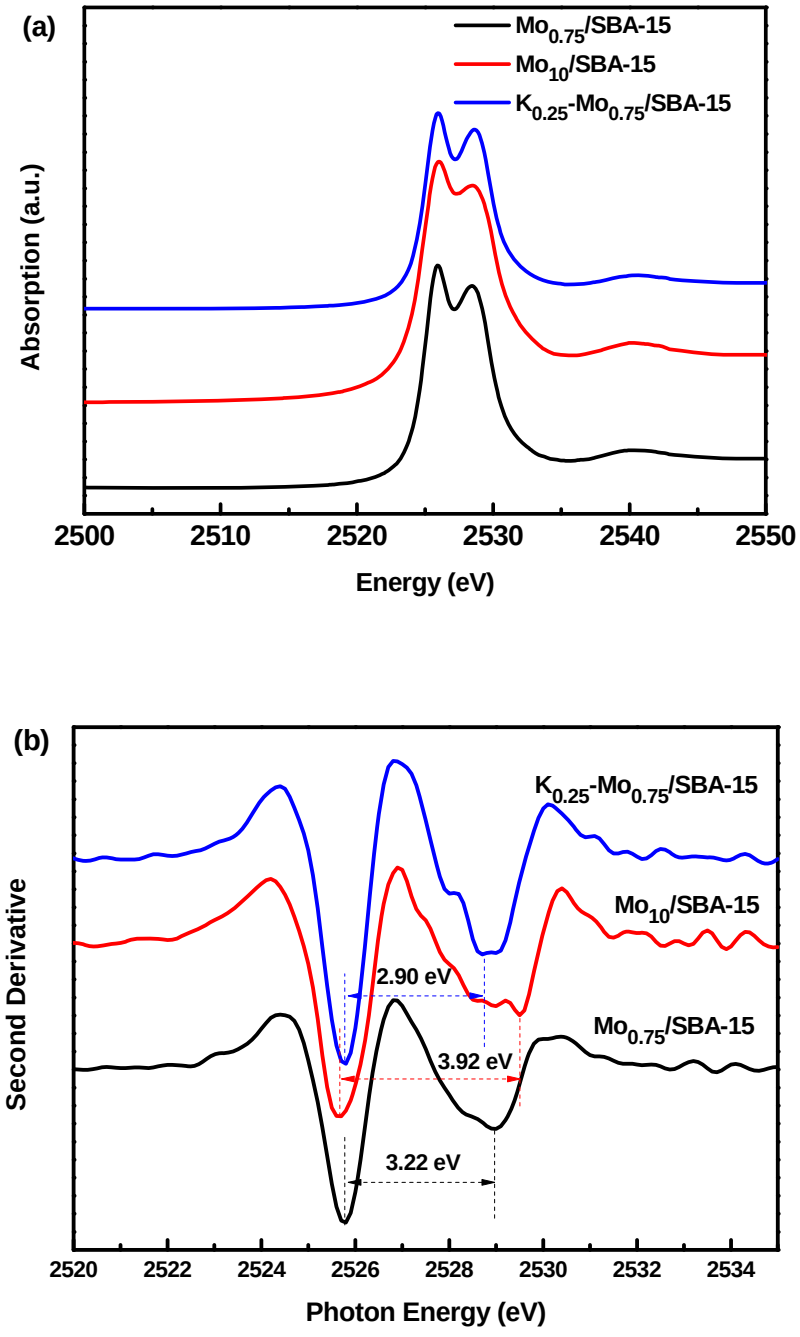

Figure B-2. (a) Mo L_3-edge XANES spectra and (b) second derivative of Mo L_3-edge XANES spectra for the DHT samples with and without the addition of potassium

In Figure B-2(a), similar shape of spectra were observed among these three samples. Figure B-2(b) shows the second derivative of Mo L_3-edge XANES spectra for the purpose of magnifying the differences within the spectra. The energy difference of the two dips (near 2,526 eV and 2,529 eV) shown in the second derivative of the XANES spectra read the d-orbital splitting values. It shows that $K_{0.25}$-$Mo_{0.75}$/SBA-15 sample has a smaller d-orbital splitting than $Mo_{0.75}$/SBA-15 sample and the Mo_{10}/SBA-15 catalyst has the biggest d-orbital splitting. More quantitative result is presented in Table B-1 listing the d-orbital splitting for different Mo samples and their molybdate species.

Table B-1. D-orbital splitting in Mo L_3-edge of XANES spectra and the coordination symmetry of molybdate species

Sample	Mo:Si (or K:Mo:Si)	d-orbital splitting (eV)	Structure
$Mo_{0.75}$/SBA-15	0.75:100	3.22	[a]Oct
Mo_{10}/SBA-15	10:100	3.92	[a]Oct
$K_{0.25}$-$Mo_{0.75}$/SBA-15	0.25: 0.75:100	2.90	[b]Tet+[a]Oct

a: Octahedral
b: Tetrahedral,

In the absence of potassium, the sample with high Mo loading (Mo_{10}/SBA-15, the d-orbital splitting is 3.92 eV) has an octahedral structure while the lower loading sample ($Mo_{0.75}$/SBA-15) has d-orbital splitting at 3.22 eV, which suggests a decrease of the octahedral Mo species in the mixture. The addition of potassium promotes the further isolation of Mo species and thus causes the structure change from octahedral to tetrahedral for the $K_{0.25}$-$Mo_{0.75}$/SBA-15 sample (the d-orbital splitting is 2.90 eV), and thus $K_{0.25}$-$Mo_{0.75}$/SBA-15 sample has more tetrahedral

structures. The XANES results are consistent with UV-Vis and Raman measurements. The results of UV-Vis and Raman results along with other characterization results can be obtained from reference [81].

B.3 Summary

The catalytic performances of a series of K-doped $Mo_{0.75}$/SBA-15 catalysts for the selective oxidation of the ethane to aldehydes were investigated. The results showed that the introduction of a moderate amount of K (0.25 and 0.5 mol%) into the $Mo_{0.75}$/SBA-15 catalyst greatly enhanced the catalytic activity and the selectivity to the total aldehydes in the selective oxidation of C_2H_6. It is believed that the formation of $K_2Mo_2O_7$ or K_2MoO_4, which are the mixture of tetrahedral and octahedral coordinated structures, serve as new active sites for the enhanced selective oxidation reactions. Mo L_3-edge XANES is a useful tool for identifying the coordination symmetry.

Appendix C. Infra red spectroscopy analysis of MPNC and MPNC-S materials

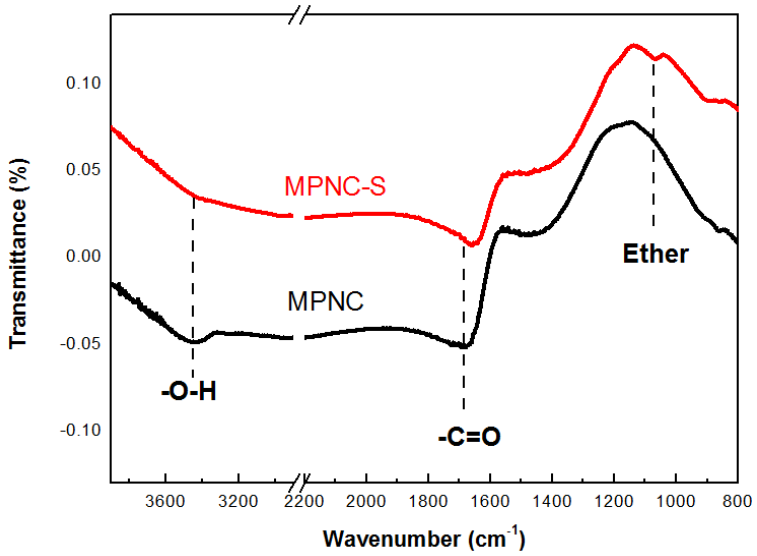

Figure C-1. IR spectra of MPNC materials before and after sulfur loading.

The transformation of oxygen functional groups was also observed by FTIR. Figure C-1 shows the IR spectra of MPNC materials before and after sulfur loading. The bands appeared near 1,680~1,670 cm^{-1} are attributed to vibration of C=O stretching and the board bands around 3,600~3,250 cm^{-1} are assigned to O–H stretching in carboxyl group [90]. More likely, the band shift to lower wavenumber at 1,680 cm^{-1} after sulfur absorption on MPNC material indicated a weaker C=O stretching, which is consistent with the hypothesis that cleavage of C=O bond resulted in the decrease of the abundance of carboxyl and carbonyl groups. Additionally, a weakened O–H stretching at 3,400 cm^{-1} implied a transformation of carboxyl group. Cyclic ether group or likely, C–O–S species can be yield as a consequence of cleavage of C=O bond, which can be assigned to the band appeared at 1080 cm^{-1} after sulfur absorption [91, 92].

REFERENCES

1. Brain, M. *How Lithium-ion Batteries Work*. 14 November 2006 [cited 2013 May 20]; Available from: http://electronics.howstuffworks.com/everyday-tech/lithium-ion-battery.htm.
2. Goodenough, J.B. and Y. Kim, *Challenges for Rechargeable Li Batteries†.* Chemistry of Materials, 2009. **22**(3): p. 587-603.
3. Xu, K., *Nonaqueous Liquid Electrolytes for Lithium-Based Rechargeable Batteries.* Chemical Reviews, 2004. **104**(10): p. 4303-4418.
4. Imhof, R. and P. Novák, *Oxidative Electrolyte Solvent Degradation in Lithium‐Ion Batteries: An In Situ Differential Electrochemical Mass Spectrometry Investigation.* Journal of The Electrochemical Society, 1999. **146**(5): p. 1702-1706.
5. Markevich, E., V. Baranchugov, and D. Aurbach, *On the possibility of using ionic liquids as electrolyte solutions for rechargeable Li ion batteries.* Electrochemistry Communications, 2006. **8**(8): p. 1331-1334.
6. Garcia, B., et al., *Room temperature molten salts as lithium battery electrolyte.* Electrochimica Acta, 2004. **49**(26): p. 4583-4588.
7. Stassen, I. and G. Hambitzer, *Metallic lithium batteries for high power applications.* Journal of Power Sources, 2002. **105**(2): p. 145-150.
8. Nishimoto, A., et al., *High ionic conductivity of new polymer electrolytes based on high molecular weight polyether comb polymers.* Electrochimica Acta, 1998. **43**(10–11): p. 1177-1184.
9. Croce, F., et al., *Nanocomposite polymer electrolytes for lithium batteries.* Nature, 1998. **394**(6692): p. 456-458.
10. Croce, F., et al., *Physical and Chemical Properties of Nanocomposite Polymer Electrolytes.* The Journal of Physical Chemistry B, 1999. **103**(48): p. 10632-10638.
11. Croce, F., L. Settimi, and B. Scrosati, *Superacid ZrO2-added, composite polymer electrolytes with improved transport properties.* Electrochemistry Communications, 2006. **8**(2): p. 364-368.
12. Hayashi, A., *Preparation and Characterization of Glassy Materials for All-Solid-State Lithium Secondary Batteries (Review).* Journal of the Ceramic Society of Japan, 2007. **115**(1338): p. 110-117.
13. Alonso, J.A., et al., *On the Location of Li+ Cations in the Fast Li-Cation Conductor La0.5Li0.5TiO3 Perovskite.* Angewandte Chemie International Edition, 2000. **39**(3): p. 619-621.
14. Knauth, P., *Inorganic solid Li ion conductors: An overview.* Solid State Ionics, 2009. **180**(14–16): p. 911-916.
15. Yashima, M., et al., *Crystal Structure and Diffusion Path in the Fast Lithium-Ion Conductor La0.62Li0.16TiO3.* Journal of the American Chemical Society, 2005. **127**(10): p. 3491-3495.

16. Robertson, A.D., A.R. West, and A.G. Ritchie, *Review of crystalline lithium-ion conductors suitable for high temperature battery applications.* Solid State Ionics, 1997. **104**(1–2): p. 1-11.
17. Kamaya, N., et al., *A lithium superionic conductor.* Nature Materials, 2011. **10**(9): p. 682-686.
18. Reddy, M.V., G.V. Subba Rao, and B.V.R. Chowdari, *Metal Oxides and Oxysalts as Anode Materials for Li Ion Batteries.* Chemical Reviews, 2013.
19. Hatchard, T.D. and J.R. Dahn, *In Situ XRD and Electrochemical Study of the Reaction of Lithium with Amorphous Silicon.* Journal of The Electrochemical Society, 2004. **151**(6): p. A838-A842.
20. Kim, I.-S. and P.N. Kumta, *High capacity Si/C nanocomposite anodes for Li-ion batteries.* Journal of Power Sources, 2004. **136**(1): p. 145-149.
21. Takamura, T., et al., *High capacity and long cycle life silicon anode for Li-ion battery.* Journal of Power Sources, 2006. **158**(2): p. 1401-1404.
22. Ma, H., et al., *Nest-like Silicon Nanospheres for High-Capacity Lithium Storage.* Advanced Materials, 2007. **19**(22): p. 4067-4070.
23. Obrovac, M.N., et al., *Alloy Design for Lithium-Ion Battery Anodes.* Journal of The Electrochemical Society, 2007. **154**(9): p. A849-A855.
24. Park, C.-M., et al., *Li-alloy based anode materials for Li secondary batteries.* Chemical Society Reviews, 2010. **39**(8): p. 3115-3141.
25. Huggins, R.A., *Lithium alloy negative electrodes.* Journal of Power Sources, 1999. **81–82**: p. 13-19.
26. Todd, A.D.W., et al., *Tin-based materials as negative electrodes for Li-ion batteries: Combinatorial approaches and mechanical methods.* International Journal of Energy Research, 2010. **34**(6): p. 535-555.
27. Whittingham, M.S., *Lithium Batteries and Cathode Materials.* Chemical Reviews, 2004. **104**(10): p. 4271-4302.
28. Girishkumar, G., et al., *Lithium−Air Battery: Promise and Challenges.* The Journal of Physical Chemistry Letters, 2010. **1**(14): p. 2193-2203.
29. McCloskey, B.D., et al., *Solvents' Critical Role in Nonaqueous Lithium–Oxygen Battery Electrochemistry.* The Journal of Physical Chemistry Letters, 2011. **2**(10): p. 1161-1166.
30. Freunberger, S.A., et al., *Reactions in the Rechargeable Lithium–O2 Battery with Alkyl Carbonate Electrolytes.* Journal of the American Chemical Society, 2011. **133**(20): p. 8040-8047.
31. Xu, W., et al., *Investigation on the charging process of Li2O2-based air electrodes in Li–O2 batteries with organic carbonate electrolytes.* Journal of Power Sources, 2011. **196**(8): p. 3894-3899.
32. Christensen, J., et al., *A Critical Review of Li/Air Batteries.* Journal of The Electrochemical Society, 2012. **159**(2): p. R1-R30.
33. Bruce, P.G., B. Scrosati, and J.-M. Tarascon, *Nanomaterials for Rechargeable Lithium Batteries.* Angewandte Chemie International Edition, 2008. **47**(16): p. 2930-2946.

34. Evers, S. and L.F. Nazar, *New Approaches for High Energy Density Lithium-Sulfur Battery Cathodes.* Accounts of Chemical Research, 2012: p. 1135-1143.
35. Manthiram, A., Y. Fu, and Y.S. Su, *Challenges and Prospects of Lithium-Sulfur Batteries.* Accounts of Chemical Research, 2012: p. 1125-1134.
36. Kolosnitsyn, V.S. and E.V. Karaseva, *Lithium-sulfur batteries: Problems and solutions.* Russian Journal of Electrochemistry, 2008. **44**(5): p. 506-509.
37. Mikhaylik, Y.V. and J.R. Akridge, *Polysulfide Shuttle Study in the Li/S Battery System.* Journal of The Electrochemical Society, 2004. **151**(11): p. A1969-A1976.
38. Ji, X., et al., *Stabilizing lithium-sulphur cathodes using polysulphide reservoirs.* Nature Communications, 2011. **2**: p. 325.
39. Liang, C., N.J. Dudney, and J.Y. Howe, *Hierarchically Structured Sulfur/Carbon Nanocomposite Material for High-Energy Lithium Battery.* Chemistry of Materials, 2009. **21**(19): p. 4724-4730.
40. Ji, X., K.T. Lee, and L.F. Nazar, *A highly ordered nanostructured carbon-sulphur cathode for lithium-sulphur batteries.* Nat Mater, 2009. **8**(6): p. 500-506.
41. Aurbach, D., et al., *On the Surface Chemical Aspects of Very High Energy Density, Rechargeable Li–Sulfur Batteries.* Journal of The Electrochemical Society, 2009. **156**(8): p. A694-A702.
42. Hassoun, J. and B. Scrosati, *Moving to a Solid-State Configuration: A Valid Approach to Making Lithium-Sulfur Batteries Viable for Practical Applications.* Advanced Materials, 2010. **22**(45): p. 5198-5201.
43. Su, Y.-S. and A. Manthiram, *A new approach to improve cycle performance of rechargeable lithium-sulfur batteries by inserting a free-standing MWCNT interlayer.* Chemical Communications, 2012. **48**(70): p. 8817-8819.
44. Su, Y.-S. and A. Manthiram, *Lithium–sulphur batteries with a microporous carbon paper as a bifunctional interlayer.* Nature Communications, 2012. **3**: p. 1166.
45. MIT, E.V.T. *A Guide to Understanding Battery Specifications*. December 2008 [cited 2013 June 3]; Available from: http://web.mit.edu/evt/summary_battery_specifications.pdf.
46. Newville, M., *Fundamentals of XAFS*, July 23, 2004: University of Chicago, Chicago, IL. p. 40.
47. Giorgetti, M., *A Review on the Structural Studies of Batteries and Host Materials by X-Ray Absorption Spectroscopy.* ISRN Materials Science, 2013. **2013**: p. 22.
48. Gocke, E., et al., *Molybdenum cluster chalcogenides Mo6X8: Electrochemical intercalation of closed shell ions Zn2+, Cd2+, and Na.* Journal of Solid State Chemistry, 1987. **70**(1): p. 71-81.
49. Tarascon, J.M., T.P. Orlando, and M.J. Neal, *Rechargeable Lithium Batteries Based on the Ternary Chevrel Phase AgMo6 S 8 as the Cathode.* Journal of The Electrochemical Society, 1988. **135**(4): p. 804-808.
50. [cited 2013 June 18th]; Available from: http://www.answers.com/topic/chevrel-phase.
51. Stiles, J.A.R., *A new rechargeable lithium battery.* Journal of Power Sources, 1989. **26**(1–2): p. 233-242.

52. McKinnon, W.R. and J.R. Dahn, *Structure and electrochemistry of $Li_xMo_6S_8$.* Physical Review B, 1985. **31**(5): p. 3084-3087.
53. Gocke, E., et al., *Molybdenum cluster chalcogenides Mo6X8: intercalation of lithium via electron/ion transfer.* Inorganic Chemistry, 1987. **26**(11): p. 1805-1812.
54. Levi, M.D., et al., *A comparative study of Mg2+ and Li+ ion insertions into the Mo6S8 Chevrel phase using electrochemical impedance spectroscopy.* Journal of Electroanalytical Chemistry, 2004. **569**(2): p. 211-223.
55. Li, X., et al., *Optimization of mesoporous carbon structures for lithium-sulfur battery applications.* Journal of Materials Chemistry, 2011. **21**(41): p. 16603-16610.
56. Li, N., et al., *High-rate lithium-sulfur batteries promoted by reduced graphene oxide coating.* Chemical Communications, 2012. **48**(34): p. 4106-4108.
57. Ji, L., et al., *Graphene Oxide as a Sulfur Immobilizer in High Performance Lithium/Sulfur Cells.* Journal of the American Chemical Society, 2011. **133**(46): p. 18522-18525.
58. Gong, K., et al., *Nitrogen-Doped Carbon Nanotube Arrays with High Electrocatalytic Activity for Oxygen Reduction.* Science, 2009. **323**(5915): p. 760-764.
59. Zhang, L. and Z. Xia, *Mechanisms of Oxygen Reduction Reaction on Nitrogen-Doped Graphene for Fuel Cells.* The Journal of Physical Chemistry C, 2011. **115**(22): p. 11170-11176.
60. Shin, W.H., et al., *Nitrogen-Doped Multiwall Carbon Nanotubes for Lithium Storage with Extremely High Capacity.* Nano Letters, 2012. **12**(5): p. 2283-2288.
61. Guo, J., et al., *Lithium–Sulfur Battery Cathode Enabled by Lithium–Nitrile Interaction.* Journal of the American Chemical Society, 2012. **135**(2): p. 763-767.
62. Maldonado, S. and K.J. Stevenson, *Influence of Nitrogen Doping on Oxygen Reduction Electrocatalysis at Carbon Nanofiber Electrodes.* The Journal of Physical Chemistry B, 2005. **109**(10): p. 4707-4716.
63. Wang, H., T. Maiyalagan, and X. Wang, *Review on Recent Progress in Nitrogen-Doped Graphene: Synthesis, Characterization, and Its Potential Applications.* ACS Catalysis, 2012. **2**(5): p. 781-794.
64. Qie, L., et al., *Nitrogen-doped porous carbon nanofiber webs as anodes for lithium ion batteries with a superhigh capacity and rate capability.* Advanced Materials, 2012. **24**(15): p. 2047-50.
65. Yang, S., et al., *Graphene-based carbon nitride nanosheets as efficient metal-free electrocatalysts for oxygen reduction reactions.* Angewandte Chemie. International Edition in English, 2011. **50**(23): p. 5339-43.
66. Gong, K., et al., *Nitrogen-doped carbon nanotube arrays with high electrocatalytic activity for oxygen reduction.* Science, 2009. **323**(5915): p. 760-4.
67. Niwa, H., et al., *X-ray absorption analysis of nitrogen contribution to oxygen reduction reaction in carbon alloy cathode catalysts for polymer electrolyte fuel cells.* Journal of Power Sources, 2009. **187**(1): p. 93-97.

68. Ravel, B. and M. Newville, *ATHENA, ARTEMIS, HEPHAESTUS: data analysis for X-ray absorption spectroscopy using IFEFFIT.* Journal of Synchrotron Radiation, 2005. **12**(4): p. 537-541.
69. Kim, K., et al., *Characterization of oxygen containing functional groups on carbon materials with oxygen K-edge X-ray absorption near edge structure spectroscopy.* Carbon, 2011. **49**(5): p. 1745-1751.
70. McKeown, D.A., et al., *Determination of sulfur environments in borosilicate waste glasses using X-ray absorption near-edge spectroscopy.* Journal of Non-Crystalline Solids, 2004. **333**(1): p. 74-84.
71. Gao, H., et al., *A simple method to synthesize continuous large area nitrogen-doped graphene.* Carbon, 2012. **50**(12): p. 4476-4482.
72. Kundu, S., et al., *Electrocatalytic Activity and Stability of Nitrogen-Containing Carbon Nanotubes in the Oxygen Reduction Reaction.* The Journal of Physical Chemistry C, 2009. **113**(32): p. 14302-14310.
73. Shao, Y., et al., *Nitrogen-doped graphene and its electrochemical applications.* Journal of Materials Chemistry, 2010. **20**(35): p. 7491-7496.
74. Jalilehvand, F., *Sulfur: not a "silent" element any more.* Chemical Society Reviews, 2006. **35**(12): p. 1256-1268.
75. Wanjala, B.N., et al., *Correlation between Atomic Coordination Structure and Enhanced Electrocatalytic Activity for Trimetallic Alloy Catalysts.* Journal of the American Chemical Society, 2011. **133**(32): p. 12714-12727.
76. Wanjala, B.N., et al., *Design of Ternary Nanoalloy Catalysts: Effect of Nanoscale Alloying and Structural Perfection on Electrocatalytic Enhancement.* Chemistry of Materials, 2012. **24**(22): p. 4283-4293.
77. Zhan, D., J. Velmurugan, and M.V. Mirkin, *Adsorption/Desorption of Hydrogen on Pt Nanoelectrodes: Evidence of Surface Diffusion and Spillover.* Journal of the American Chemical Society, 2009. **131**(41): p. 14756-14760.
78. Rehr, J.J. and R.C. Albers, *Theoretical approaches to x-ray absorption fine structure.* Reviews of Modern Physics, 2000. **72**(3): p. 621-654.
79. Rehr, J.J. and R.C. Albers, *Theoretical approaches to x-ray absorption fine structure.* Reviews of Modern Physics, 2000. **72**(3): p. 621.
80. Chen, Y., J.L. Fulton, and W. Partenheimer, *The Structure of the Homogeneous Oxidation Catalyst, Mn(II)(Br-1)x, in Supercritical Water: An X-ray Absorption Fine-Structure Study.* Journal of the American Chemical Society, 2005. **127**(40): p. 14085-14093.
81. Liu, J., et al., *Potassium-modified molybdenum-containing SBA-15 catalysts for highly efficient production of acetaldehyde and ethylene by the selective oxidation of ethane.* Journal of Catalysis, 2012. **285**(1): p. 134-144.
82. Lou, Y., et al., *SBA-15-supported molybdenum oxides as efficient catalysts for selective oxidation of ethane to formaldehyde and acetaldehyde by oxygen.* Journal of Catalysis, 2007. **247**(2): p. 245-255.

83. Zhang, Q., et al., *Vanadium-Containing MCM-41 for Partial Oxidation of Lower Alkanes.* Journal of Catalysis, 2001. **202**(2): p. 308-318.
84. Zhao, Z., et al., *Selective Oxidation of Ethane to Acetaldehyde and Acrolein over Silica-Supported Vanadium Catalysts Using Oxygen as Oxidant.* Journal of Catalysis, 2000. **190**(2): p. 215-227.
85. Bravo-Suárez, J.J., et al., *Mechanistic study of propane selective oxidation with H2 and O2 on Au/TS-1.* Journal of Catalysis, 2008. **257**(1): p. 32-42.
86. Hu, H., I.E. Wachs, and S.R. Bare, *Surface Structures of Supported Molybdenum Oxide Catalysts: Characterization by Raman and Mo L_3-edge XANES.* The Journal of Physical Chemistry, 1995. **99**(27): p. 10897-10910.
87. George, S.J., et al., *Molybdenum X-ray absorption edges from 200 to 20,000 eV: The benefits of soft X-ray spectroscopy for chemical speciation.* Journal of Inorganic Biochemistry, 2009. **103**(2): p. 157-167.
88. Aritani, H., et al., *Methane dehydroaromatization over Mo-modified H-MFI for gas to liquid catalysts.* Journal of Environmental Sciences, 2009. **21**(6): p. 736-740.
89. Lede, E.J., et al., *XANES Mo L-edges and XPS Study of Mo Loaded in HY Zeolite.* The Journal of Physical Chemistry B, 2002. **106**(32): p. 7824-7831.
90. Fanning, P.E. and M.A. Vannice, *A DRIFTS study of the formation of surface groups on carbon by oxidation.* Carbon, 1993. **31**(5): p. 721-730.
91. Meldrum, B.J. and C.H. Rochester, *In situ infrared study of the surface oxidation of activated carbon dispersed in potassium bromide.* Journal of the Chemical Society, Faraday Transactions, 1990. **86**(17): p. 2997-3002.
92. Shafeeyan, M.S., et al., *A review on surface modification of activated carbon for carbon dioxide adsorption.* Journal of Analytical and Applied Pyrolysis, 2010. **89**(2): p. 143-151.

VITA

Pengyu Zhu

EDUCATION

Ph. D. in Energy and Mineral Engineering August 2013
The Pennsylvania State University, University Park, PA, USA

M. S. in Chemical Engineering June 2009
University of Idaho, Idaho Falls, ID

B. S. in Chemical Engineering June 2007
Sichuan University, Chengdu, China

PUBLICATIONS

- ***Zhu, P.***; Song, J.; Lv, D.; Wang, D.; Jaye, C.; Fischer, D.; Wu, T.; Chen, Y., *X-ray Absorption Analysis of Nitrogen Contribution to the Enhanced Performance of Lithium-sulfur Battery on Mesoporous Carbon Cathode.* In Preparation.
- Song, J.; Xu, T.; Gordin, L.M.; Lv, D.; ***Zhu, P.***; Jiang, Y-B.; Chen, Y.; Wang D., *Nitrogen-Doped Mesoporous Carbon-Sulfur Nanocomposite Cathodes for Lithium-Sulfur Batteries: Enhanced Performance by Exploiting Chemical Adsorption.* Submitted to **Advanced Energy Materials**.
- Wanjala, B. N.; Fang, B.; Shan, S.; Petkov, V.; ***Zhu, P.***; Loukrakpam, R.; Chen, Y.; Luo, J.; Yin, J.; Yang, L.; Shao, M.; Zhong, C.-J., *Design of Ternary Nanoalloy Catalysts: Effect of Nanoscale Alloying and Structural Perfection on Electrocatalytic Enhancement*. **Chemistry of Materials** 2012**,** *24* (22), 4283-4293.
- Liu, J.; Yu, L.; Zhao, Z.; Chen, Y.; ***Zhu, P***.; Wang, C.; Luo, Y.; Xu, C.; Duan, A.; Jiang, G., *Potassium-modified molybdenum-containing SBA-15 catalysts for highly efficient production of acetaldehyde and ethylene by the selective oxidation of ethane.* **Journal of Catalysis,** 2012**,** 285 (1), 134-144.
- Kim, K.; ***Zhu, P.***; Li, N.; Ma, X.; Chen, Y., *Characterization of oxygen containing functional groups on carbon materials with oxygen K-edge X-ray absorption near edge structure spectroscopy.* **Carbon**, 2011. 49(5): p. 1745-1751.

AWARDS

Graduate Nuclear Engineering Award Scholarship, University of Idaho 2007—2008